Controllable Association of Ion-Containing Polymers in Dilute Solution

Shufu Peng

Department of Chemistry, The Chinese University of Hong Kong, Shatin, Hong Kong

Chi Wu

*Department of Chemistry, The Chinese University of Hong Kong, Shatin, Hong Kong and
The Open Laboratory of Bond-Selective Chemistry, Department of Chemical Physics,
University of Science and Technology of China, Hefei, Anhui, China*

CONTENTS

1. INTRODUCTION

1.1. Overview of Polyelectrolyte Studies

Polyelectrolytes, which are defined as macromolecules with ~10 mol% or more ionic groups on their chain backbones, are soluble in highly polar solvents, ubiquitous in biological systems, and useful in environmentally friendly polymer processes. Polyelectrolytes remain one of the least-understood states of condensed matter, in contrast to neutral polymer solutions. Although considerable efforts have been made to understand the properties of polyelectrolytes over the past several decades, an understanding of the behavior of polyelectrolytes is lacking. This problem is especially critical because of the fundamental importance of many of the prototypical polyelectrolytes. In the dilute regime, properties of polyelectrolytes include the dimensions, interactions, correlations, diffusion, and viscosity of polyelectrolytes in response to their ionic environments: charges, mass densities, and distributions have been studied [1–3]. Such study is difficult because the solution contains at least four components: polyions, counterions, coions, and solvent, and also because different interactions, such as intra- and interchain interactions, long-range electrostatic interactions, hydrophobic interactions, and entropic force, have to be simultaneously considered [4]. Different interactions of polyelectrolytes with other charged and uncharged polymers can lead to the formation of complexes, gel formation, precipitation, phase separation, and other phenomena.

In addition to industrial interests, theoretical and experimental studies have shown that polyelectrolyte solutions differ fundamentally from neutral polymers with respect to, for example, their scattering properties and viscosity behavior. A growing interest in weakly charged polyelectrolyte systems is observed in both theoretical and experimental studies. Theoretical works based on the concept of electrostatic persistence length were presented by Odijk [5], Skolnick and Fixman [6], and Barrat and Joanny [7]. Various experimental techniques used to understand the behavior of polyelectrolyte systems include small X-ray scattering (SAXS), small angle neutron scattering (SANS), viscosity measurements, and static and dynamic light scattering (LLS) [8–11]. Models to describe the properties such as scattering properties, phase diagrams, and the viscosity behavior of weakly charged polyelectrolytes in solutions and in gels have been developed by de Gennes et al. [12], Khokhlov and Khachaturian [13], Borue and Eurokomovich [14], Joanny and Leibler [15], and Vilgis and Borsali [16]. Experimentally, Essafi et al. [17], Shibayama et al. [18], and Moussaid et al. [19] carried out studies on weakly charged systems.

1.2. Polyelectrolyte Complex Formation

1.2.1. Chain Conformations and Complex Formation

In contrast to the simple procedure of polyelectrolyte complex formation, a deeper understanding of the processes that govern the formation of supermolecular structures is still a challenge to scientists due to the great variety of different polyelectrolytes, the various influences of a lot of external parameters, and the interfering interactions of non-Coulomb forces. Starting with the pioneering work of Michaels and Miekka [20], who prepared well-defined polysalts with a 1:1 stoichiometry, a continuously increasing number of publications have appeared, many of which are reviewed in [21] and [22]. Successful contributions to elucidate the mechanism of polyelectrolyte complex formation have been made by Tsuchida et al. [23], and Kabanov and Zezin [24] on the subject of sequential water-soluble polyelectrolyte complexes in dilute solutions of polyelectrolyte components with significantly different molecular weights in nonstoichiometric systems. In dilute solutions, polyelectrolyte complex formation leads to aggregates with dimensions on a colloidal level, building optically homogeneous and stable dispersions. This offers the possibility to study the formation of polyelectrolyte complexes as well as the structures of polyelectrolyte complex particles by methods normally used for the characterization of polymer solutions.

1.2.2. Complexation with Cations

The study of cation and polyanion association and interaction is important to the understanding of various physicochemical behaviors in environmental research and biological science. Such an association also has many direct technological applications. Experimental observation is usually related to an overall distribution of cations around polyanion chains without knowing how various fractions are attributed to different underlying interaction processes, such as electrostatics and complexation [25]. Polyelectrolyte complexes can be formed as a result of interaction when some cations are added to dilute solutions [26]. Coulomb attraction or other interactions, such as hydrogen bonding, dipole–dipole interaction, charge-transfer interaction, and hydrophobic effects may drive the association. These forces are important factors in determining the overall configuration and stability of the complexes. Efforts to study polyelectrolyte complexation with cations have focused on synthetic homopolymers [27–29] and copolymers [30]. The influences of ionic strength, composition of solvent, and nature of various metal ions on the properties of polyelectrolyte–metal complexes have been discussed [31].

1.2.3. Polyelectrolyte–Protein Complexes

Polyelectrolyte complexes with protein molecules [32] and micelle polyelectrolyte complexes [33, 34] were investigated in detail by focusing on the complex structure as well as the effect of ionic strength. The structural parameters of the complexes were determined using light-scattering measurements. A mechanism for the complexation that was suggested explained stoichiometeric complex formation at low ionic strength and nonstoichiometric complex formation at high ionic strength. In light-scattering studies of polyelectrolyte complexes by Hara and Nakajima [29], the pronounced influences of the ionic strength of the solution and the mixing

ratio of polyelectrolyte components on the complex formation were discussed. Studies on the interactions between polyelectrolytes and globular proteins bearing a net opposite charge have been reported [35]. However, the mechanism of interaction between polyion and ampholytic protein with a net charge of the same sign as that of the polyion is less understood.

1.2.4. Mechanism of Complex Formation

Despite a great deal of effort, the mechanism of complex formation among polyelectrolytes and cations or protein is still lacking due to the high complexity of the phenomena. The responses of the complex particles to the variation of experimental conditions are quite different owing to the peculiarities of the system investigated. A combination of different scattering techniques provides a possibility to study the formation and structures of colloidal complexes over a wide size range [36–38]. The formation of interpolymer and intrapolymer complexes has been studied [39, 40]. The transition from intrachain complexation to interchain aggregation of polyelectrolytes has received little attention.

1.3. Aggregation Process of Polyelectrolytes

Aggregating polyelectrolyte systems have many applications, such as water purification, papermaking, protein purification and other separation processes. Time-dependent aggregation of polyelectrolytes is encountered in many contexts. Polyelectrolytes of two opposite charges are mixed, resulting in the formation of a large and time-evolving aggregate [41]. The association kinetics of synthetic polyelectrolytes has been extensively studied [42–44]. It was found that the rate constant of the interaction increased sharply with decreasing polycation ionic strength, but was independent of the polyanion chain length [45, 46]. It was suggested that the distribution of ionic groups on the chain backbone had no effect on the complexation [47]. The kinetics of diffusion controlled aggregation were approached mathematically long ago by Smoluchowski [48], whose simplified analysis still provides a useful starting point for experimental analysis. More recent approaches using scaling and fractal theories have predicted kinetic and aggregate distributions [49, 50]. Unfortunately, most of the past studies were conducted in a poorly controlled and irreversible fashion. It seems that although the time evolution of polyelectrolyte complexes is often mentioned in the literature, quantitative approaches to its characterization are seldom taken. For example, how does the association and/or interaction influence the aggregation kinetics and the aggregate structures? How does the fractal dimension change with experimental conditions, such as temperature, salt concentration, time, and conformation of polyelectrolytes?

1.4. Main Goals

In this review, we summarize our recent efforts associate polyelectrolytes in the dilute regime. We believe that a careful characterization of structure, composition, and stability of these polyelectrolytes complexes is essential for a better understanding of the formation and structure of resultant complexes. We have systematically investigated and compared the temperature-, cation-, pH-, surfactant-, and protein-induced association of linear polyelectrolyte chains and spherical polyelectrolyte microgels. Our results reveal (1) the transition from intrachain complexation to interchain aggregation, (2) the controllable and reversible mechanisms for complexation as a function of temperature, pH, ionic strength, and charge density of the polyelectrolytes, and (3) the kinetics and structures of the complexes of linear chains and spherical microgels.

2. TEMPERATURE-INDUCED SWELLING AND SHRINKAGE OF POLYELECTROLYTES

2.1. Coil-to-Globule Transition of Linear Poly(N-Isopropylacrylamide) Ionomers

Poly(N-isopropylacrylamide) (PNIPAM) is a well-known thermal sensitive polymer [51, 52]. It is soluble in water at room temperature, but undergoes a phase separation at temperatures higher than its lower critical solution temperature (LCST; ~32 °C). This unusual and convenient phase transition temperature and its related solution properties have attracted much theoretical and technological interest [53–56]. It is commonly believed that this convenient LCST is the result of a delicate balance between the hydrophobic and hydrophilic interactions. At higher temperatures, the term related to the negative entropy change leads to a positive free energy change (i.e., $\Delta G = \Delta H - T \Delta S > 0$) so that individual PNIPAM chains collapse and aggregate in water [52].

A combination of static and dynamic laser light-scattering study of the collapsing process of two PNIPAM ionomers in deionized water showed that the collapse of PNIPAM ionomer chains as temperature increases generally involves two independent and competing processes: intrachain coil-to-globule transition and interchain aggregation. The higher the polymer concentration is, the larger the aggregates formed will be. The decrease of the ionomer concentration and the increase of the ionic content can suppress the interchain aggregation. Using an extremely dilute ionomer solution, we found another way to prepare a single polymer chain globule that is thermodynamically stable in water, where the requirement of a very narrowly distributed sample for the study of the coil-to-globule transition has been removed. Our results also indicate that some of the intersegment structures formed at higher temperature in the coil-to-globule transition can be preserved in the cooling process as long as the solution temperature is not too low. It should be of importance to further study these intersegment structures formed at high temperatures possibly by nuclear magnetic resonance (NMR).

Figure 1 shows that in the temperature range of 25–32 °C, the $R_{vv}(\theta)/KC$ of each solution is a constant in the small range of ~4–5 $\times 10^6$ g/mol, very close to the molar mass of individual PNIPAM-0.8KAA chains, indicating that there was no interchain aggregation. When the temperature is raised to
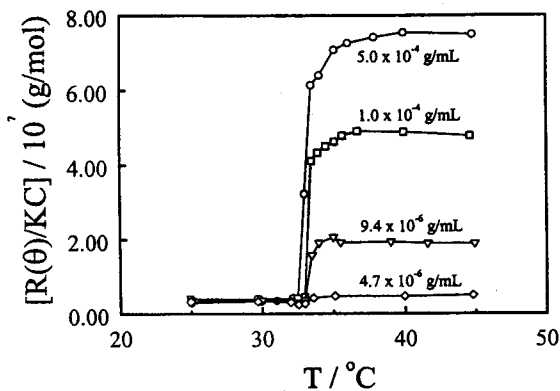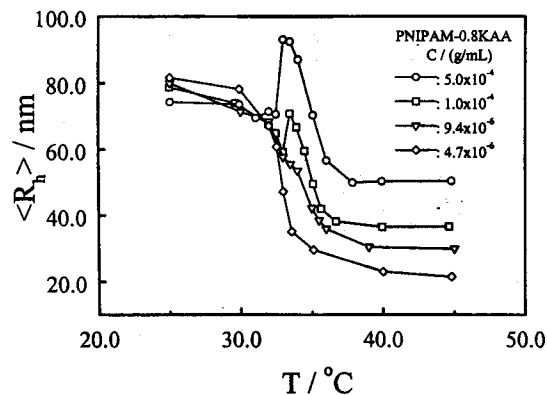
Figure 1. Temperature and concentration dependence of the excess scattering intensity $R_{vv}(\theta)/KC$ of PNIPAM-0.8KAA in deionized water, where K is a constant and $R_{vv}(\theta)/KC$ approximately equals the weight average molar mass (M_w) because the solution is very dilute. Reprinted with permission from [116], X. Qiu et al., *J. Polym. Sci., Part B: Polym. Phys.* 36, 1501 (1998). © 1998, John Wiley & Sons, Inc.

Figure 2. Temperature and concentration dependence of the average hydrodynamic radius $\langle R_h \rangle$ of PNIPAM-0.8KAA in deionized water. Reprinted with permission from [116], X. Qiu et al., *J. Polym. Sci., Part B: Polym. Phys.* 36, 1501 (1998). © 1998, John Wiley & Sons, Inc.

~32.5–33 °C, slightly higher than the LCST of PNIPAM, an abrupt increase of $R_{vv}(\theta)/KC$ appears for the solution with a concentration higher than 9.5×10^{-6} g/mL, clearly indicating interchain aggregation. Further increase of the temperature to ~34–35 °C, lead to a new $R_{vv}(\theta)/KC$ plateau. The constant $R_{vv}(\theta)/KC$ at temperatures higher than ~35 °C indicates the cessation of interchain aggregation. From the ratio of $[R_{vv}(\theta)/KC]_{T=45 \,°C}/[R_{vv}(\theta)/KC]_{T=25 \,°C}$, we were able to estimate the average number of PNIPAM chains inside each aggregate (N_{chain}) to be ~17, ~8, and ~4, respectively, for $C = 5.0 \times 10^{-4}$, 1.0×10^{-4}, and 9.5×10^{-6} g/mL. In the case of $C = 4.7 \times 10^{-6}$ g/mL, $R_{vv}(q)/KC$ is nearly independent of temperature. Note that $R_{vv}(q)$ is proportional to the square of the mass, that is, a dimer scatters four times more light than a unimer. Therefore, a very small amount of interchain aggregation leads to a large increase of $R_{vv}(\theta)/KC$. The temperature independence of $R_{vv}(q)/KC$ indicates no interchain aggregation in the extremely dilute solution even at temperatures as high as 45 °C.

Figure 2 shows that when $C = 4.7 \times 10^{-6}$ g/mL, $\langle R_h \rangle$ decreases as the temperature increases, which actually reflects the intrachain coil-to-globule transition, because we know from Figure 1 that in this solution there is no interchain aggregation in the heating process. This mechanism is very similar to the collapsing process observed for a neutral PNIPAM homopolymer chain in an extremely dilute solution [55]. The difference is that the sample used here ($M_w/M_n = 1.6$–1.7) is not as narrow as the one ($M_w/M_n < 1.1$) used in [55], which makes the experiment much easier. The decrease of $\langle R_h \rangle$ can be divided into three stages:

1. In the low temperature range (25–32 °C), water progressively changes from a good solvent to a poor solvent, resulting in a slight contraction of the PNIPAM chain and a slightly smaller $\langle R_h \rangle$.

2. Around the phase transition temperature (32–35 °C), the PNIPAM chain undergoes the coil-to-globule transition so that $\langle R_h \rangle$ rapidly decreases.

3. At temperatures higher than ~35 °C, the PNIPAM chain is already in its fully collapsed globule state so that further increase of temperature has little effect on $\langle R_h \rangle$.

In the solution with a higher concentration, the intrachain coil-to-globule transition is accompanied by interchain aggregation. When the interchain aggregation is dominant, $\langle R_h \rangle$ increases as temperature increases, leading to a peak in the temperature range of 32–35 °C. At higher temperatures, the interchain aggregation stops because the increase of $R_{vv}(q)/KC$ stops at ~34 °C as shown in Figure 1. Thus the intrachain coil-to-globule transition becomes dominant at temperatures higher than ~34 °C, resulting in the decrease of $\langle R_h \rangle$.

A combination of static and dynamic LLS results leads to microscopic parameters of the stable interchain aggregates at 34 °C, such as the weight average molar mass ($M_{w,agg}$), the average hydrodynamic radius ($\langle R_h \rangle_{agg}$), the average number of the polymer chains inside each aggregate ($\langle N \rangle_{agg}$), the average surface area per ionic group ($\langle S \rangle_{ionic}$), and the average hydrodynamic volume of each polymer chain inside the aggregate ($\langle V \rangle_{chain}$), which are summarized in Table 1. Note that the aggregates formed in different solutions have a very similar $\langle V \rangle_{chain}$, indicating that at a given temperature the average degree of the shrinking of the polymer chains is similar in spite of the interchain aggregation, so that the aggregates formed in different solutions have a similar density. This result clearly indicates that the intrachain coil-to-globule transition and the interchain aggregation are two *independent*, but *competing*, processes.

Table 2 summarizes the LLS results of the aggregates formed in different PNIPAM-0.8KAA solutions at 45 °C. The ratio of $\langle R_g \rangle/\langle R_h \rangle$ is in the range of 0.73–0.84, indicating that the aggregates are uniform spheres [57]. The average density $\langle \rho \rangle$ of the aggregates decreases as the aggregation number

Table 1. LLS results of PNIPAM-0.8KAA aggregates formed at 34 °C.

C (g/mL)	$M_{w, agg}$ (g/mol)	$\langle N \rangle_{agg}$	$\langle R_h \rangle$ (nm)	$\langle S \rangle_{ionic}$ (nm²)	$\langle V \rangle_{chain}$ (nm³)
5.0×10^{-4}	7.68×10^7	17	87	17.8	1.62×10^5
1.0×10^{-4}	3.88×10^7	8	68	20.9	1.64×10^5
9.4×10^{-6}	1.86×10^7	4	54	26.3	1.64×10^5
4.7×10^{-6}	4.97×10^6	1	35	49.1	1.80×10^5

Reprinted with permission from [116], X. Qiu et al., *J. Polym. Sci., Part B: Polym. Phys.* 36, 1501 (1998). © 1998, John Wiley & Sons, Inc.

Figure 3. Temperature dependence of the average surface area $\langle S \rangle_{ionic}$ per ionic group on the PNIPAM-0.8KAA aggregates, where $\langle S \rangle_{ionic}$ is defined as $4\pi \langle R_h \rangle^2 / \langle N \rangle_{ionic}$. Reprinted with permission from [116], X. Qiu et al., *J. Polym. Sci., Part B: Polym. Phys.* 36, 1501 (1998). © 1998, John Wiley & Sons, Inc.

$\langle N \rangle_{agg}$ decreases, which may be attributed to the imperfect packing of the polymer chains inside the aggregate when there are only one or two chains inside each aggregate [58]. In the case of $\langle N \rangle_{agg} > 8$, $\langle \rho \rangle \sim 0.34$ g/cm³, very close to the value of the neutral PNIPAM aggregates reported by Ricka et al. [59]. For the single-chain globule, $\langle \rho \rangle \sim 0.20$ g/cm³, very close to what we found in the case of the PNIPAM homopolymer [55], indicating that the ionic groups are on the surface of the aggregates and have nearly no effect on the coil-to-globule transition.

We can reasonably picture that in the coil-to-globule transition the PNIPAM segments between two neighboring ionic groups collapse and associate with each other, while all the ionic groups stay on the surface of the aggregates to act as a stabilizer. As the aggregation proceeds, for the aggregates with a uniform density, the number of the ionic groups on each particle is proportional to the mass of the aggregate (M_{agg}) or the cubic of the size, while the surface area of the aggregate is only proportional to the square of the size or $M_{agg}^{2/3}$. Therefore, the surface area per ionic group is proportional to $M_{agg}^{-1/3}$ (i.e., $\langle S \rangle_{ionic} \propto M_{agg}^{-1/3}$), indicating that $\langle S \rangle_{ionic}$ decreases as the aggregation proceeds. At the same time, the intrachain coil-to-globule transition also leads to the decrease of $\langle S \rangle_{ionic}$.

Figure 3 shows a sharp decrease of $\langle S \rangle_{ionic}$ in the temperature range of 32.5–33 °C, which exactly corresponds to the slow down of the interchain aggregation [the increase of $R_{vv}(\theta)/KC$] shown in Figure 1 and to the peak position of $\langle R_h \rangle$ shown in Figure 2. Logically, there is a minimum value of $\langle S \rangle_{ionic}$, at which the surface of the aggregates is "fully covered" by the ionic groups, so that further aggregation is impossible because of the ionic repulsion between different aggregates. However, the intrachain coil-to-globule transition inside the aggregates continues. This is exactly why $\langle R_h \rangle$ in Figure 2 first increases and then decreases, but $\langle S \rangle_{ionic}$ in

Figure 3 only decreases. Note that for aggregates with different sizes formed in different solutions, $\langle S \rangle_{ionic}$ approaches a similar value at high temperatures. This is reasonable because hydrophobic particles have a tendency to aggregate in water. The stabilizers (here the ionic groups) can reduce the surface energy. When the surface per stabilizer decreases to a certain value, that is, the surface reaches a certain degree of coverage, the aggregation stops and the particles will be stabilized. For a given type of interface (here particle–water), this value should be a constant, independent of the particle size. Therefore, $\langle S \rangle_{ionic}$ is a fundamental parameter that governs the size of the aggregates.

Figures 4 shows that in spite of the large difference in ionic content, PNIPAM-4.5KAA exhibits intrachain collapsing and interchain aggregation similar to PNIPAM-0.8KAA. In the extremely dilute solution ($C = 5.0 \times 10^{-6}$ g/mL), the collapsing process involves only the intrachain coil-to-globule transition. Note that the degree of aggregation of PNIPAM-4.5KAA

Table 2. LLS results of PNIPAM-0.8KAA particles formed at 45 °C.

C (g/mL)	M_w (g/mol)	$\langle N \rangle_{agg}$	$\langle R \rangle_h$ (nm)	$\langle R_g \rangle / \langle R_h \rangle$	$\langle \rho \rangle$ (g/cm³)
5.0×10^{-4}	7.88×10^7	17	45.6	0.78	0.34
1.0×10^{-4}	4.08×10^7	8	36.6	0.73	0.34
9.4×10^{-6}	1.86×10^7	4	30.6	0.75	0.28
4.7×10^{-6}	4.97×10^6	1	21.5	0.84	0.20

Reprinted with permission from [116], X. Qiu et al., *J. Polym. Sci., Part B: Polym. Phys.* 36, 1501 (1998). © 1998, John Wiley & Sons, Inc.
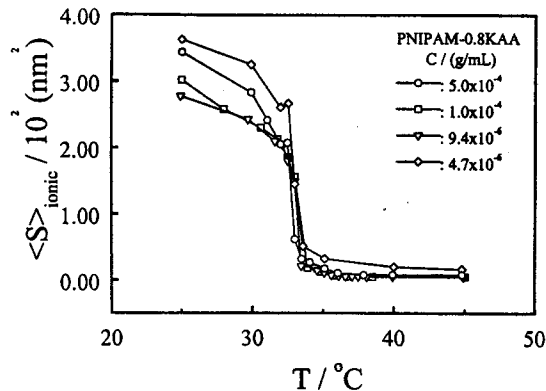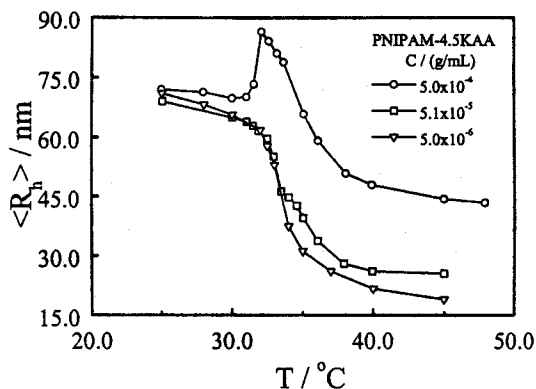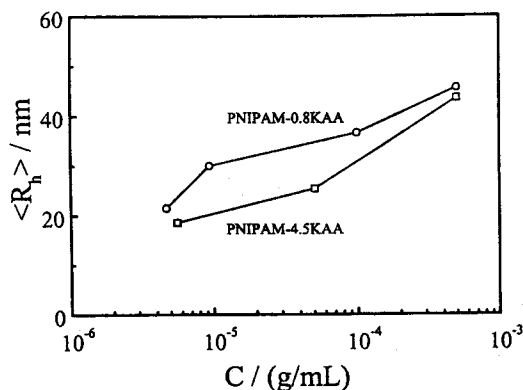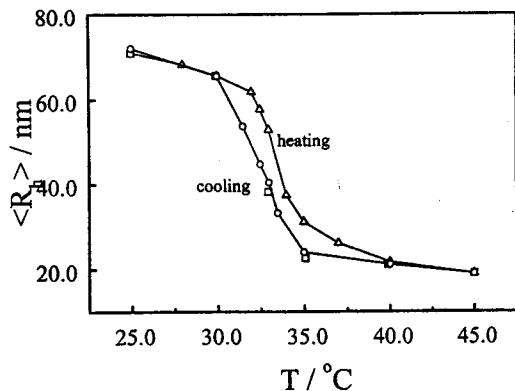

Figure 4. Temperature and concentration dependence of the average hydrodynamic radius $\langle R_h \rangle$ of PNIPAM-4.5KAA in deionized water. Reprinted with permission from [116], X. Qiu et al., *J. Polym. Sci., Part B: Polym. Phys.* 36, 1501 (1998). © 1998, John Wiley & Sons, Inc.

Figure 5. Comparison of the average size of the aggregates formed in the PNIPAM-0.8KAA and PNIPAM-4.5KAA solutions. Reprinted with permission from [116], X. Qiu et al., *J. Polym. Sci., Part B: Polym. Phys.* 36, 1501 (1998). © 1998, John Wiley & Sons, Inc.

is lower than that of the low ionic PNIPAM-0.8KAA, which is reflected by the smaller size (Fig. 5) and smaller aggregation peak formed in the PNIPAM-4.5KAA solution with a similar concentration. This is reasonable because PNIPAM-4.5KAA has a higher ionic content and requires a much lower degree of aggregation to reach the same minimum value of $\langle S \rangle_{\text{ionic}}$ as in the case of PNIPAM-0.8KAA.

Figure 6 shows that $\langle R_h \rangle$ returns to the starting point when the solution is cooled to 25 °C, indicating that the solution returns to its initial state in which all the ionomers exist as individual chains. On the other hand, the heating rate independence of $\langle R_h \rangle$ at 45 °C implies that the solution at 45 °C is in a thermodynamic equilibrium state. However, around the coil-to-globule transition temperature (32–34 °C), $\langle R_h \rangle$ in the heating process is different from that in the cooling process, that is,

there is a hysteresis, which can be attributed to the association of different segments (presumably through the hydrogen bonding) in the globule state that persist at the temperature around the transition in the cooling process, so that $\langle R_h \rangle$ is smaller. When the temperature is lower than 25 °C, water becomes such a good solvent that all the intersegmental structures are destroyed and $\langle R_h \rangle$ returns to its initial preheating value.

2.2. Swelling and Shrinking Behavior of Linear P(VCL-*co*-NaA) Chains and Microgels

Poly(*N*-vinylcaprolactam) (PVCL) is a relatively new type of nonionic water-soluble polymer. It was developed for hair-care and cosmetic applications. In principle, it should be more bio-compatible than PNIPAM. It is known that PVCL can complex with organic compounds [60–64] and resist hydrolysis [65], and its gel can undergo a continuous volume transition in the temperature range 25–36 °C [66]. Only a few studies on PVCL and its gels have been reported, partially because its polymerization is relatively difficult and partially because its volume transition is not as sharp as that of the PNIPAM gels. However, its biocompability attracted us to initiate a study to see whether PVCL microgels can be used as an injecting composition for certain biomedical applications. Table 3 summarizes static and dynamic LLS results of linear poly(*N*-vinylcaprolactam-*co*-sodium acrylate) [(PVCL-*co*-NaA)] chains and spherical microgels with different NaA content in swollen (27 °C) and collapsed (50 °C) states. In each case, M_w is independent of the temperature, indicating no interchain or no interparticle aggregation. As expected, the linear chains have a larger change in $\langle R_h \rangle$ than the microgels. For the linear chains, the decrease of $\langle R_g \rangle/\langle R_h \rangle$ from 1.33 to 0.82 indicates that a coil-to-globule transition in the chain conformation presumably leads to a single-chain core–shell nanostructure or a single-chain micelle as shown in Figure 7. On the other hand, the shrinkage of the microgels as the temperature increases was relatively smooth, similar to the
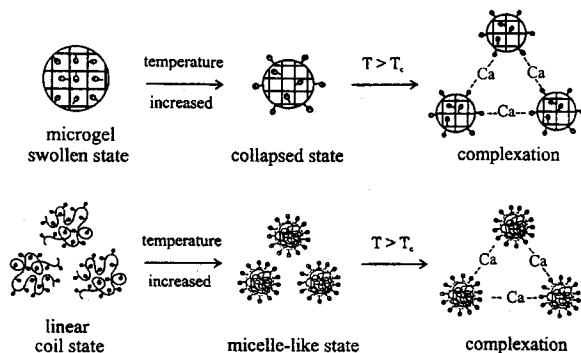

Figure 6. Temperature dependence of $\langle R_h \rangle$ of a dilute PNIPAM-4.5KAA solution ($C = 5.0 \times 10^{-6}$ g/mL) in the slow heating and cooling. □ represents the solution jumped from 25 to 45 °C in a single step and then slowly cooled to each measurement temperature; △ and ○ represent the solution slowly heated to each measurement temperature from 25 to 45 °C and then slowly cooled to each measurement temperature. Every data point was obtained after thermodynamic equilibrium. Reprinted with permission from [116], X. Qiu et al., *J. Polym. Sci., Part B: Polym. Phys.* 36, 1501 (1998). © 1998, John Wiley & Sons, Inc.

Table 3. LLS characterization of linear P(VCL-*co*-NaA) chains and spherical microgels in deionized water.

	L-P(VCL-4.6A)			G-P(VCL-1.0A)		
T (°C)	$M_w \times 10^6$ (g/mol)	$\langle R_h \rangle$ (nm)	$\langle R_g \rangle/\langle R_h \rangle$	$M_w \times 10^9$ (g/mol)	$\langle R_h \rangle$ (nm)	$\langle R_g \rangle/\langle R_h \rangle$
27	3.03	73	1.33	1.34	330	0.70
37	3.02	33	0.92	1.40	191	0.73
50	3.06	25	0.82	1.42	134	0.85
	G-P(VCL-4.3A)			G-P(VCL-9.1A)		
	$M_w \times 10^9$ (g/mol)	$\langle R_h \rangle$ (nm)	$\langle R_g \rangle/\langle R_h \rangle$	$M_w \times 10^9$ (g/mol)	$\langle R_h \rangle$ (nm)	$\langle R_g \rangle/\langle R_h \rangle$
27	2.22	355	0.87	5.54	515	1.29
37	2.10	229	0.88	5.41	371	0.91
50	2.13	177	0.92	5.21	272	1.11

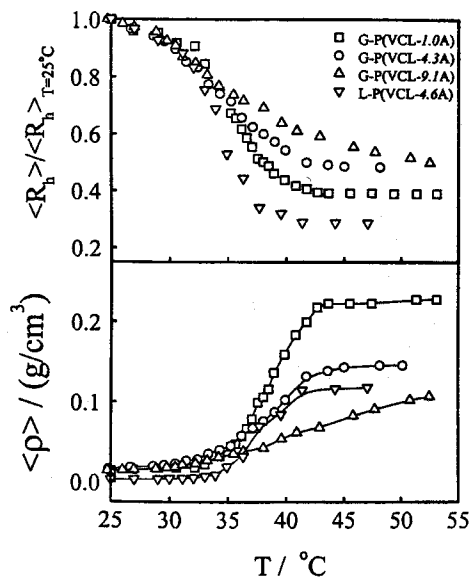**Figure 7.** Schematic of the temperature dependence of linear P(VCL-co-NaA) chains and spherical microgels in the presence of Ca^{2+}. Reprinted with permission from [164], S. Peng and C. Wu, *J. Phys. Chem. B* 105, 2331 (2001). © 2001, American Chemical Society.

temperature-induced volume change of neutral PVCL microgels [66]. However, the ionic groups make the PVCL chain more hydrophilic, which leads to a higher swelling extent at lower temperatures, shifts the shrinking temperature higher, and results in a less compact globule [67, 68]. The increase of $\langle R_g \rangle / \langle R_h \rangle$ as the ionic content increases indicates further swelling of the microgels.

Figure 8 clearly show that the shrinkage of the linear chains is more than that of the microgels. The relative shrinkage of the microgels decreases as the ionic content increases. Note that in the temperature range studied, there was no change in M_w in any case, that is, no intermicrogel aggregation in

Figure 8. Temperature dependence of the relative average hydrodynamic radius $\langle R_h \rangle / \langle R_h \rangle_{T=25\,°C}$ and the average chain density $\langle \rho \rangle$ for linear P(VCL-co-NaA) chains and spherical microgels copolymerized with different amounts of NaA, where $\langle R_h \rangle_{T=25\,°C}$ is the average hydrodynamic radius $\langle R_h \rangle$ at 25 °C. Reprinted with permission from [164], S. Peng and C. Wu, *J. Phys. Chem. B* 105, 2331 (2001). © 2001, American Chemical Society.

the shrinking process. Figure 8 shows a better view of the shrinkage of the linear chains and microgels in terms of the average chain density $\langle \rho \rangle$ defined as $M_w / ((4/3)\pi \langle R_h \rangle^3)$. In both swollen and collapsed states, the linear chains have a lower density than the microgels because cross-linking limits the swelling of the gel network. Except for the microgels with the highest ionic content, both the linear chains and the microgels reached their corresponding collapsed states at 42 °C. The slow increase of $\langle \rho \rangle$ for the P(VCL-9.1A) microgels can be attributed to a balance between strong electrostatic repulsion and hydrophobic attraction. Using $\langle \rho \rangle$ at 25 °C as a reference, we found that $\langle \rho \rangle$ increased ~40 times for the linear chains, but only 8–16 times for the microgels, depending on the ionic content.

3. SALT-INDUCED THERMOREVERSIBLE AND CONTROLLABLE COMPLEXATION

It is known that certain alkaline earth ions and heavy metal ions can specifically interact with carboxylic groups [69, 70]. If carboxylic groups are attached to a polymer chain backbone, as in polyacrylic acid and its copolymers, this interaction can lead to cation–polyanion "complexation" even at a very low cation concentrations [71]. Furthermore, some polyanions can complex with protein, in which metal ions act as cross-linking agents. Long ago, Wall and Drenan [72] investigated the Ca^{2+}-, Ba^{2+}-, and Sr^{2+}-induced precipitation of polyacrylates and interpreted their results as gelation via bond formation between the polyelectrolyte chains and cations. Flory and Osterheld [73] pointed out that Ca^{2+} could induce a more profound chain contraction of partly neutralized polyacrylates than an equivalent amount of Na^+. More recent studies have revealed some important roles of metal ions, such as Cu^{2+}, Zn^{2+}, and Fe^{3+}, in the functional activity of immunocomponent cells [74–77]. It has been suggested that the addition of metal ions to an aqueous solution of polyanions alters the hydration, that is, disrupts oriented water molecules near the chain [78–80].

3.1. Ca^{2+}-Induced Complexation of P(VCL-co-NaA)

Figure 9 shows typical hydrodynamic radius distributions of spherical microgels and linear chains at 25 °C before and after adding Ca^{2+}. It shows that both microgels and linear chains are reasonably narrowly distributed. The relative distribution widths $(\mu_2 / \langle \Gamma \rangle^2)$ for spherical microgels and linear chains are ~0.05 and ~0.18, respectively. The addition of Ca^{2+} led to shrinking of both spherical microgels and linear chains. However, it should be stated that the addition of Ca^{2+} did not alter the scattering intensity. Therefore, the shrinkage of spherical microgels and linear chains can be, respectively, attributed to intraparticle and intrachain Ca^{2+}/COO^- complexation. For each $f(R_h)$, we were able to calculate one average hydrodynamic radius $\langle R_h \rangle$ by using $\langle R_h \rangle = \int_0^0 f(R_h) R_h \, dR_h$.
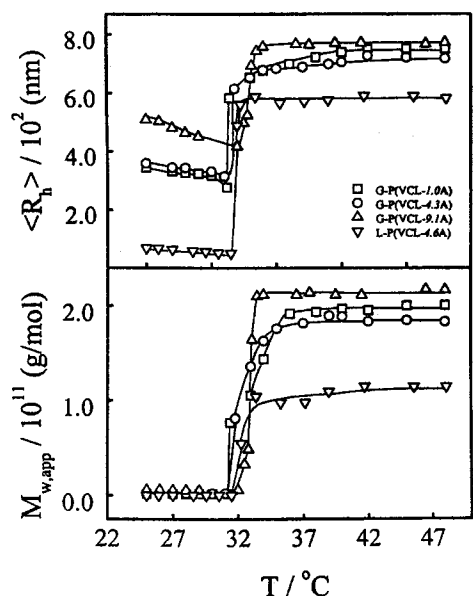
Figure 10 shows the temperature dependence of the average hydrodynamic radius $(\langle R_h \rangle)$ and the apparent weight average molar mass $(M_{w,\,app})$ of the linear chains and microgels
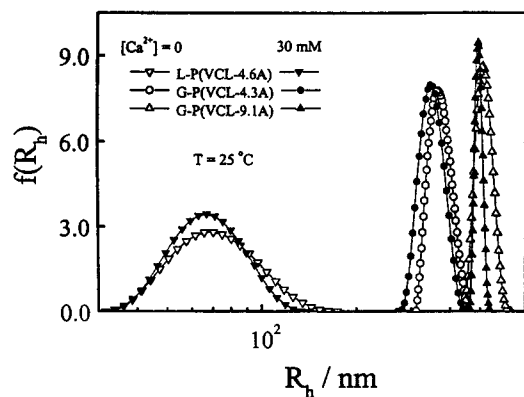
Figure 9. Typical hydrodynamic radius distributions of P(VCL-*co*-NaA) spherical microgels and linear chains at 25 °C with and without the addition of Ca^{2+}. Reprinted with permission from [164], S. Peng and C. Wu, *J. Phys. Chem. B* 105, 2331 (2001). © 2001, American Chemical Society.

in 0.03 M $CaCl_2$ aqueous solution. In the range 25–31.8 °C, the microgels shrink as the temperature increases, but $M_{w, app}$ is independent of the temperature, indicating no intermicrogel aggregation. At ~32 °C, the average hydrodynamic size and the apparent weight average molar mass sharply increase, revealing a clear intermicrogel aggregation.

Figure 11 shows that for the linear chains, the average number of chains inside each complex particle (N_{agg}) is as high as ~4 × 10⁴, whereas for the microgels, N_{agg} is much less, only in the range of 40–200. This is understandable because the linear chains can entangle and complex with each other via the inter-
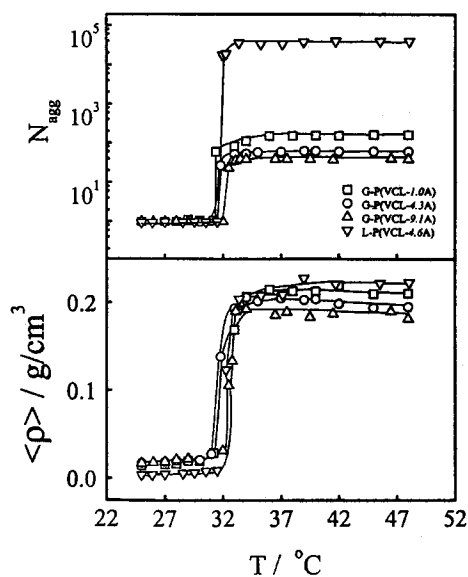
Figure 11. Temperature dependence of the average number of aggregation (N_{agg}) and the average chain density $\langle \rho \rangle$ of linear P(VCL-*co*-NaA) chains and spherical microgels in the presence of Ca^{2+}, where $[Ca^{2+}] = 0.03$ M. Reprinted with permission from [164], S. Peng and C. Wu, *J. Phys. Chem. B* 105, 2331 (2001). © 2001, American Chemical Society.
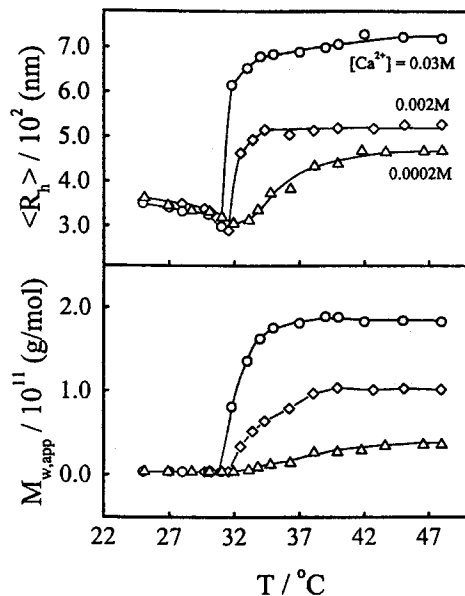
action between Ca^{2+} and $-COO^-$ to form a hyperbranched structure, whereas for the microgels, when the temperature reaches the transition temperature, PVCL becomes hydrophobic and the microgel starts to collapse, but the hydrophilic $-COO^-$ groups tend to stay on the periphery of the microgel. The complexation between Ca^{2+} and $-COO^-$ sticks the microgels together and the complexation occurs in a narrow temperature range.

Figure 11 also shows that the resultant complexes have a similar average chain density $\langle \rho \rangle$ of ~0.2 g/cm³, in spite of a big difference in N_{agg}. A slight decrease of $\langle \rho \rangle$ as the ionic content increases can be attributed to the fact that the chains with more ionic groups are more hydrophilic and collapse less at high temperatures. The higher $\langle \rho \rangle$ of the linear chains is related to chain entanglement. Note that both the linear chains and the microgels have an amphiphilic character at higher temperatures. The shrinkage of each linear chain forces most of the ionic groups to form a relatively more hydrophilic periphery, similar to a micelle [81–84], whereas in the case of the microgels, most of the ionic groups are trapped inside the microgel due to cross-linking, so that there are less chances to form the intermicrogel complexes, which explains why N_{agg}(microgel) is much lower than N_{agg}(liner chain) and why N_{agg}(microgel) decreases as the ionic content increases.
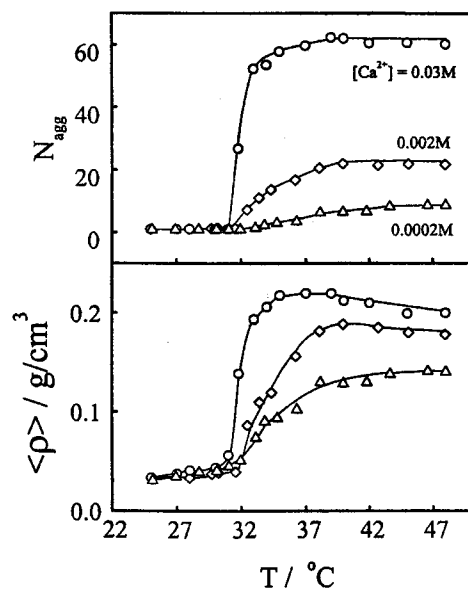
Figure 12 shows the temperature dependence of the average hydrodynamic radius $\langle R_h \rangle$ and the apparent weight average molar mass ($M_{w, app}$) for P(VCL-4.3A) microgels in the presence of different amounts of Ca^{2+}. Note that the complexation occurs at a similar temperature in spite of a variation of Ca^{2+} concentration, but both $\langle R_h \rangle$ and $M_{w, app}$ increase as $[Ca^{2+}]$ increases. The increase of ionic content has little effect on

Figure 10. Temperature dependence of the average hydrodynamic radius $\langle R_h \rangle$ and the apparent weight average molar mass ($M_{w, app}$) of linear P(VCL-*co*-NaA) chains and spherical microgels in the presence of Ca^{2+}, where $[Ca^{2+}] = 0.03$ M. Reprinted with permission from [164], S. Peng and C. Wu, *J. Phys. Chem. B* 105, 2331 (2001). © 2001, American Chemical Society.

Figure 12. Temperature dependence of the average hydrodynamic radius $\langle R_h \rangle$ and apparent weight average molar mass $(M_{w, app})$ of P(VCL-4.3A) microgels with different Ca^{2+} concentrations. Reprinted with permission from [164], S. Peng and C. Wu, *J. Phys. Chem. B* 105, 2331 (2001). © 2001, American Chemical Society.

$\langle R_h \rangle$. Figure 13 shows that the average numbers of microgels inside each intermicrogel complex (N_{agg}) are ~60, ~20, and ~8, respectively, for $[Ca^{2+}] = 3 \times 10^{-2}$, 2×10^{-3}, and 2×10^{-4} M. The average chain density $\langle \rho \rangle$ of the complexes

Figure 13. Temperature dependence of the average number of aggregation (N_{agg}) and the average chain density $\langle \rho \rangle$ of P(VCL-4.3A) microgels with different Ca^{2+} concentrations. Reprinted with permission from [164], S. Peng and C. Wu, *J. Phys. Chem. B* 105, 2331 (2001). © 2001, American Chemical Society.

decreases as N_{agg} decreases, perhaps due to an imperfect packing of larger microgels inside each complex, especially when each complex is only made of approximately eight microgels.

3.2. Cation-Induced Complexation of P(VCL-co-NaA) Microgels

The aggregation induced by different kinds of cations and at different temperatures was investigated. Table 4 summarizes the laser light-scattering results of P(VCL-co-NaA) microgels in deionized water and in different 0.01 N salt solutions. It is clear that Na^+ has the weakest effect on the microgels, whereas Hg^{2+} leads to a profound shrinkage. This is understandable because the presence of monovalent Na^+ can only increase the ionic strength and reduce electrostatic repulsion between carboxylic groups. In addition to the influence on ionic strength, divalent cations can also pull two carboxylic groups together so that they can induce a larger shrinkage of the microgels. The fact that the molar mass of the microgels $(M_{w, microgel})$ remains a constant indicates no interparticle complexation; in other words, the interaction between cations and microgels at 25 °C is purely intramicrogel. The decrease of $\langle R_g \rangle / \langle R_h \rangle$ indicates that the shrinkage of the microgel reduces the hydrodynamic draining. Table 4 shows that in terms of the effect of different cations on the shrinkage of the microgels, $Hg^{2+} \gg Cu^{2+} > Ca^{2+}$. Such an effect can be better viewed in terms of the cation concentration dependence of $\langle R_g \rangle$ and $\langle R_h \rangle$.

Figure 14 shows a clear shrinkage of the microgels as the cation concentration is increased. There exist at least four interactions in the mixture of cations and polyanions: the hydrophobic attraction among the hydrocarbon backbone chains, the hydration of the polymer chain, the electrostatic repulsion between carboxylic groups, and the electrostatic attraction (or complexation) among divalent cations and carboxylic groups. The balance of these interactions determines whether the microgel is in the swelling or shrinking state. It is clear that the addition of cations not only increases the ionic strength (reduces the electrostatic repulsion), but also leads to possible complexation, depending on the kind of cation used. The shrinkage of the microgels can also be viewed in terms of the ratio of $\langle R_g \rangle / \langle R_h \rangle$. It is known that for a uniform nondraining sphere, $\langle R_g \rangle / \langle R_h \rangle \sim 0.774$. The hydrodynamic

Table 4. LLS results of P(VCL-co-SA) microgels in different 0.01 N cation solutions at 25 °C.[a]

Cationic ions	$\langle R_h \rangle$ (nm)	$\langle R_g \rangle$ (nm)	$\langle R_g \rangle / \langle R_h \rangle$	$M_{w, microgel}$ (10^{-8} g/mol)
No cation	258	221	0.86	8.3
Na^+	242	216	0.89	8.5
Ca^{2+}	237	200	0.85	8.9
Cu^{2+}	223	180	0.81	8.4
Hg^{2+}	195	146	0.75	8.0

Reprinted with permission from [165], S. Peng and C. Wu, *Polymer* 42, 6871 (2001). © 2001, Elsevier Science.
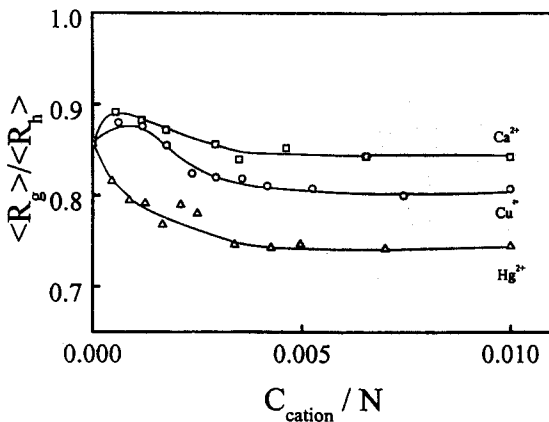
[a] Relative errors: $\langle R_h \rangle$, ±2%; $\langle R_g \rangle$, ±5%; $\langle R_g \rangle / \langle R_h \rangle$, ±7%; $M_{w, microgel}$, ±5%.
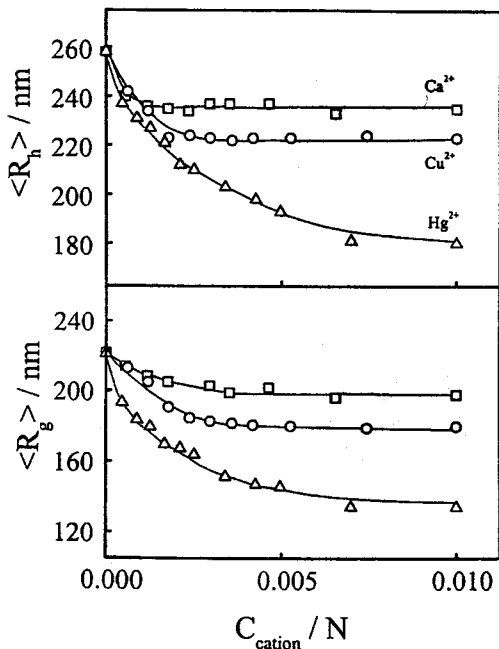
...ining results in a relatively smaller $\langle R_h \rangle$ and a large ratio $\langle R_g \rangle / \langle R_h \rangle$.

Figure 15 shows that $\langle R_g \rangle / \langle R_h \rangle$ decreases as the cation ...centration is increased, indicating that the shrinkage of ... microgels reduces the hydrodynamic draining. When the ...ion concentration reaches ~0.005 N, $\langle R_g \rangle / \langle R_h \rangle$ approaches ...ferent constants in the presence of different cations. Note ...t for Ca^{2+} and Cu^{2+}, $\langle R_g \rangle / \langle R_h \rangle$ increases slightly in the ... cation concentration range. A comparison of the decreases ... $\langle R_g \rangle$ and $\langle R_h \rangle$ in Figure 14 shows that $\langle R_h \rangle$ decreases faster ...n $\langle R_g \rangle$ in this range. This could be attributed to the col-

lapse of the rough surface of the microgel. Figure 15 shows that Hg^{2+} is the most effective in induction of shrinkage and reduction of hydrodynamic draining. As $[Hg^{2+}]$ is increased, $\langle R_g \rangle / \langle R_h \rangle$ decreases from 0.86 to ~0.75, indicating that the microgels are collapsed and become nondraining at $[Hg^{2+}] > $ ~0.0025 N.
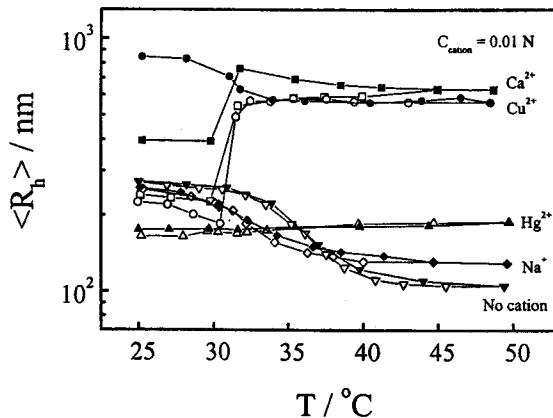
Figures 16 and 17 show the temperature dependence of the average hydrodynamic radius $\langle R_h \rangle$ and the weight average molar mass $M_{w, aggregate}$ of the P(VCL-co-NaA) microgels, respectively, in heating and cooling conditions. Note that in the presence of Na^+, $\langle R_h \rangle$ gradually decreases as the temperature is increased, but the molar mass remains a constant, indicating that there is no intermicrogel aggregation. The shrinkage of individual microgels is due to the intramicrogel hydrophobic attraction. The addition of Ca^{2+} or Cu^{2+} leads to different results; namely, in the range 25–32 °C, the shrinkage of microgels is similar to the case of adding Na^+, but when the temperature reaches ~32 °C, the sharp increases of $\langle R_h \rangle$ and
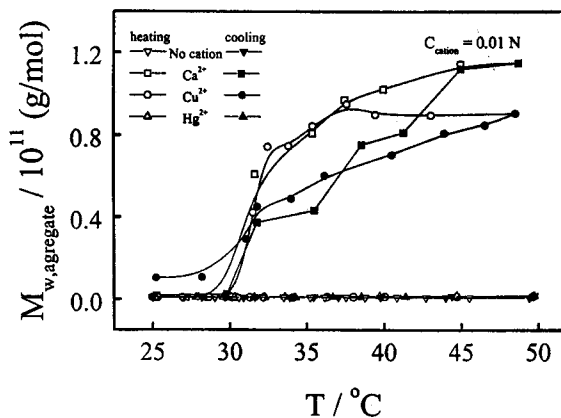
$M_{w, \text{aggregate}}$ clearly reveal an intermicrogel aggregation. However, in the presence of Hg^{2+}, both $\langle R_h \rangle$ and $M_{w, \text{aggregate}}$ are nearly independent of temperature. Presumably, the intermicrogel aggregation is induced by the attraction between one cation and two anionic carboxylic groups on two different microgels. In the presence of 0.01 N Ca^{2+} or Cu^{2+}, each aggregate on average contains $\sim100\text{--}200$ microgels. The different effects of Na^+, Ca^{2+}, Cu^{2+}, and Hg^{2+} on the microgels can be explained as follows.

When the temperature reaches transition, the PVCL chains become hydrophobic and start to collapse, but the hydrophilic COO^- groups tend to stay on the periphery. In the case of Na^+, there is no complexation between COO^- and Na^+, so the Na^+ is not able to pull different microgels together, whereas in the case of Ca^{2+} and Cu^{2+}, the attraction–complexation among one cation and two COO^- groups on the surface of two different microgels leads to aggregation. As for the case of Hg^{2+}, the strong intramicrogel complexation results in complete intramicrogel complexation so that the microgel collapses even at 25 °C. Therefore, no sufficient amount of carboxylic groups are left on the periphery to induce the intermicrogel complexation.

Figures 16 and 17 also show the cation and temperature dependence of $\langle R_h \rangle$ and $M_{w, \text{aggregate}}$ of the aggregates during the cooling processes. A comparison of the heating and cooling processes shows that a hysteresis exists in the first heating and cooling cycle. It is interesting to note that before dropping at ~32 °C, $\langle R_h \rangle$ slightly increases during the cooling, revealing the swelling of individual microgels inside the aggregate. When $T < \sim32$ °C, individual swollen microgels become so hydrophilic that the strength of the attraction between Ca^{2+} and the COO^- groups on the periphery is not sufficient to pull different microgels together. Therefore, most of the aggregates are dissociated at 25 °C. In the case of Cu^{2+}, $\langle R_h \rangle$ increases during the cooling even at temperature lower than 32 °C, revealing that the attraction between Cu^{2+} and COO^- groups is so strong that the dissociation of the aggregates is incomplete. The hysteresis in the change of $M_{w, \text{aggregate}}$ in Figure 17 also shows that the dissociation of the aggregate at lower temperatures is not complete. As expected, for the case of Na^+ and Hg^{2+}, there is no hysteresis in the cooling process. However, as discussed before, the reasons for the temperature independence in these two cases are completely different. Figure 18 shows a schematic of the effects of different cations and temperature on the P(VCL-co-NaA) microgels.

To prove that it is the COO^- groups on the periphery that lead to the intermicrogel aggregation, we changed the order of adding cations and raising the temperature; namely, we first increased the temperature higher than 32 °C and then added different cations. Figure 19 shows that after 0.01 N cations were added at 45 °C, both $\langle R_h \rangle$ and $M_{w, \text{aggregate}}$ increased sharply, clearly showing that adding cations before or after increasing the temperature has completely different results. The observations support our argument that at higher temperatures, the collapse of the microgel forces the COO^- groups
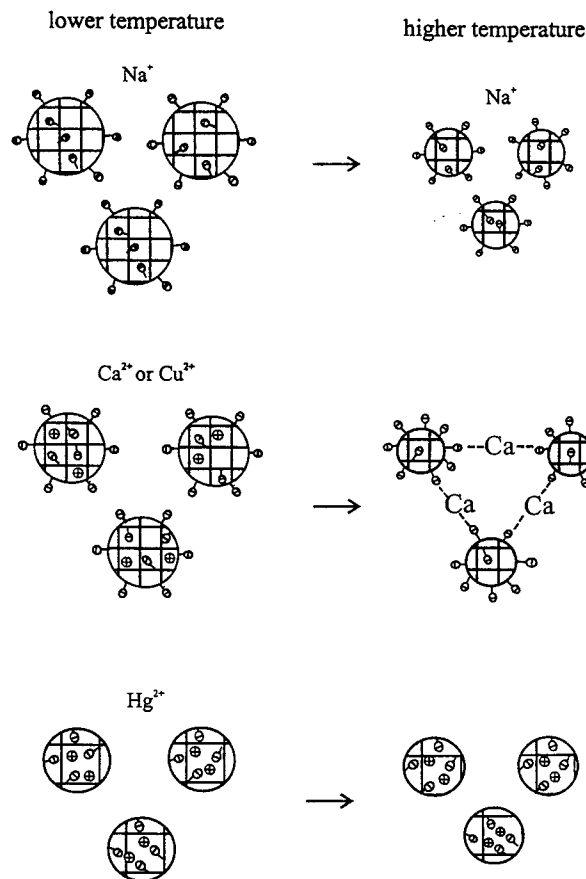
Figure 18. Schematic of the effects of different cations and temperature on the P(VCL-co-NaA) microgels. Reprinted with permission from [165], S. Peng and C. Wu, *Polymer* 42(16), 6871 (2001). © 2001, Elsevier Science.
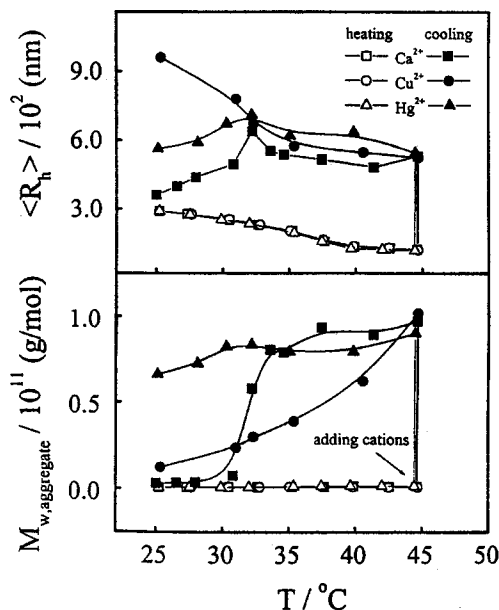
Figure 19. Temperature dependence of the average hydrodynamic radius $\langle R_h \rangle$ and weight average molar mass $M_{w, \text{aggregate}}$ of P(VCL-co-NaA) microgels, where cations were added after the temperature was raised to 45 °C. Reprinted with permission from [165], S. Peng and C. Wu, *Polymer* 42(16), 6871 (2001). © 2001, Elsevier Science.

stay on the periphery so that the intermicrogel complexa-
is enhanced. In the cooling process, there is only a little
teresis for Ca^{2+}, but for Cu^{2+}, $\langle R_h \rangle$ increases even when
temperature is lower than 32 °C. It is interesting to note
for Cu^{2+}, the hysteresis in $M_{w, \text{aggregate}}$ is not as large as
in $\langle R_h \rangle$, revealing a partial dissociation of the aggregates
ower temperatures. In the case of Hg^{2+}, there was a large
teresis during cooling. $M_{w, \text{aggregate}}$ remained nearly constant
ing the cooling process, indicating a strong intermicrogel
plexation between Hg^{2+} and COO$^-$ groups. The fact that
e was nearly no increase of $\langle R_h \rangle$ in the cooling process
aled a strong intramicrogel complexation.

figure 20 shows that after reducing the cation concentra-
to 0.0025 N, the results are quite different from those
wn in Figures 16 and 17, especially, for Hg^{2+}. In the range
32 °C, the shrinkage of the microgels is similar to the
e of adding 0.01 N cations, except for Hg^{2+}. The increases
$R_h \rangle$ and $M_{w, \text{aggregate}}$ in the temperature range ~30–33 °C
cated an intermicrogel aggregation. It is interesting to see
a further increase in temperature results in a decrease in
) even though $M_{w, \text{aggregate}}$ still increases. This is because,
igher temperatures, the effect of intramicrogel hydropho-
attraction is stronger than intermicrogel complexation. In
cooling process, the Ca^{2+}-induced aggregation is essen-
y reversible, but a large hysteresis exists in the Cu^{2+}- or
$^+$-induced aggregation because of a strong complexation
ween Cu^{2+} or Hg^{2+} with COO$^-$ groups. In terms of the
ngth of the complexation between the divalent cations and
O$^-$ groups, it is known that Hg^{2+} ≫ Cu^{2+} > Ca^{2+}. How-

ever, Figure 20 shows that the extent of the intermicrogel
complexation induced by Cu^{2+} is higher than that induced
by Hg^{2+}. This clearly shows that to induce the intermicrogel
complexation, there exists an optimal strength of complexa-
tion between the cation and COO$^-$ groups. If the strength of
the complexation is too strong, the intramicrogel complexa-
tion leads to much less intermicrogel complexation. On the
other hand, if the strength of the complexation is too weak,
the attraction between the cation and COO$^-$ groups is not suf-
ficient to pull different microgels together. Such a trend in
the strength of cation-induced complexation is similar to that
derived from Pearson's concept of hard and soft acids and
bases [85]. Generally, hard acids coordinate better with hard
bases and soft acids coordinate better with soft bases. The
hard base–hard acid interaction is charge-controlled, result-
ing mostly from a favorable electrostatic interaction between
a donor and an acceptor, respectively, with a high and a low
orbital electronegativity. However, the interaction between a
soft acid and a soft base normally leads to covalent coor-
dination of a donor with a low orbital electronegativity and
an acceptor with a high orbital electronegativity [86]. In the
present system, the COO$^-$ groups is a soft base, and the
cations Hg^{2+} and Cu^{2+} are soft acids, but the cation Ca^{2+} is
borderline between hard and soft acids. The Hg^{2+}- or Cu^{2+}-
induced complexation is a typical soft base–soft acid interac-
tion, so it is stronger.

4. ASSOCIATION OF A ZWITTERIONIC POLYCARBOXYBETAINE

Researchers have begun to study more complicated stable
zwitterionic polymers (also known as betaine) because car-
boxybetaine and sulfobetaine are widely used in textile, med-
ical, and other industrial branches [87, 88]. These polymers
are regarded as a well identified class of highly dipolar poly-
meric materials with a wide spectrum of unique and specific
properties. In a zwitterionic polymer, each covalently bonded
anion and cation pair leads to a permanent dipole whose
value can be varied by the intercharge length. Depending on
whether the solution pH is above or below its isoelectric point
(IEP), a zwitterionic polymer in solution could be overall
anionic or cationic. In a zwitterionic polyelectrolyte, polycar-
boxybetaine, poly(N,N-dimethyl ((methacrylamido) propyl)
ammonium propiolactone) (DMMPAPL) [89] in dilute aque-
ous solution, the ζ potential was measured to determine the
pH dependence of the net charge of poly(DMMPAPL) chains
in aqueous solution. Figure 21 shows that poly(DMMPAPL)
has an IEP of pH 8.6. When pH < 8.6, poly(DMMPAPL)
chains are net positively charged. The ζ potential decreases
as the pH increases until pH > 11. The net negative charge
of poly(DMMPAPL) chains at high pH values is due to the
ionization of the carboxylic groups.

Figure 22 shows the temperature dependence of the
weight distribution of the hydrodynamic radius $w(R_h)$ of
poly(DMMPAPL) in deionized water. The $w(R_h)$ has two
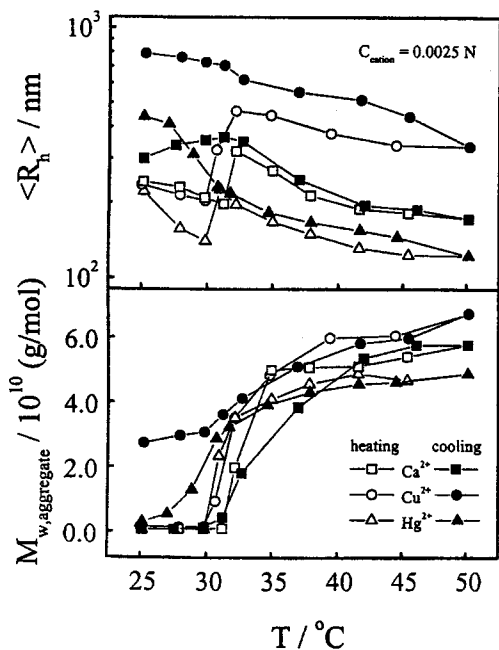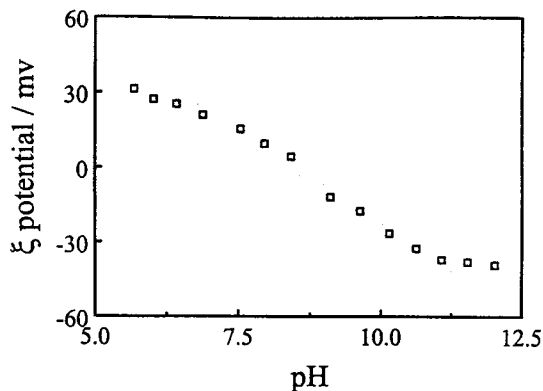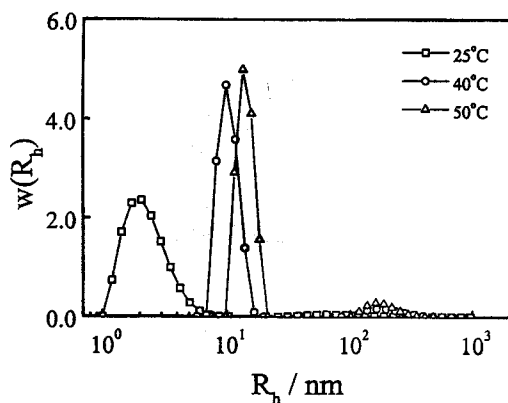peaks at 25 °C. The first peak, located in the range 1~10 nm

re 20. Temperature dependence of the average hydrodynamic radius
and weight average molar mass $M_{w, \text{aggregate}}$ of P(VCL-co-NaA) micro-
where cation concentration is 0.0025 N. Reprinted with permission from
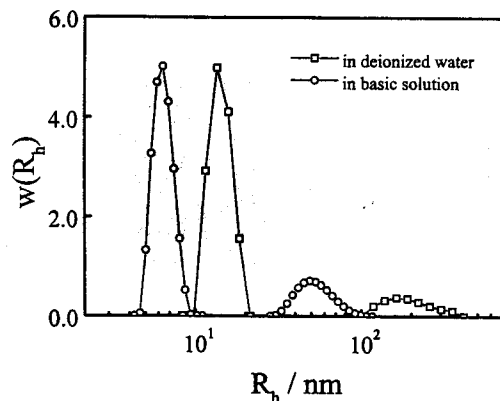, S. Peng and C. Wu, *Polymer* 42(16), 6871 (2001). © 2001, Elsevier
ce.

Figure 21. pH dependence of the ζ potential of poly(DMMPAPL) in 1 mM potassium nitrate aqueous solution. Reprinted with permission from [166], A. Niu et al., *Macromolecules* 33, 3492 (2000). © 2000, American Chemical Society.

Figure 23. Comparison of the weight distribution of the hydrodynamic radius $w(R_h)$ of poly(DMMPAPL) in deionized water and in aqueous solution (pH 12) at 50 °C, where $C = 4.65 \times 10^{-5}$ g/mL. Reprinted with permission from [166], A. Niu et al., *Macromolecules* 33, 3492 (2000). © 2000, American Chemical Society.

corresponds to individual chains, whereas the second broad peak can be related to larger interchain aggregates. The static light-scattering measurments revealed a 10-times higher apparent weight average molar mass (M_w), clearly indicating interchain aggregation. Therefore, in deionized water, poly(DMMPAPL) exists as a mixture of individual chains and interchain associations due to its zwitterionic nature. As the temperature increases, the first peak shifts into the range 7~20 nm, whereas the second peak becomes narrower. The shift of the first peak can be attributed to the break up of the intrachain association and the extension of individual chains.

Figure 23 shows that adjusting the pH to 12 shifts the two peaks toward the left (small R_h direction) because, on the one hand, the addition of NaOH completely ionizes the carboxylic groups and reduces the hydrogen bonding so that the interassociation is suppressed. This leads to the shift of the second peak. On the other hand, the presence of NaOH increases

the ionic strength and decreases electrostatic repulsion so that individual chains contract, resulting in the shift of the first peak.

Figure 24 reveals that the addition of a very small amount of NaCl into the solution at pH 12 leads to a decrease of the hydrodynamic radius and molar mass. This indicates a further dissociation of the interchain association, because of higher ionic strength and weaker electrostatic attraction between —R$_4$N$^+$ and —COO$^-$ groups. Both $\langle R_h \rangle$ and $(M_w)_{app}$

Figure 22. Temperature dependence of the weight distribution of the hydrodynamic radius $w(R_h)$ of poly(DMMPAPL) in deionized water when $C = 4.65 \times 10^{-5}$ g/mL. Reprinted with permission from [166], A. Niu et al., *Macromolecules* 33, 3492 (2000). © 2000, American Chemical Society.
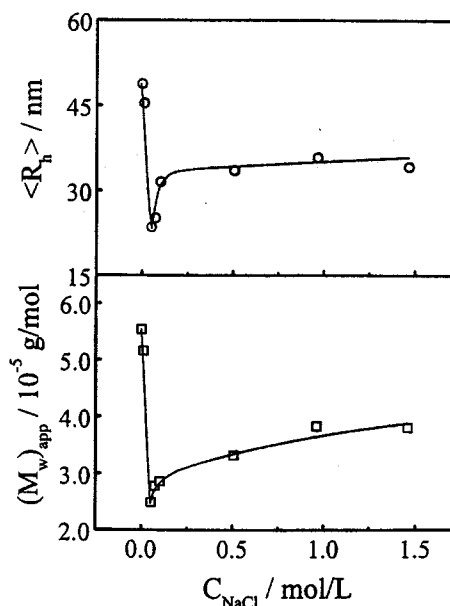
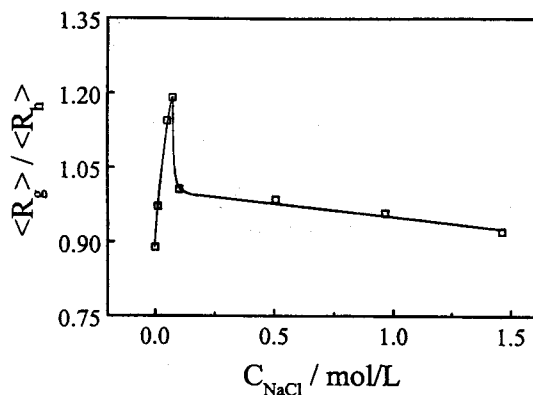Figure 24. NaCl concentration dependence of the average hydrodynamic radius $\langle R_h \rangle$ and apparent weight average molar mass of poly(DMMPAPL) in aqueous solution (pH 12) at 50 °C, where $C_{poly(DMMPAPL)} = 4.65 \times 10^{-5}$ g/mL. Reprinted with permission from [166], A. Niu et al., *Macromolecules* 33, 3492 (2000). © 2000, American Chemical Society.
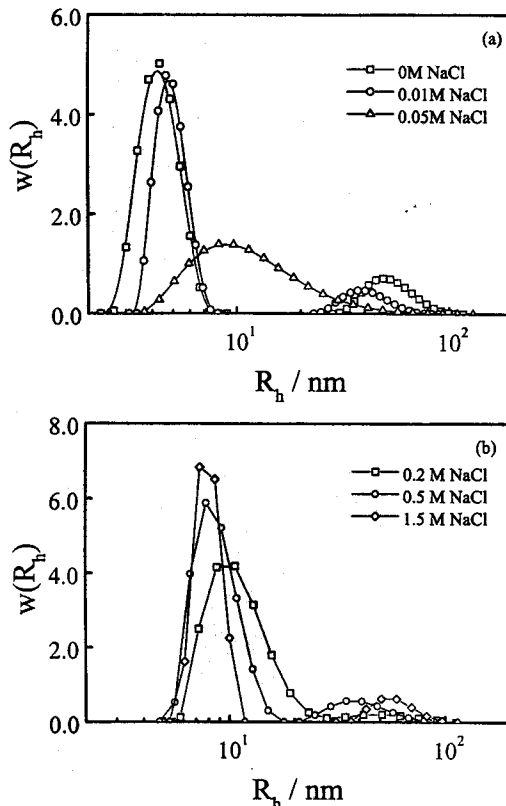
reach their corresponding minimums at $C_{NaCl} \sim 0.05$ M. Further addition of NaCl results in increases of both $\langle R_h \rangle$ and $(M_w)_{app}$. A previous study attributed this increase of $\langle R_h \rangle$ purely to the break up of the intrachain association and the chain extension [90]. However, the increase of molar mass in Figure 24 reveals that there exists an interchain aggregation, which is at least partially attributed to the increase of $\langle R_h \rangle$. Note that in a zwitterionic polymer solution, electrostatic attraction, on the one hand, induces inter- and intrachain associations, but on the other hand, electrostatic repulsion leads to solvation of the polymer chains. Therefore, suppressing electrostatic interactions by the addition of NaCl has a double effect. This is why there is a change from dissociation and extension to aggregation and contraction that accompanies the increase of NaCl concentration. This change can be better viewed from the ratio of $\langle R_g \rangle / \langle R_h \rangle$, which directly reflects the chain conformation.

Figure 25 shows that $\langle R_g \rangle / \langle R_h \rangle$ first increases and then decreases as the NaCl concentration increases. It is known that for a uniform and nondraining sphere, $\langle R_g \rangle / \langle R_h \rangle \sim 0.8$; for a loosely connected hyperbranched chain or aggregate, $\langle R_g \rangle / \langle R_h \rangle \sim 1.0$; for a linear flexible random coil chain, $\langle R_g \rangle / \langle R_h \rangle \sim 1.5$; and for an extended rigid chain, $\langle R_g \rangle / \langle R_h \rangle \geq 2.0$. A combination of Figures 24 and 25 shows that the initial increase of $\langle R_g \rangle / \langle R_h \rangle$ reflects the dissociation of intra- and interchain associations and chain extension because NaCl weakens electrostatic attraction, whereas the decrease of $\langle R_g \rangle / \langle R_h \rangle$ at higher salt concentrations indicates interchain aggregation and intrachain contraction. If the increase of $\langle R_h \rangle$ in Figure 24 is only attributed to the chain extension, we would observe an increase of $\langle R_g \rangle / \langle R_h \rangle$.

Figure 26a shows that the addition of a small amount of NaCl further breaks up inter- and intra-associations because of the increase of ionic strength and electrostatic repulsion, leading to the shift of the aggregation peak toward the small
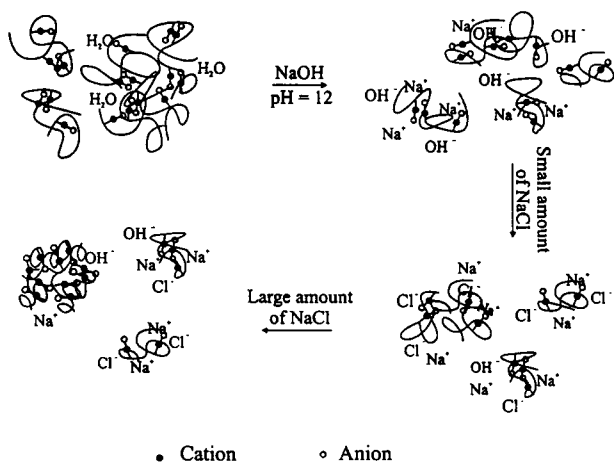

Figure 26. NaCl concentration dependence of the weight distribution of the hydrodynamic radius $w(R_h)$ of poly(DMMPAPL) in aqueous solution ($C_{poly(DMMPAPL)} = 4.65 \times 10^{-5}$ g/mL, pH 12) at 50 °C: (a) $C_{Nacl} \leq 0.05$ M and (b) $C_{NAcl} > 0.05$ M. Reprinted with permission from [166], A. Niu et al., *Macromolecules* 33, 3492 (2000). © 2000, American Chemical Society.

R_h direction. The peaks of the interchain aggregates and individual chains overlap when $C_{Nacl} \sim 0.05$ M. Figure 26b shows that further addition of NaCl leads to the shift of the aggregation peak toward the higher R_h direction, reflecting the decrease of electrostatic repulsion. The further increase of ionic strength results in hydrophobic aggregation of the contracted chains.

Figure 27 shows a schematic of the effects of adding NaOH and NaCl into a zwitterionic poly(DMMPAPL) aqueous solution. The hydrophilic–hydrophobic balance inside a polymer chain is a prime important factor to determine its association behavior in aqueous solution. In deionized water, the zwitterionic polymer chains exist as a mixture of interchain aggregates and individual chains due to the zwitterionic interaction. On the one hand, the addition of NaOH and a small amount of NaCl leads to a higher ionic strength, a weaker electrostatic attraction, and the break up of the inter- and intrachain associations, resulting in smaller interchain aggregates. On the other hand, it decreases both electrostatic repulsion and solvation, and makes the polymer chains more hydrophobic. The hydrophobic attraction results in intrachain contraction and interchain aggregation.

Figure 25. NaCl concentration dependence of the ratio of the average radius of gyration $\langle R_g \rangle$ to the average hydrodynamic radius $\langle R_h \rangle$ of poly(DMMPAPL) in aqueous solution (pH 12) at 50 °C, where $C_{poly(DMMPAPL)} = 4.65 \times 10^{-5}$ g/mL. Reprinted with permission from [166], A. Niu et al., *Macromolecules* 33, 3492 (2000). © 2000, American Chemical Society.

Figure 27. Schematic of the effects of adding NaOH and NaCl into a poly(DMMPAPL) aqueous solution. Reprinted with permission from [166], A. Niu et al., *Macromolecules* 33, 3492 (2000). © 2000, American Chemical Society.

5. SURFACTANT EFFECT ON pH AND TEMPERATURE SENSITIVITIES OF MICROGELS

The swelling and shrinking of a polymeric gel network can be generally attributed to a balance between the repulsion and attraction among functional groups attached to the gel network. These repulsions and attractions can arise from a combination of four intermolecular forces; namely, electrostatic, hydrophobic, van der Waals, and hydrogen bonding [91]. When a repulsive force, usually electrostatic in nature, overcomes an attractive force such as hydrogen bonding or hydrophobic interaction, the gel network swells, sometimes "discontinuously" leading to a volume transition [92]. The variables that can trigger and shift the swelling and shrinking depend on the nature of intermolecular forces that exist in the gel network [93]. Charged groups can be chemically introduced to a hydrophobic gel network, either via hydrolysis or copolymerization with ionic comonomers, to alter its swelling behavior in water and make it sensitive to ionic strength and pH [94].

The interaction between polyelectrolytes and surfactant has been an interesting subject for a long time in both fundamental and technological research [95–98]. Studies of the interaction between a polyelectrolyte's gel network and surfactant have revealed three different controlling effects [99–101]: the translational entropy of counterions, electrostatic interactions, and hydrophobic interactions. It has been shown that the surfactant can form micelles in polymer gels even at a concentration much lower than its critical micelle concentration [98, 102]. This leads to the possibility of using surfactant to change the swelling/shrinking behavior of a thermally sensitive polymer gel instead of a more complicated chemical modification. Therefore, spherical P(VCL-*co*-NaA) microgels were also used to study the surfactant effect on their pH and temperature sensitivities. There are several advantages to using

small microgels over using a bulk gel. For example, equilibrium can be reached in minutes instead of days, and the swelling and shrinking can be monitored by an accurate laser light-scattering spectrometer instead of by eye or a charge-coupled device camera.

Figure 28 shows that when both pH and temperature are fixed, the microgels swell when more surfactant is added. Note that here the surfactant molar concentration (SDS) is well below its critical micelle concentration (CMC $\sim$ 8.0 mM). It is known that SDS can form micelles in the gel network [102, 103], so that electrostatic repulsion between the anionic group (COO^-) on the gel network and anionic surfactant leads to the swelling [104, 105]. Figure 29 shows that the average hydrodynamic radius $\langle R_h \rangle$ increases with SDS. This indicates a concentration of SDS inside the microgels, which can be viewed better in terms of the change of the average number (n_s) of surfactant molecules inside each microgel. n_s can be determined from the increase of the apparent average weight molar mass ($M_{w, app}$) of the microgels; namely, $n_s = (M_{w, app} - M_{w, gel})/M_{surfactant}$, where $M_{w, gel}$ is the average molar mass of the microgels in the absence of surfactant and $M_{surfactant}$ is the molar mass of surfactant. Figure 29 shows that when both pH and temperature are fixed, n_s does increase when more surfactant is added.

It is known that for two like charged groups separated by a distance (r), the electrostatic repulsion force (f) is reciprocally proportional to r^2, that is, $f \propto r^{-2}$. Note that r decreases as n_s increases by $r \propto n_s^{-1/3}$, so that $f \propto n_s^{2/3}$. On the other hand, the swelling deformation is linearly proportional to the repulsion force. Therefore, $\langle R_h \rangle \propto n_s^{2/3}$, which is exactly what we observed in Figure 30, where $\langle V_h \rangle = (4\pi/3)\langle R_h \rangle^3$. Figure 30 clearly reveals, for the first time, that the surfactant-induced swelling can be attributed to the electrostatic repulsion between the anionic surfactant molecules concentrated inside the microgel network.

Figure 31 shows that for a given temperature, the swelling of the microgels as pH increases in the lower pH range is limited. There exists a critical pH at which $\langle R_h \rangle$ rapidly increases
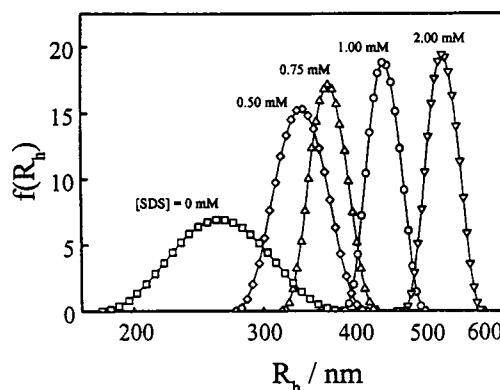

Figure 28. Surfactant concentration (SDS) dependence of the hydrodynamic radius distribution $f(R_h)$ of P(VCL-*co*-NaA) microgels in water at 25 °C and pH 6.2. Reprinted with permission from [167], S. Peng and C. Wu, *Macromolecules* 34, 568 (2001). © 2001, American Chemical Society.

Figure 31. pH dependence of the average hydrodynamic radius $\langle R_h \rangle$ of P(VCL-co-NaA) microgels in the presence of different amounts of surfactant SDS at 25 °C. Reprinted with permission from [167], S. Peng and C. Wu, *Macromolecules* 34, 568 (2001). © 2001, American Chemical Society.
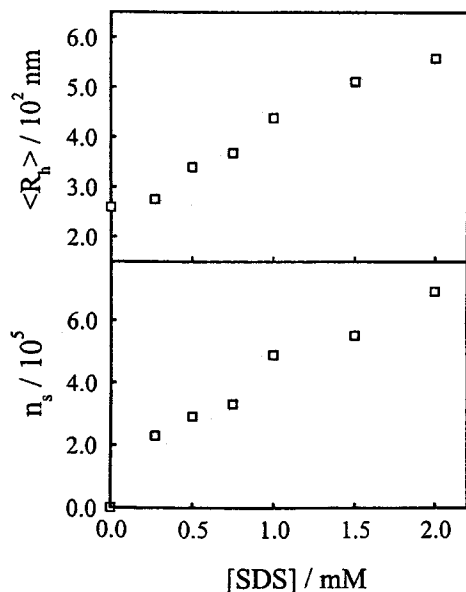
Figure 29. Surfactant concentration (SDS) dependence of the average hydrodynamic radius $\langle R_h \rangle$ of P(VCL-co-NaA) microgels and the average number (n_s) of surfactant molecules concentrated inside each microgel at 25 °C and pH 6.2. Reprinted with permission from [167], S. Peng and C. Wu, *Macromolecules* 34, 568 (2001). © 2001, American Chemical Society.
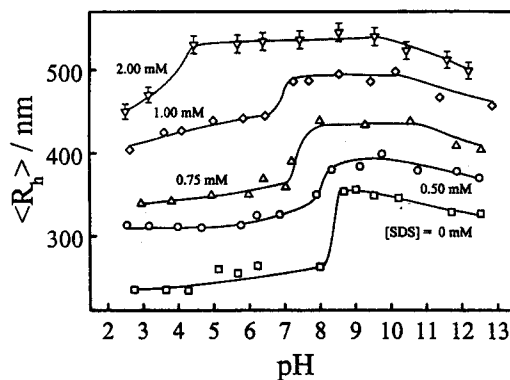
to a maximum. Further increase of pH leads to shrinkage. The critical pH decreases as SDS increases. This is because the binding of SDS to the PVCL chains through hydrophobic interaction converts the microgel into polyelectrolytes. It is these additional charges and their counterions that exert an extra osmotic pressure on the gel network. It is clear that when pH is low, the effect of SDS on the swelling is more profound. It is known that at a lower pH, most of the carboxylic groups are in the acid form (—COOH) and the gel network becomes neutral. The swelling is attributed to the concentra-
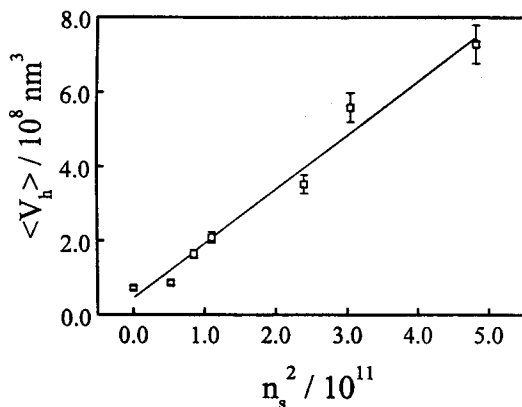
Figure 30. Plot of the average hydrodynamic volume $\langle V_h \rangle$ of P(VCL-co-NaA) microgels versus the square of the average number (n_s) of surfactant molecules concentrated inside each microgel at 25 °C and pH 6.2, where $\langle V_h \rangle = (4\pi/3)\langle R_h \rangle^3$. Reprinted with permission from [167], S. Peng and C. Wu, *Macromolecules* 34, 568 (2001). © 2001, American Chemical Society.

tion of SDS inside the microgel. As pH increases, more and more carboxylic groups become anionic —COO⁻ groups so that the microgel swells even in the absence of SDS. We found that the microgels copolymerized with 1.0 mol% sodium acrylate in the presence of 0.5, 0.75, 1.0, and 2.0 mM SDS have a pH dependence similar to those copolymerized with 3.6, 5.3, 7.1, and 14.2 mol% of sodium acrylate in the absence of SDS, respectively.

The effects of adding surfactant and NaOH are schematically shown in Figure 32. The anionic surfactant concentrated inside the microgel increases the electrostatic repulsion and makes the microgel swell. The addition of NaOH has two opposite effects: (1) to ionize the carboxylic groups and enhance the electrostatic repulsion, and (2) to increase the ionic strength and weaken the electrostatic repulsion. When pH is low, these two effects partially cancel each other so that the swelling is limited. At the critical pH, all the carboxylic groups are ionized. Further addition of NaOH can only enhance the second effect, which explains the shrinkage of the microgel in the high pH range.

Figure 33 shows that for a given SDS concentration, the microgels gradually shrink when the temperature is raised. This is because the increase of temperature weakens the hydration so that the chain backbone gradually becomes more hydrophobic, but the temperature has much less effect on the electrostatic repulsion, leading to the collapse of the gel network. The temperature independence of M_w indicates that there is no interparticle aggregation. It is necessary to indicate that we have revised the values of dn/dC that induced the temperature; dn/dC are 0.232, 0.226, and 0.212 at 25, 32, and 40 °C, respectively. It is clear that increasing pH can profoundly raise the shrinking temperature. As discussed before, for a given temperature, the swelling of the microgels as SDS increases is due to the concentration of SDS inside the gel network.

Figure 34 shows that the addition of only 0.5 mM SDS shifts the shrinking temperature to ~45 °C. When SDS is
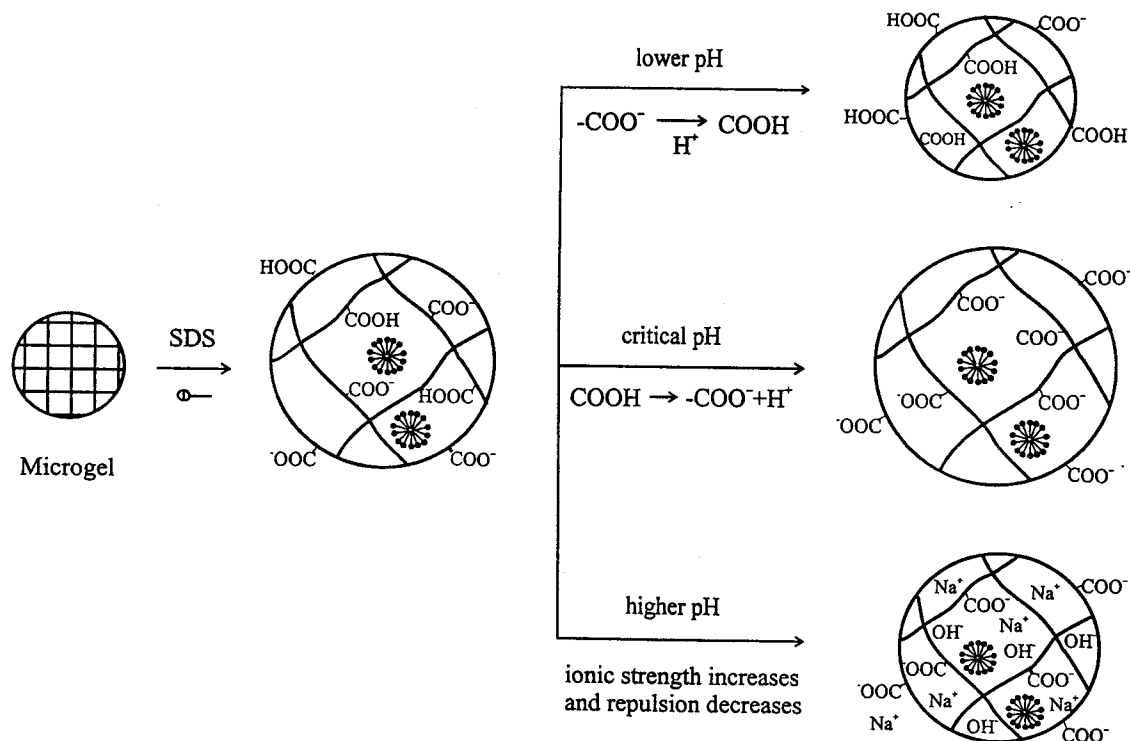
Figure 32. Schematic of the electrostatic interaction between a P(VCL-co-NaA) microgel network and anionic surfactant SDS and the effect of pH on swelling. Reprinted with permission from [167], S. Peng and C. Wu, *Macromolecules* 34, 568 (2001). © 2001, American Chemical Society.
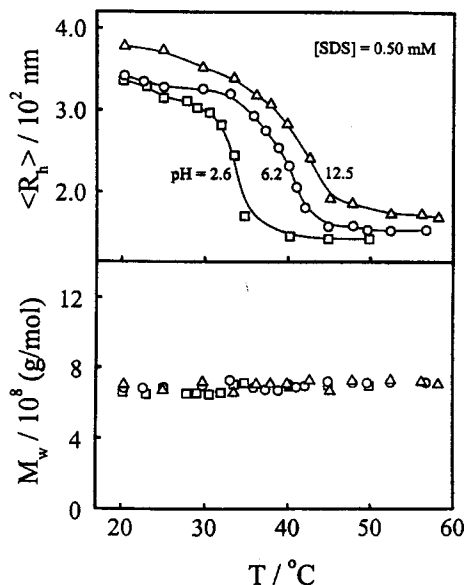
Figure 33. Temperature dependence of the average hydrodynamic radius $\langle R_h \rangle$ and weight average molar mass (M_w) of P(VCL-co-NaA) microgels in water at a given surfactant concentration, but different pH. Reprinted with permission from [167], S. Peng and C. Wu, *Macromolecules* 34, 568 (2001). © 2001, American Chemical Society.

1.0 mM, $\langle R_h \rangle$ becomes independent of the temperature, indicating that the shrinking temperature has already been shifted outside the range studied. The sharp increase of M_w reflects the aggregation of surfactant-free microgels in a high pH dispersion at ~31 °C. Note that the high ionic strength at pH 12 weakens the electrostatic repulsion. This explains why an excess amount of Na⁺ and OH⁻ led to a salt-out effect on the microgels [81, 106]. Actually, the addition of NaCl instead of NaOH had a similar effect as shown in Figure 35. It has been suggested that there exist two types of water structures—coulombic and hydrophobic—that comprise the hydration sheath of the polymer [107]. The hydrophobic hydration of P(VCL-co-NaA) is expected to exclude coulombically hydrated anionic surfactant, resulting in a more hydrophobic chain. This explains why the microgels in the presence of salt start to aggregate at higher temperatures.

In summary, our results demonstrate that the incorporation of a small amount of anionic surfactant sodium dodecyl sulfate in a spherical poly(N-vinylcaprolactam-co-sodium acrylate) microgel can greatly alter its pH and temperature sensitivities, leading to a swelling and shrinking behavior similar to those gels modified chemically with different amounts of ionic groups. We found that the surfactant-induced swelling is closely related to the concentration of anionic surfactant molecules inside the gel network, reflecting an observed relationship between the average hydrodynamic volume ($\langle V_h \rangle$) and the average number (n_s) of surfactant concentrated in
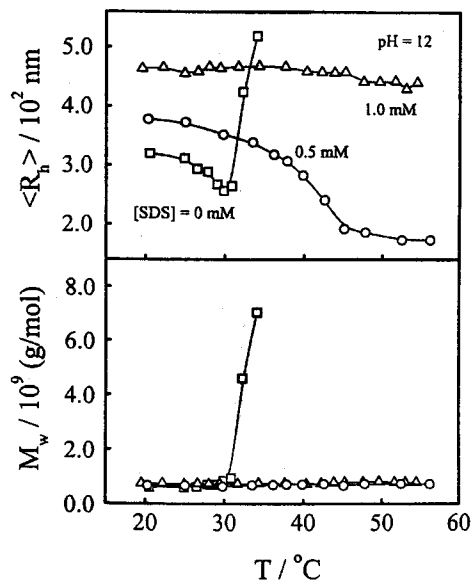
Figure 34. Temperature dependence of the average hydrodynamic radius $\langle R_h \rangle$ and weight average molar mass (M_w) of P(VCL-co-NaA) microgels in water at a given pH, but different surfactant concentrations. Reprinted with permission from [167], S. Peng and C. Wu, *Macromolecules* 34, 568 (2001). © 2001, American Chemical Society.

each microgel, namely, $\langle V_h \rangle \propto n_s^2$. We have shown that using a small amount of surfactant is much simpler and cheaper than chemical modification. The principle demonstrated in this study can be easily applied for other types of pH and thermosensitive hydrogels.
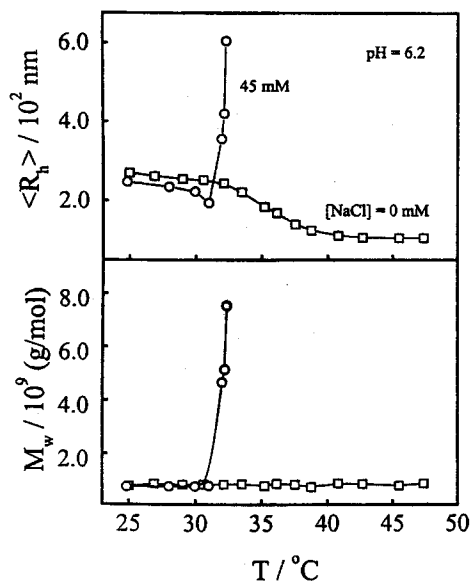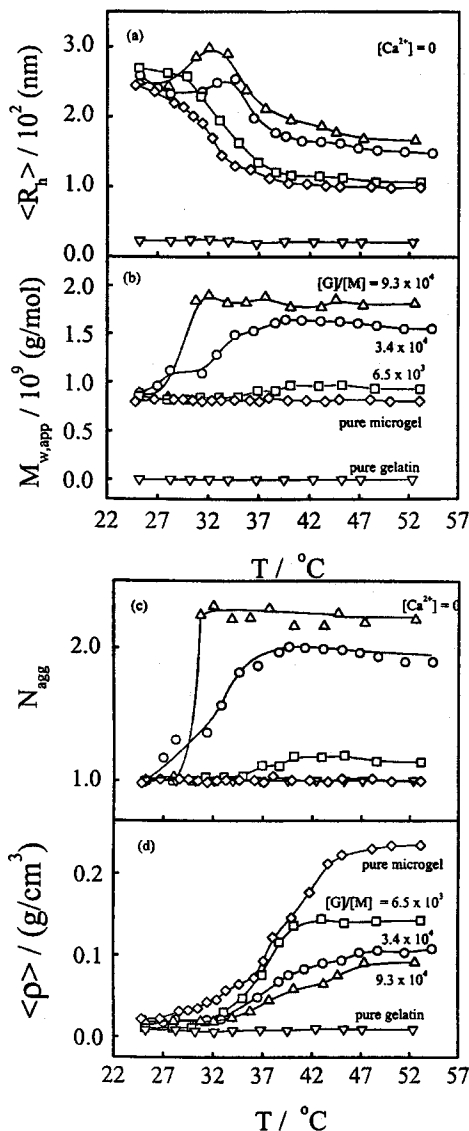

Figure 35. Temperature dependence of the average hydrodynamic radius $\langle R_h \rangle$ and weight average molar mass (M_w) of surfactant-free P(VCL-co-NaA) microgels with and without the addition of NaCl. Reprinted with permission from [167], S. Peng and C. Wu, *Macromolecules* 34, 568 (2001). © 2001, American Chemical Society.

6. COMPLEXATION BETWEEN P(VCL-*co*-NaA) MICROGELS AND GELATIN

Complexation of a polyelectrolyte and a protein can provide a range of physicochemical properties, including biocompatibility. Special attention has been drawn to their biomedical applications [24, 108]. Moreover, the complexation of synthetic polyelectrolytes and proteins presents a convenient model for various biological processes [109]. It is also known that certain metal ions as well as biphilic low molar mass compounds can bind to polyelectrolytes and lead to the complexation of polymer chains with a complementary surface [70, 110–111]. Bowman et al. [112] and Hara and Nakajima [29] studied the effects of various parameters on the structure of soluble complexes. Carboxylic groups (COO⁻) have a tendency to interact with Ca^{2+}, leading to distinct conformational changes or intermolecular bridges between polyelectrolyte chains. In biopolymers, this complexation can modify their biological activities, such as blood clotting and muscular contraction [113, 114]. In spite of a great deal of effort spent on this subject, the details of the complexation and stabilization are still missing because of its complex nature.

Figure 36 shows that when the gelatin/microgel molar ratio is less than $\sim 3.4 \times 10^4$ and Ca^{2+} is absent, both $\langle R_h \rangle$ and $M_{w, app}$ of the microgel/gelatin complexes only slightly increase at a temperature around 32 °C, revealing that, on average, each complex contains only approximately two microgels or less. A further increase of the temperature leads to a gradual decrease of $\langle R_h \rangle$, but $M_{w, app}$ is nearly independent of the temperature in the same range, indicating the shrinkage of the microgels, but no further interparticle association. For the mixture with a higher ratio $[G]/[M]$, $\langle R_h \rangle$ decreases monotonously as the temperature increases in the whole temperature range studied. The increase of the average chain density $(\langle \rho \rangle)$ of the microgel/gelatin complexes as the temperature increases in the range ~ 32–45 °C reflects shrinkage of the microgels inside the complex. Note that at high temperatures, $\langle \rho \rangle$ increases as the ratio of $[G]/[M]$ decreases, further reflecting that the shrinkage is related to the microgels. More microgels inside each complex can provide a stronger shrinking force and lead to a more compact structure at high temperatures.
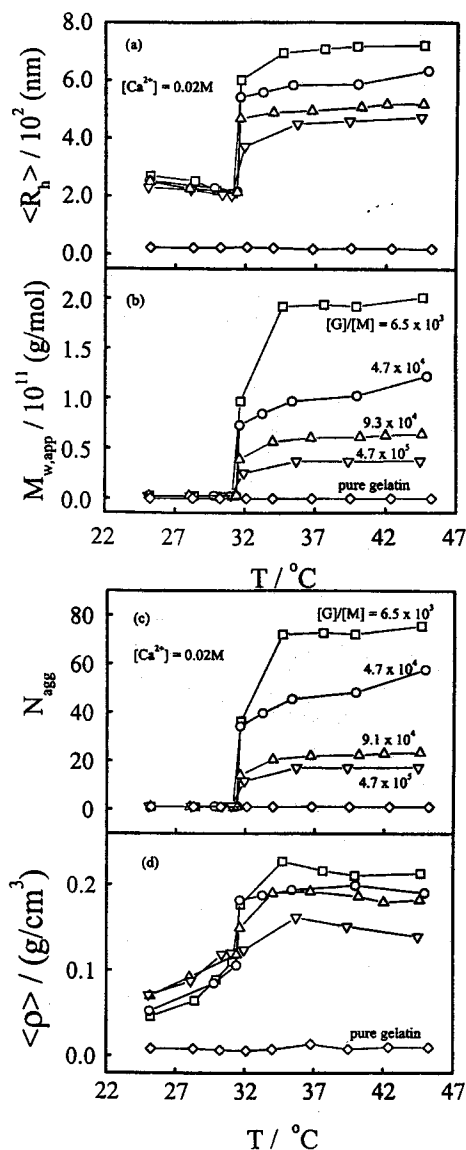
Figure 37 shows that in the presence of Ca^{2+}, the complexation is more profound in comparison with that shown in Figure 36. Both $\langle R_h \rangle$ and $M_{w, app}$ increase as the $[G]/[M]$ ratio decreases, indicating that the gelatin chains act as a stabilizer, presumably by the adsorption of gelatin chains on the microgel surface. Note that the complexation occurs at a similar temperature in spite of a big difference in the gelatin concentration. This clearly shows that when the microgel is in its shrunken state (hydrophobic), most of the carboxylic groups are forced to locate on the surface of the microgel so that Ca^{2+} can bind the microgels and gelatin chains through the carboxylic groups. On average, each complex contains 20–70 microgels and the average density of the complexes is in the range 0.13–0.22 g/cm³ at temperatures higher

Figure 36. Temperature dependence of (a) the average hydrodynamic radius $\langle R_h \rangle$, (b) the apparent weight average molar mass $(M_{w,app})$, (c) the average aggregation number (N_{agg}), and (d) the average chain density $\langle \rho \rangle$ of the microgel/gelatin complexes, where $[G]/[M]$ is the initial gelatin/microgel molar ratio and $\langle \rho \rangle$ is defined as $M_w/[(4/3)\pi\langle R_h \rangle^3]$. Reprinted with permission from [168], S. Peng and C. Wu, *Polymer* 42(17), 7355 (2001). © 2001, Elsevier Science.

Figure 37. Temperature dependence of (a) the average hydrodynamic radius $\langle R_h \rangle$, (b) the apparent weight average molar mass $(M_{w,app})$, (c) the average aggregation number (N_{agg}), and (d) the average chain density $\langle \rho \rangle$ of microgel/gelatin complexes formed in the presence of Ca^{2+}, where $[G]/[M]$ is the initial gelatin/microgel molar ratio and $\langle \rho \rangle$ is defined as $M_w/[(4/3)\pi\langle R_h \rangle^3]$. Reprinted with permission from [168], S. Peng and C. Wu, *Polymer* 42(17), 7355 (2001). © 2001, Elsevier Science.

than ~32 °C. The decreases of N_{agg} $[\equiv M_{w, aggregate}/M_{w, microgel}]$ and $\langle \rho \rangle$ $[\equiv M_{w, aggregate}/[(4/3)\pi\langle R_h \rangle^3]$ as $[G]/[M]$ increases further indicate that the adsorption of gelatin chains on the microgel surface reduces the complexation of the microgels. Figure 38 shows a schematic of the temperature dependence of the microgel/gelatin complexation in the presence of Ca^{2+}.

Figure 39 shows that in the presence of Ca^{2+}, the temperature dependence of $\langle R_h \rangle$, $M_{w,app}$, N_{agg}, and $\langle \rho \rangle$ of the complexes during heating and cooling are slightly different. Gen-

erally, there is a hysteresis during cooling. The slight increase of $\langle R_h \rangle$ during cooling before it drops at ~32 °C and a lower $\langle \rho \rangle$ reveals that the complexes swell before their dissociation at lower temperatures. This indicates that complexation of the microgels and gelatin chains formed via Ca^{2+} at high temperatures is relatively strong. When $T < ~32$ °C, the swollen microgels become so hydrophilic that the interaction between the COO^- groups and Ca^{2+} is not able to hold the microgel/gelatin complexes together. The swelling of the microgels
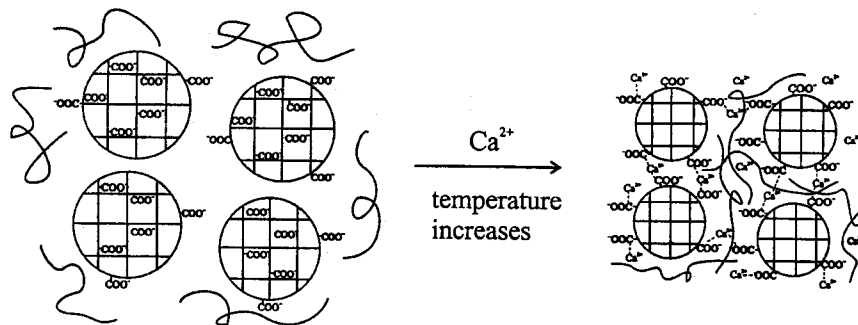
Figure 38. Schematic of the temperature dependence of microgel/gelatin complexation in the presence of Ca²⁺. Reprinted with permission from [168], S. Peng and C. Wu, *Polymer* 42(17), 7355 (2001). © 2001, Elsevier Science.

is also evidenced by the fact that at a temperature higher than ~32 °C, the complexes are larger during cooling, but there is no change in $M_{w,\,app}$. The swelling is due to the gel network's elasticity, which was absent when linear poly(N-isopropylacrylamide) or its copolymer chains were used [115, 116]. Note that for a given temperature, there is nearly no difference between N_{agg} during heating and cooling. However, N_{agg} becomes larger at 25 °C after the first heating and cooling cycle, indicating that the complexation induced at higher temperatures is not completely reversible.

Figure 40 shows a gel composite in which the microgels are embedded in a chemically cross-linked gelatin network. This clearly shows that the shrinkage of each microgel inside leads to the shrinkage of the bulk gel. The degree of shrinkage can be well controlled by the amount of microgels embedded inside and by the cross-linking density of the gelatin network. More important, both the gelatin solutions before gelation and the microgel dispersion are injectable. Gel formation inside the body makes such a gelatin/microgel composite a potential biomedical material.

Our results reveal that when the P(VCL-co-NaA) microgel becomes hydrophobic at temperatures higher than ~32 °C, most of the carboxylic groups are located on its surface so that the microgel can complex with gelatin in the presence of Ca²⁺, suggesting that the microgel/gelatin complexation is induced by both hydrophobic interaction and electrostatic attraction. However, if an excess of gelatin chains is used, the adsorption of gelatin chains on the microgel surface prevents the complexation. The shrinkage of each microgel inside can lead to the shrinkage of a bulk microgel/gelatin gel composite at temperatures higher than ~32 °C. The complexation is essentially reversible. The shrinkage of each microgel inside a gel composite leads to shrinkage of the bulk gel. This study leads to a novel and injectable thermally sensitive gel composition. It can repair broken nerve and bone tissue without any surgical stitches. Its swelling and shrinking temperature can be adjusted by the amount of carboxylic group incorporated inside the microgel, and its swelling and shrinking extent can be controlled by the microgel/gelatin ratio.

7. CONTROLLABLE AGGREGATION OF LINEAR CHAINS AND SPHERICAL MICROGELS

## 7.1. Formation and Structure of HPAM/Ca²⁺ Complexes

As a fascinating subject, the aggregation of colloidal particles in dispersion has been extensively studied because it is important in both theory and practice [117–124], such as the production of chemical toners and the treatment of wastewater. Two limiting regimes have been identified: the diffusion-limited cluster–cluster aggregation (DLCA) and the reaction-limited cluster–cluster aggregation (RLCA) [125, 126]. One of distinctive features between them is different fractal dimensions (d_f) of the resultant aggregates [127, 128], that is, different scalings between the mass (M) and size (R) of the aggregates, $M \sim R_f^d$. Which regime an actual aggregation process falls into is essentially governed by the sticking efficiency between two collided particles. In DLCA, every collision leads to irreversible sticking and the aggregation rate is limited solely by the time required for two particles to encounter each other by diffusion. The DLCA process leads to aggregates with an open and less uniform structure, and d_f in the range ~1.75–1.80 for a three-dimensional system. On the other hand, the sticking probability in RLCA is so low that a number of collisions can only result in one sticking [129–131] and individual colloidal particles can penetrate into the "fjords" of the aggregate before they stick together [132]. The resultant aggregates are more uniform with a higher fractal dimension of d_f ~2.0–2.5. Experimentally, a combination of different scattering techniques provides the possibility to study the formation and structures of colloidal aggregates over a wide size range [133–135].

The study has been extended to the association of synthetic and biopolymers, especially polyelectrolytes, in solution because of their implications in ecology, biotechnology, and medicine [136, 137]. It was found that the rate constant of the interaction increased sharply with decreasing the polycation ionic strength, but was independent of the polyanion chain length [138, 139]. It was suggested that the distribution of
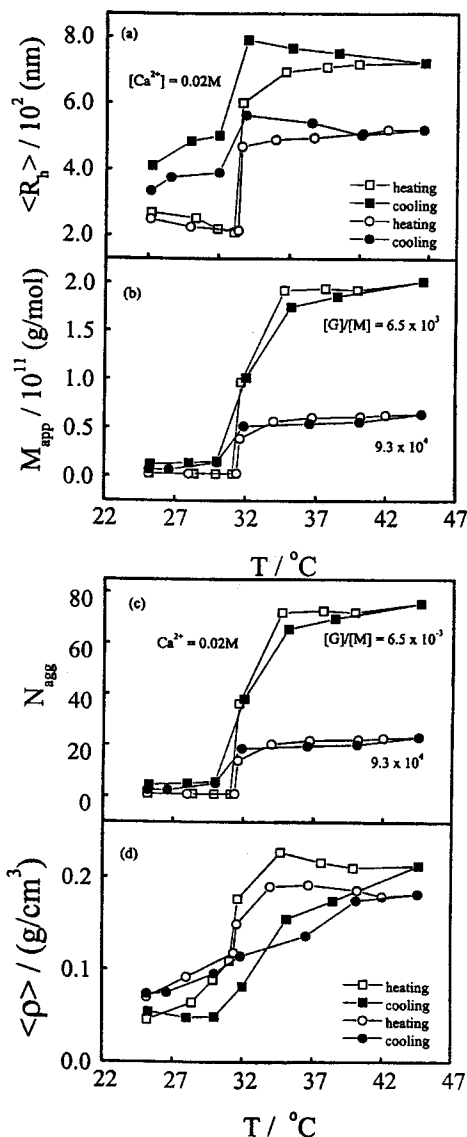
Figure 39. Heating and cooling dependence of (a) the average hydrodynamic radius $\langle R_h \rangle$, (b) the apparent weight average molar mass $(M_{w, app})$, (c) the average aggregation number (N_{agg}), and (d) the average chain density $\langle \rho \rangle$ of the microgel/gelatin complexes formed in the presence of Ca^{2+}, where $[G]/[M]$ is the initial gelatin/microgel molar ratio and $\langle \rho \rangle$ is defined as $M_w/[(4/3)\pi \langle R_h \rangle^3]$. Reprinted with permission from [168], S. Peng and C. Wu, *Polymer* 42(17), 7355 (2001). © 2001, Elsevier Science.

ionic groups on the chain backbone had no effect on the complexation [140]. In general, the association of heteropolymer chains in a dilute solution can be placed under the framework of the formation of a mesoglobule phase [141]. To our knowledge, the influence of initial chain conformation on the association of linear heteropolymers has not been thoroughly investigated and the theoretical study in this respect has been limited because linear flexible polymer chains with a variable conformation are much less defined than colloidal particles. Modeling the chain aggregation is a remaining challenge.
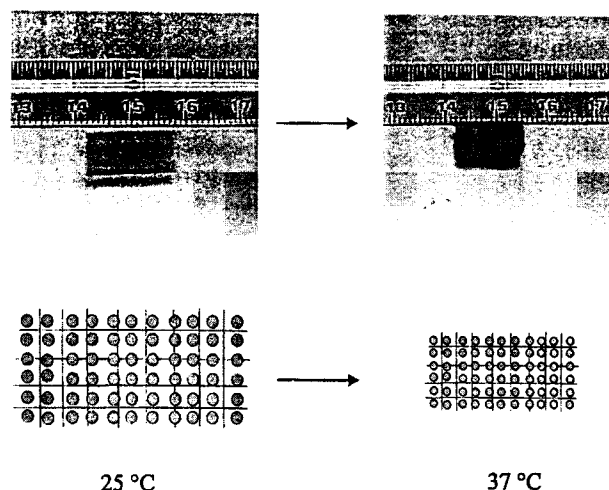

Figure 40. Swelling and shrinkage of a novel microgel/gelatin composite at two different temperatures and schematic of the corresponding structures of the composite. Reprinted with permission from [168], S. Peng and C. Wu, *Polymer* 42(17), 7355 (2001). © 2001, Elsevier Science.

7.1.1. Kinetics of Self-Complexation of Hydrolyzed Polyacrylamide Chains

It is known that certain metal ions like Ca^{2+} can specifically interact with carboxylic groups. If the carboxylic groups are attached to a polymer chain backbone as partially hydrolyzed polyacrylamide (HPAM), the interaction can lead to a chain aggregation through polyion/metal "complexation" [142]. Figure 41 shows the time dependence of the self-complexation of the HPAM chains in 0.05 M $CaCl_2$ aqueous solution in terms of the change of the hydrodynamic radius distribution $f(R_h)$. It clearly shows the increases of the size and the distribution width with time. Figure 42 shows the time dependence of the average hydrodynamic radius $\langle R_h \rangle$ of the HPAM/Ca^{2+} complexes after the addition of different amounts of Ca^{2+}, where $\langle R_h \rangle = \int f(R_h)R_h \, dR_h$. Note that for each given Ca^{2+} concentration, there exists a plateau value $\langle R_h \rangle_{max}$. Figure 43 clearly shows that for a given HPAM sample, both the initial complexation rate $[d\langle R_h \rangle / dt]_{t\rightarrow 0}$ and $\langle R_h \rangle_{max}$ increase with Ca^{2+} concentration, which is understandable because Ca^{2+} acts as the cross-linking agent to interconnect ("complex") the HPAM chains. Note that when $[Ca^{2+}] < 0.01$ M, the $\langle R_h \rangle$ is nearly independent of time, indicating that there exists a critical Ca^{2+} concentration for inter-chain complexation. Figure 43 shows that $[d\langle R_h \rangle / dt]_{t\rightarrow 0} \propto Ca^{2+}]^2$, indicating that for a given HPAM sample, the initial rate of self-complexation is strongly dependent on $[Ca^{2+}]$.

Figure 44 shows the complexation kinetics in terms of the change of $\langle R_h \rangle$ for five different HPAM samples in a given $CaCl_2$ aqueous solution. For each HPAM sample, $\langle R_h \rangle$ approaches a plateau $\langle R_h \rangle_{max}$. As expected, $\langle R_h \rangle_{max}$ decreases as the hydrolysis degree decreases. It is interesting to note that in Figure 44, there exists an initial stage in which $\langle R_h \rangle$ decreases, which reveals an intrachain complexation in which
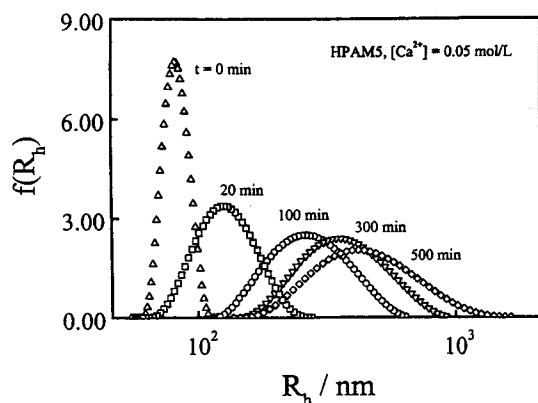
Figure 41. Time dependence of the hydrodynamic radius distribution $f(R_h)$ of HPAM/Ca^{2+} complexes for self-complexation of the HPAM chains in 0.05 M CaCl$_2$ aqueous solut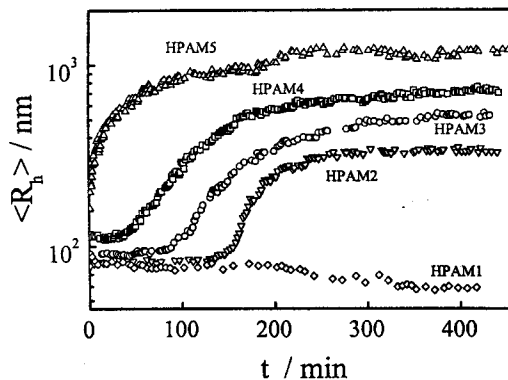ion. Reprinted with permission from [169], S. Peng and C. Wu, *Macromolecules* 32, 585 (1999). © 1999, American Chemical Society.
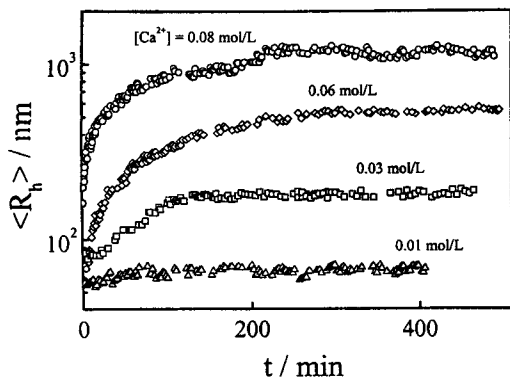
Figure 42. Time dependence of the average hydrodynamic radius $\langle R_h \rangle$ of HPAM/Ca^{2+} complexes for self-complexation of the HPAM chains in different CaCl$_2$ aqueous solutions. Reprinted with permission from [169], S. Peng and C. Wu, *Macromolecules* 32, 585 (1999). © 1999, American Chemical Society.
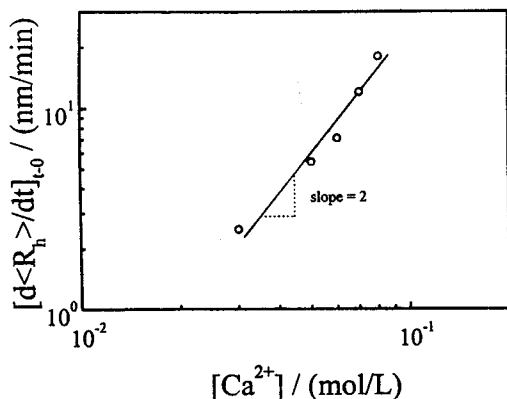
Figure 43. Ca^{2+} concentration dependence of the initial complexation rate $[d\langle R_h \rangle/dt]_{t \to 0}$ calculated from the data in Figure 42, where the slope of the line is 2. Reprinted with permission from [169], S. Peng and C. Wu, *Macromolecules* 32, 585 (1999). © 1999, American Chemical Society.
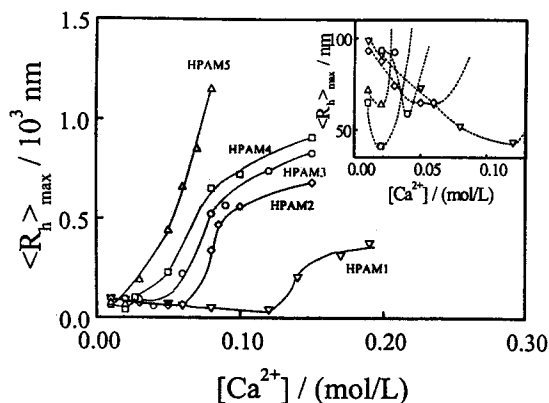

Figure 44. Time dependence of the average hydrodynamic radius $\langle R_h \rangle$ of the HPAM/Ca^{2+} complexes for self-complexation of HPAM samples in 0.08 M CaCl$_2$ aqueous solution. Reprinted with permission from [169], S. Peng and C. Wu, *Macromolecules* 32, 585 (1999). © 1999, American Chemical Society.

individual HPAM chains contract before the interchain aggregation. For HPAM5, the *interchain* complexation was dominant and the initial stage was too short to be observed, whereas for HPAM1, the *intrachain* complexation was dominant, so that no increase of $\langle R_h \rangle$ was observed. As for HPAM2, HPAM3, and HPAM4, the transition from the *intrachain* complexation to *interchain* complexation is very clear. To our knowledge, this transition is observed and reported for the first time. Figure 44 reveals that for a given Ca^{2+} concentration, the *interchain* complexation is directly related to the hydrolysis degree because the carboxylic groups act as "stickers" to complex with the HPAM chains, similar to the results of the PMA/Ca^{2+} system reported by Yuko et al. [143].

Figure 45 shows the Ca^{2+} concentration dependence of $\langle R_h \rangle_{max}$ for five different HPAM samples. The inset shows an enlargement of the low [Ca^{2+}] range in which $\langle R_h \rangle_{max}$ decreases as [Ca^{2+}] increases, indicating the *intrachain* complexation. Figure 45 shows that at higher [Ca^{2+}] concentrations, $\langle R_h \rangle$ increases sharply as [Ca^{2+}] increases, revealing a Ca^{2+}-induced transition between the *intrachain* and *interchain* complexations. The [Ca^{2+}] concentration at which $\langle R_g \rangle$ starts to increases is defined as the aggregation concentration [Ca^{2+}]$_{agg}$.

Figure 46 shows the hydrolysis degree (HD%) dependence of [Ca^{2+}]$_{agg}$, where the inset shows a double logarithmic plot of [Ca^{2+}]$_{agg}$ versus [—COO$^-$]. The line in the inset shows a least square fitting of [Ca^{2+}]$_{agg}$ = 7.46 × 10^{-9} [—COO$^-$]$^{-1.4}$. Figures 43 and 45 clearly reveal that increasing either the hydrolysis degree or [Ca^{2+}] can promote the *interchain* complexation. Figure 46 shows that increasing the hydrolysis degree is more effective, but there is an upper limit of ~20% beyond which the increases of HD% have less effect on the *interchain* complexation. The ratio of [—COO$^-$]/[Ca^{2+}] should be 2 if every Ca^{2+} ion in the solution complexes with two —COO$^-$ ions. However, as shown in Figure 46, [—COO$^-$]/[Ca^{2+}] is much smaller than 2, indicating that most of the Ca^{2+} ions are free in water.

Figure 45. Ca^{2+} concentration dependence of the maximum average hydrodynamic radius $\langle R_h \rangle_{max}$, where $\langle R_h \rangle_{max}$ is the plateau value as shown in Figure 44. Reprinted with permission from [169], S. Peng and C. Wu, *Macromolecules* 32, 585 (1999). © 1999, American Chemical Society.

Figure 47. pH dependence of the maximum average hydrodynamic radius $\langle R_h \rangle_{max}$ for a given ratio of $[Ca^{2+}]/[-COO^-]$. Reprinted with permission from [169], S. Peng and C. Wu, *Macromolecules* 32, 585 (1999). © 1999, American Chemical Society.

Figure 47 shows the pH dependence of $\langle R_h \rangle_{max}$ for a given $[Ca^{2+}]$ concentration. Note that $K_{acid} \equiv [-COO^-][H^+]/[COOH]$ and $pH \equiv -\log[H^+]$, that is, $\log[-COO^-]/[COOH] = \log(K_{acid}) + pH$, where K_{acid} is a constant. Therefore, $[-COO^-]/[COOH]$ increases as pH increases. In other words, the effective hydrolysis degree (or the sticking probability when two HPAM chains collide) increases with pH. This is why $\langle R_h \rangle_{max}$ of the HPAM/Ca^{2+} complexes increases with pH. When $pH < 3$, $\langle R_h \rangle_{max}$ is independent of pH, which can be attributed to the shift of $-COO^-$ to $-COOH$, so that further complexation of the HPAM chains stops.

From Figures 42–47, we know that complexation between the HPAM chains in $CaCl_2$ aqueous solutions can be dominated by either *intrachain* or *interchain* complexation, depending on the hydrolysis degree and Ca^{2+} concentration. The

complexation can be viewed as follows: Each HPAM is a long coil chain with hundreds of stickers ($-COO^-$). Two stickers and one Ca^{2+} ion can be driven thermodynamically together to form one $(-COO)_2Ca$ complex point. The *interchain* "points" result in the clustering of the HPAM chains. These clusters further collide with each other or with individual HPAM chains, leading to larger clusters. Finally, when either Ca^{2+} ions or $-COO^-$ groups are consumed, the complexation stops. In the process, clusters with different sizes were formed as shown in Figure 34. Note that the *intrachain* $-COO^-$ groups are closer than the *interchain* $-COO^-$ groups. For the HPAM chains with a low degree of hydrolysis, the *intrachain* complexation in the presence of small amounts of Ca^{2+} ions is expected to be easier. In the case of a high hydrolysis degree and a high Ca^{2+} concentration, the *interchain* complexation dominates, as shown schematically in Figure 48. In the medium range of $[Ca^{2+}]$ and $[-COO^-]$, the HPAM chains first undergo *intrachain* complexation through the neighboring carboxylic acid groups on the same chain before the *interchain* complexation becomes apparent.

7.1.2. Fractal Structure of HPAM/Ca^{2+} Complexes

Figure 49 shows double logarithmic plots of the weight average molar mass (M_w) of the HPAM/Ca^{2+} complexes versus their average hydrodynamic radius $\langle R_h \rangle$ for a given HPAM sample and different Ca^{2+} concentrations. Figure 50 shows double logarithmic plots of M_w versus $\langle R_h \rangle$ for a given Ca^{2+} concentration and different HPAM samples. The values of M_w were calculated from the measured Rayleigh ratio on the basis of

Figure 46. Hydrolysis degree (HD%) dependence of the aggregation concentration ($[Ca^{2+}]_{agg}$), where $[Ca^{2+}]_{agg}$ is defined as the Ca^{2+} concentration at wh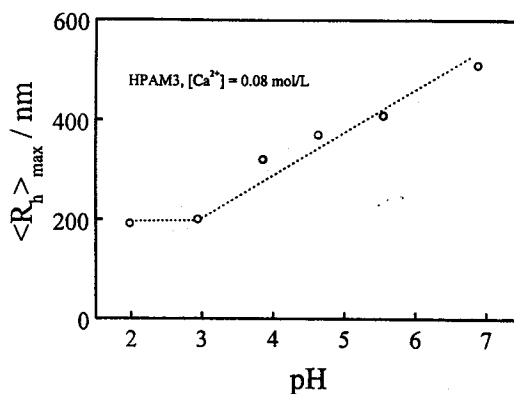ich $\langle R_h \rangle$ starts to increase as shown in Figure 45. The inset shows a double logarithmic plot of $[Ca^{2+}]_{agg}$ versus $[-COO^-]$ and the straight line represents a least square fit of $[Ca^{2+}]_{agg} = 7.46 \times 10^{-9} [-COO^-]^{-1.4}$. Reprinted with permission from [169], S. Peng and C. Wu, *Macromolecules* 32, 585 (1999). © 1999, American Chemical Society.

$$\frac{KC}{R_{vv}(q)} \cong \frac{1}{M_w}\left(1 + \frac{1}{3}\langle R_g^2 \rangle_z q^2\right) + 2A_2C \tag{1}$$
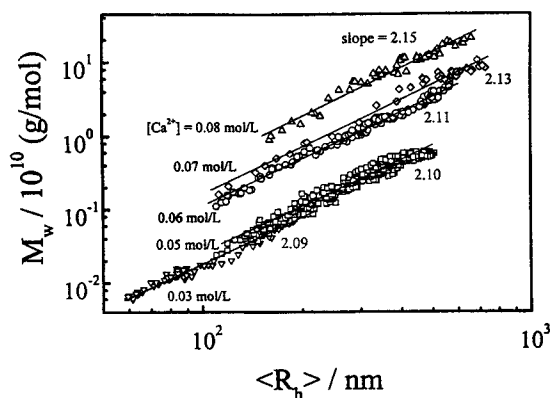
where $K [=(4\pi^2 n_1^2/\lambda_0^4 N_A)(dn/dC)^2]$ is a constant and $q [=(4\pi n_1/\lambda_0)\sin(\theta/2)]$ is the scattering vector where N_A is Avogadro's number, dn/dC is the specific refractive index increment, n_1 is the refractive index of the solvent, λ_0 is
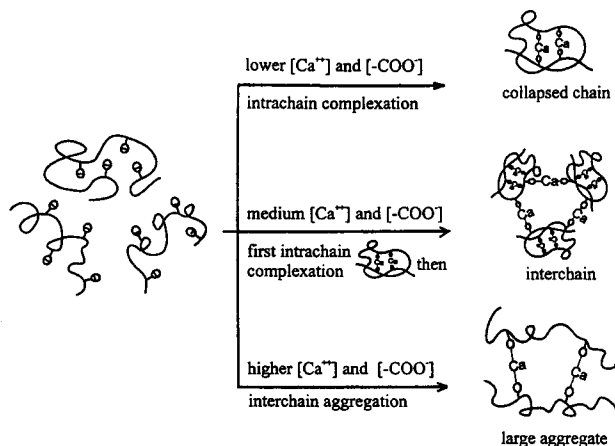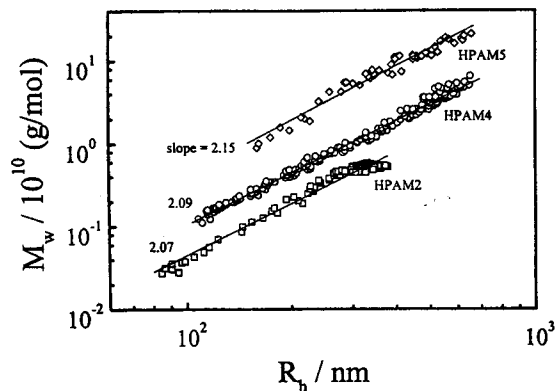
Figure 48. Schematic of the self-complexation of the HPAM chains under different experimental conditions. Reprinted with permission from [169], S. Peng and C. Wu, *Macromolecules* 32, 585 (1999). © 1999, American Chemical Society.

Figure 50. Double logarithmic plots of the weight average molar mass (M_w) versus the hydrodynamic radius $\langle R_h \rangle$ for different HPAM samples in 0.08 M $CaCl_2$ aqueous solution. Reprinted with permission from [169], S. Peng and C. Wu, *Macromolecules* 32, 585 (1999). © 1999, American Chemical Society.

the wavelength of the light in vacuum, and θ is the scattering angle, respectively. It should be stated that the ratio of $\langle R_g \rangle / \langle R_h \rangle$ was close to a constant of ~ 1.35 in the measurable range of $\langle R_g \rangle$. Figures 50 and 51 clearly demonstrate that M_w can be scaled to $\langle R_h \rangle$ (i.e., $M_w \propto \langle R \rangle^{2.11 \pm 0.04}$) for different Ca^{2+} concentrations and different HPAM samples. This suggests that the HPAM/Ca^{2+} complexes have a fractal structure with a dimension of $d_f = 2.11 \pm 0.04$, which is in a good agreement with the value predicted for RLCA [144, 145].

Figure 51 shows double logarithmic plots of the scattering intensity $I(q)$ versus the scattering vector q after the maximum complexation was reached. The slope of ~ 2 also indicates that the HPAM/Ca^{2+} complexes have a fractal structure.

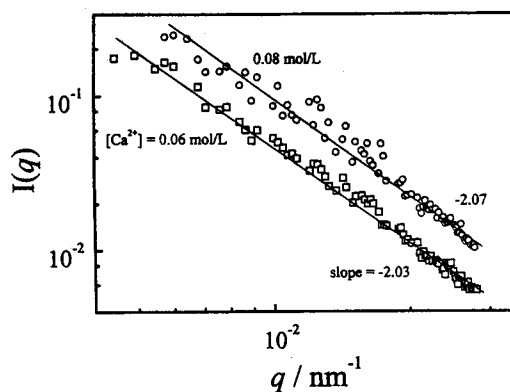## 7.2. Comparison Between P(VCL-*co*-NaA) Microgels and Linear Chains

In addition, by using thermally sensitive poly(*N*-vinylcaprolactam-*co*-sodium acrylate) (P(VCL-*co*-NaA)) chains, we were able to keep the same chain length and ionic distribution, and alter only the initial chain conformation by a simple temperature variation because PVCL is hydrophilic/soluble in water and has a coil conformation at ~ 25 °C or below. P(VCL-*co*-NaA) gradually becomes hydrophobic/insoluble and collapses into a globule when the temperature increases from ~ 25 to ~ 35 °C [136]. Taking advantage of this thermal sensitivity, we studied the influence of the initial chain conformation on the Ca^{2+}/COO^- complexation-induced aggregation. Figure 52 shows that the Ca^{2+}/COO^- complexation can induce an interparticle aggregation after the dispersion temperature suddenly is increased from 30 to 32.5 °C. As expected, the extent of

Figure 49. Double logarithmic plots of the weight average molar mass (M_w) versus the average hydrodynamic radius $\langle R_h \rangle$ for the HPAM5 chains in the presence of different amounts of Ca^{2+} ions. Reprinted with permission from [169], S. Peng and C. Wu, *Macromolecules* 32, 585 (1999). © 1999, American Chemical Society.

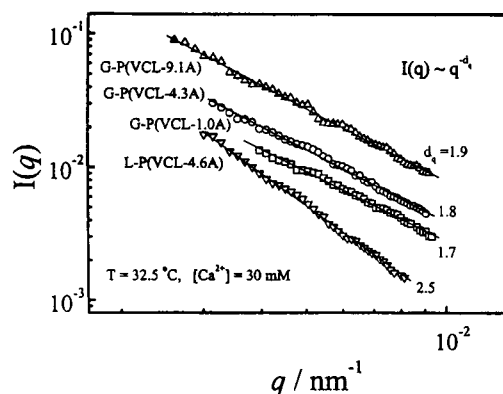**Figure 51.** Double logarithmic plots of the scattering intensity $I(q)$ versus the scattering vector q for the HPAM5 chains in two different $CaCl_2$ aqueous solutions after maximum complexation was reached. Reprinted with permission from [169], S. Peng and C. Wu, *Macromolecules* 32, 585 (1999). © 1999, American Chemical Society.

the aggregation for a given Ca^{2+} concentration increases with the ionic content because each COO^- group acts as a sticker in the interparticle or interchain aggregation via the $Ca^{2+}(COO^-)_2$ complexation. The aggregation slows down after a few hours and gradually approaches a plateau. The resultant aggregates were very stable and no precipitation was observed for a long time. For spherical microgels, $\langle R_h \rangle$ can be scaled to t by $\langle R_h \rangle \propto t^\beta$ with β in the range 0.16–0.20, but the aggregation of linear chains has a different kinetics; namely, the increase of $\langle R_h \rangle$ can be described by two exponential terms that represent two distinct processes. The initial fast process is related to the aggregation of individual chains and the formation of clusters, whereas the second slow process mainly involves cluster–cluster aggregation.

Figure 53 shows that the scattering intensity $I(q)$ of the resultant aggregates is dependent on the scattering vector q as $I(q) \propto q^{-d_q}$ with $d_q = 1.7$–1.9 for spherical microgels and $d_q = 2.4$–2.5 for linear chains, indicating that the aggregation of spherical microgels follows the DLCA process, but the aggregation of linear chains might be described by the RLCA mechanism. For spherical microgels, the slight decrease of d_q as the COO^- content increases indicates that the structure of the aggregates made of microgels with less COO^- groups is relatively more open and less uniform. Note that d_q for linear P(VCL-co-NaA) chains is higher than ~2.0–2.2 observed in the aggregation/association of other linear chains, such as in the HPAM/Ca^{2+} system [129]. This is because, in addition to the interpenetration of different chains, the collapse of PVCL at higher temperatures leads to a more uniform structure. The packing of spherical microgels or linear chains in the resultant aggregates can be better viewed in terms of the size dependence of the average chain density $\langle \rho \rangle$ defined as $M_w/[(4/3)\pi\langle R_h \rangle^3]$.

Figure 54 shows that during the aggregation, $\langle \rho \rangle$ decreases as the aggregation proceeds, clearly indicating that the aggregates become loose and less uniform. Unfortunately, $\langle \rho \rangle$ and

Figure 53. Double logarithmic plots of the scattering intensity $I(q)$ versus the scattering vector q for resultant aggregates made of different spherical microgels and linear chains, where $[Ca^{2+}] = 30$ mM and $T = 32.5$ °C. Reprinted with permission from [170], S. Peng and C. Wu, *Macromolecules* 34, 6795 (2001). © 2001, American Chemical Society.

$\langle R_h \rangle$ only spread over a limited range. A combination of Figures 53 and 54 shows that for a given size, the aggregates made of microgels have a lower d_q and chain density. It also shows that the aggregates made of linear chains have a much lower chain density but a higher d_q. This is because, in comparison with the microgels, there is no chemical cross-linking among different chains in the aggregates made of linear chains. Therefore, the interchain distance inside is large, so the chain density is lower. Thermodynamically, there should be an entropy penalty when individual microgels stick together, but the intertwining and knotting of linear chains could lead to a possible entropy gain. It is expected that the enthalpy change in the formation of each $Ca^{2+}(COO^-)_2$ complex is a constant. Therefore, the increase of entropy makes a process more favorable. Figure 55 shows a schematic of the Ca^{2+}/COO^- complexation-induced aggregation of spherical microgels and linear chains at higher temperatures. The difference in the lin-
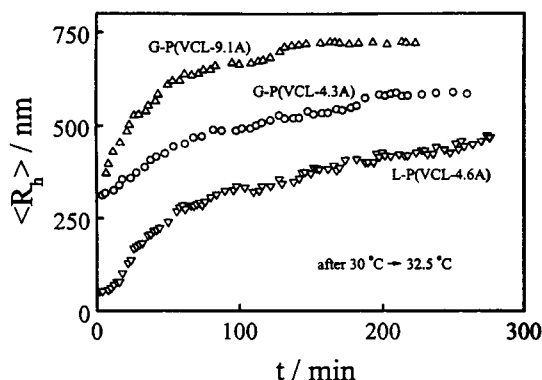
Figure 52. Time dependence of the average hydrodynamic radius $\langle R_h \rangle$ of aggregates, made of different spherical microgels and linear chains, where $[Ca^{2+}] = 30$ mM and $T = 32.5$ °C. Reprinted with permission from [170], S. Peng and C. Wu, *Macromolecules* 34, 6795 (2001). © 2001, American Chemical Society.
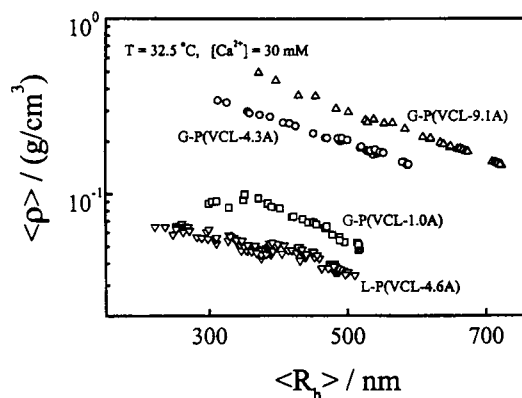
Figure 54. Aggregate size dependence of the average chain density $\langle \rho \rangle$ for different spherical microgels and linear chains, where $[Ca^{2+}] = 30$ mM and $T = 32.5$ °C. Reprinted with permission from [170], S. Peng and C. Wu, *Macromolecules* 34, 6795 (2001). © 2001, American Chemical Society.
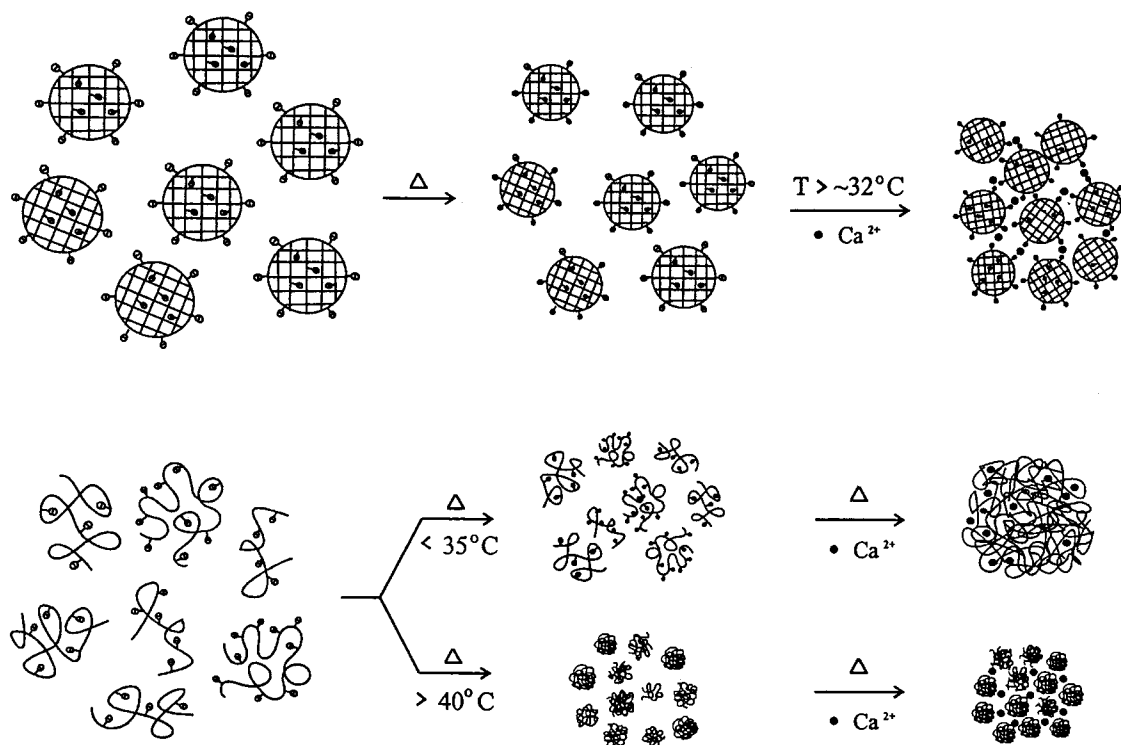
Figure 55. Schematic of Ca^{2+}/COO^- complexation-induced aggregation of thermally sensitive P(VCL-*co*-NaA) spherical microgels and linear chains at high temperatures. Reprinted with permission from [170], S. Peng and C. Wu, *Macromolecules* 34, 6795 (2001). © 2001, American Chemical Society.

ear chain aggregation at different temperatures is presented and discussed as follows.

Figure 56 shows that for a given Ca^{2+} concentration, $\langle R_h \rangle$ decreases as the aggregation temperature increases. This is different from what we expected. Originally, we thought that PVCL at a higher temperature was more hydrophobic, so aggregation should be enhanced. However, we forgot that PVCL collapses more at a higher aggregation temperature. After a sudden temperature increase, individual microgels collapse before they have a chance to be stuck together by Ca^{2+}. The higher the temperature, the faster the collapse. It is expected that in a fast shrinking process, more COO^- groups are trapped inside, so that the number of effective COO^- groups on the periphery decreases. Therefore, the binding probability between two collided microgels reduces. Furthermore, we should consider the surface curvature of collapsed microgels. For less collapsed microgels, the surface is relatively flat so that two microgels can be stuck together via more $Ca^{2+}(COO^-)_2$ complexation points, resulting in a stronger binding. For fully collapsed microgels, the surface curvature limits the complexation between two microgels. Figure 57 shows that $I(q)$ is scaled to q as $I(q) \propto q^{-d_q}$ with d_q in the range 1.6–1.8. The slight decrease of d_q as the temperature increases reveals that the aggregates formed at higher temperatures are relatively more open and less uniform.

In comparison, Figure 58 shows the aggregation of linear chains at different temperatures. As in the case of microgels,

the resultant aggregates become smaller when the temperature is higher. At 35 °C, there exists a short initial induction period in which there is no apparent interchain aggregation. Figure 59 shows a corresponding scaling between $I(q)$ and q for the resultant aggregates made of linear chains. d_q decreases as the aggregation temperatures increase. At 45 and 50 °C, d_f is similar to those values observed in the aggregation of spherical microgels. Note that the complexation of linear chains could
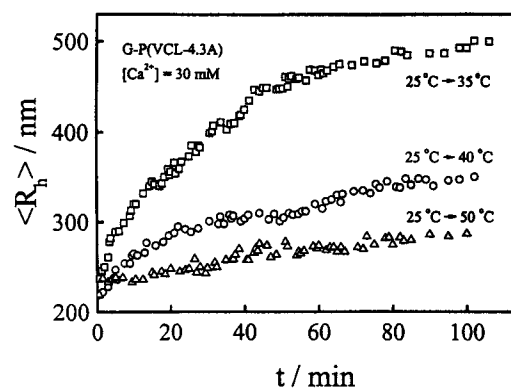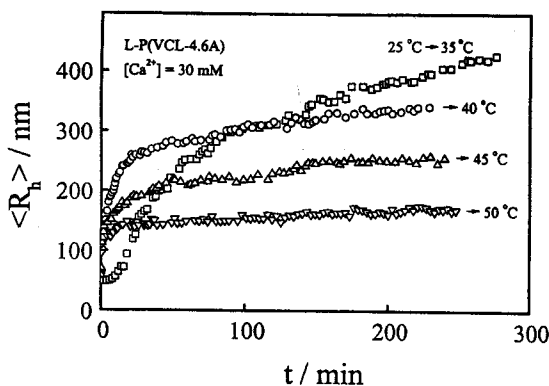

Figure 56. Time dependence of the average hydrodynamic radius $\langle R_h \rangle$ of microgel aggregates formed after the dispersion temperatures were suddenly increased to different aggregation temperatures. Reprinted with permission from [170], S. Peng and C. Wu, *Macromolecules* 34, 6795 (2001). © 2001, American Chemical Society.
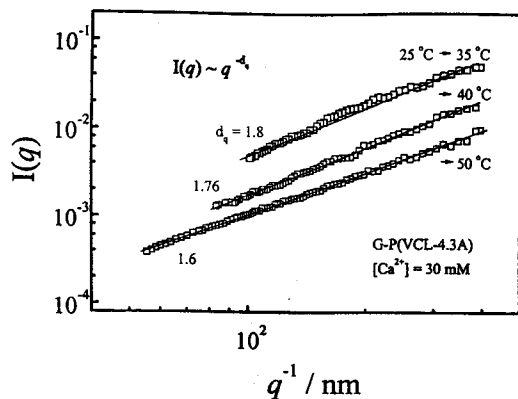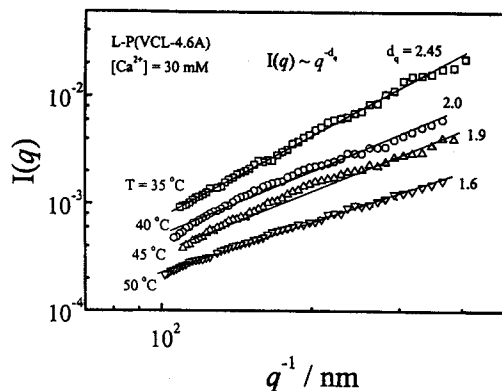
Figure 57. Double logarithmic plots of the scattering intensity $I(q)$ versus the scattering vector q for resultant microgel aggregates formed at different aggregation temperatures. Reprinted with permission from [170], S. Peng and C. Wu, *Macromolecules* 34, 6795 (2001). © 2001, American Chemical Society.

Figure 59. Double logarithmic plots of scattering intensity $I(q)$ versus scattering vector q for resultant linear chain aggregates formed at different aggregation temperatures. Reprinted with permission from [170], S. Peng and C. Wu, *Macromolecules* 34, 6795 (2001). © 2001, American Chemical Society.

be either intrachain or interchain. The intrachain complexation leads to chain contraction; only the interchain complexation results in aggregation. The two processes always compete in a real experiment. At a lower aggregation temperature, individual crumpled chains are able to interpenetrate to form a more uniform structure. As the aggregation temperature increases, the collapse of individual chains becomes so fast that individual chains have less chance to undergo interchain complexation in a dilute solution. Therefore, the complexation at higher temperatures mainly happens between highly collapsed small clusters, similar to the complexation between the collapsed microgels. Therefore, less interchain penetration occurs at higher temperatures, as illustrated in Figure 55.

Figure 60 reveals that in spite of different values of d_f shown in Figure 59, the plots of $\langle \rho \rangle$ versus $\langle R_h \rangle$ for different temperatures collapse together. It is clear that in the initial stage, small linear chain aggregates formed at 35 °C have a

lower chain density. This is because linear chains were not fully collapsed at 35 °C and the interpenetration of different chains at the initial stage was less. At higher temperatures, linear chains are more collapsed so that as the aggregation temperature increases, the chain density increases, but the size of the aggregates decreases, supporting the results in Figure 58, namely, a higher aggregation temperature leads to aggregates with a more open and less uniform structure.

Figure 61 shows that for the aggregation of microgels at 35 °C , the aggregation rate and the size and molar mass of the resultant aggregates increases with increasing Ca^{2+} concentrations. This is because more Ca^{2+} ions can enhance the sticking probability of two collided microgels via Ca^{2+}/COO^- complexation. However, a similar scaling of $I(q)$ versus q shown in Figure 62 reveals that the structure of the resultant aggregates is independent of Ca^{2+} concentration. The aggregation at 35 °C leads to a structure with d_q in the range 1.7–1.9, which agrees well with the DLCA model. Figure 63
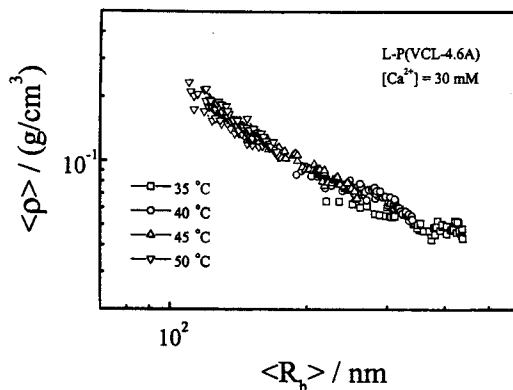

Figure 58. Time dependence of the average hydrodynamic radius $\langle R_h \rangle$ of linear chain aggregates formed after the solution temperatures were suddenly increased to different aggregation temperatures. Reprinted with permission from [170], S. Peng and C. Wu, *Macromolecules* 34, 6795 (2001). © 2001, American Chemical Society.

Figure 60. Double logarithmic plots of the aggregate size dependence of the average chain density $\langle \rho \rangle$ versus the average hydrodynamic radius $\langle R_h \rangle$ for resultant linear chain aggregates formed at different aggregation temperatures. Reprinted with permission from [170], S. Peng and C. Wu, *Macromolecules* 34, 6795 (2001). © 2001, American Chemical Society.
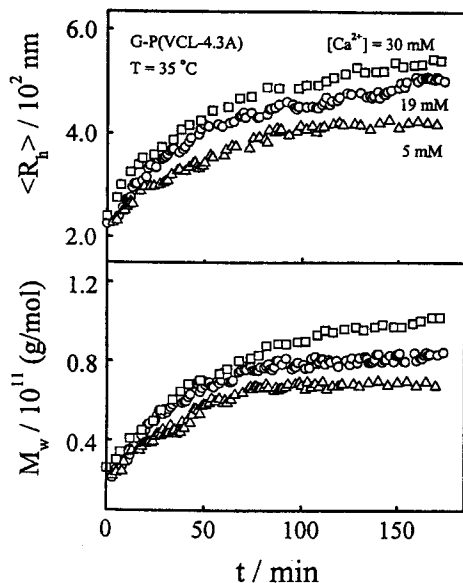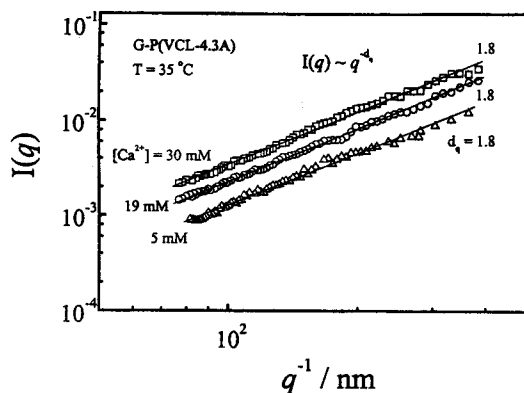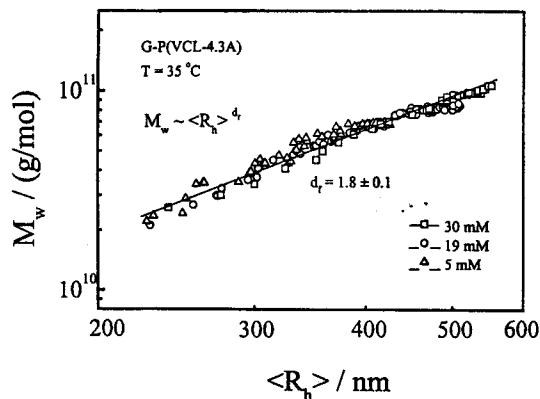
Figure 61. Temperature dependence of the average hydrodynamic radius $\langle R_h \rangle$ and the weight average molar mass M_w of microgel aggregates formed in the presence of different amounts of Ca^{2+}. Reprinted with permission from [170], S. Peng and C. Wu, *Macromolecules* 34, 6795 (2001). © 2001, American Chemical Society.

shows that the plots of M_w versus $\langle R_h \rangle$ in the presence of three different amounts of Ca^{2+} ions collapse into a single line of $M_w \propto \langle R_h \rangle^{d_f}$ with $d_f = 1.8 \pm 0.1$, further indicating that the Ca^{2+} concentration has no influence on the structure of the resultant aggregates. A combination of Figures 61–63 show that in spite of different aggregation rates and aggregate sizes, the aggregation mechanism and the aggregate structure are not influenced by the cation concentration as long as the ratio of $[Ca^{2+}]/[COO^-]$ is much higher than the stoichiomeric ratio (1:2).


Figure 62. Double logarithmic plots of the scattering intensity $I(q)$ versus the scattering vector q for resultant microgel aggregates formed in the presence of different amounts of Ca^{2+}. Reprinted with permission from [170], S. Peng and C. Wu, *Macromolecules* 34, 6795 (2001). © 2001, American Chemical Society.

Figure 63. Double logarithmic plots of the weight average molar mass M_w versus the average hydrodynamic radius $\langle R_h \rangle$ of resultant microgel aggregates formed in the presence of different amounts of Ca^{2+}. Reprinted with permission from [170], S. Peng and C. Wu, *Macromolecules* 34, 6795 (2001). © 2001, American Chemical Society.

In comparison, Figure 64 shows that for linear chains, both the complexation rate and the aggregate size also increase with Ca^{2+} concentration. Note that when $[Ca^{2+}] = 5$ mM, there is no apparent interchain complexation even though the ratio of $[Ca^{2+}]/[COO^-]$ is already hundreds times higher than the stoichiometric ratio (1:2). In comparison with the aggregation of spherical microgels under the same condition, the Ca^{2+}/COO^- complexation-induced aggregation of linear chains is less effective. Note that at 35 °C, each linear chain is not fully collapsed and the COO^- groups are uniformly distributed in its hydrodynamic volume, whereas the shrinkage of microgels forces more COO^- groups on to the surface. Thus, it is easier for two collided microgels to stick together. Figure 65 shows that the scaling of $I(q)$ to q is similar, revealing that the structure of the aggregates is also not affected by the Ca^{2+} concentration. The higher fractal dimension d_q of the linear chain aggregates was discussed before.

We have shown that the Ca^{2+}/COO^- complexation-induced aggregation of thermally sensitive poly(N-vinylcaprolactam-co-sodium acrylate) spherical microgels is essentially governed by the DLCA mechanism, leading to aggregates with a fractal dimension d_f in the range 1.7–1.9. The chain density of the resultant aggregates increases with the sodium acrylate content. The increase of Ca^{2+} concentration can speed up the aggregation and result in larger aggregates, but has no influence on the aggregation mechanism and the aggregate structure. We also found that the fractal dimension and the chain density of the resultant aggregates slightly decreased as the aggregation temperature increased. As for poly(N-vinylcaprolactam-co-sodium acrylate) linear chains, the situation is more complicated because the chain conformation varies with the aggregation temperature. We have revealed *for the first time* that the fractal dimension of linear chain aggregates is dependent on the initial chain conformation. At a relatively lower aggregation temperature, the contraction of individual chains was accompanied by an extensive interchain
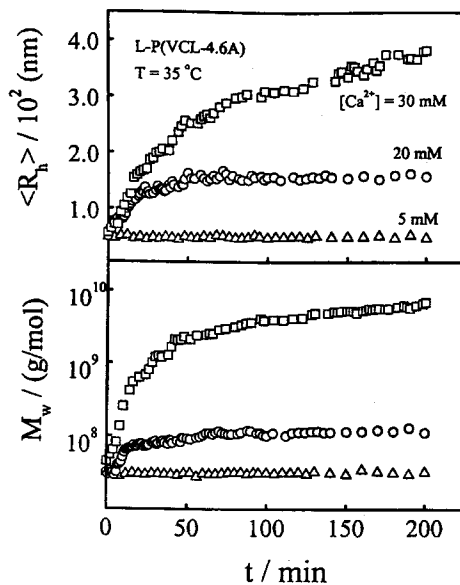
Figure 64. Time dependence of the average hydrodynamic radius $\langle R_h \rangle$ and the weight average molar mass M_w for resultant linear chain aggregates formed in the presence of different amounts of Ca^{2+}. Reprinted with permission from [170], S. Peng and C. Wu, *Macromolecules* **34**, 6795 (2001). © 2001, American Chemical Society.

penetration and aggregation. The resultant aggregates are more uniform. As the aggregation temperature increases, the collapse of individual chains is so fast that they have less chance to undergo interchain aggregation. Therefore, Ca^{2+}/COO^- complexation mainly happens between highly collapsed small clusters, resulting in a more open and less uniform structure, similar to that formed in the aggregation of spherical microgels. The fractal dimension of the resultant linear chain aggregates decreases from 2.5 to 1.6 as the aggregation temperature increases from 35 to 50 °C.
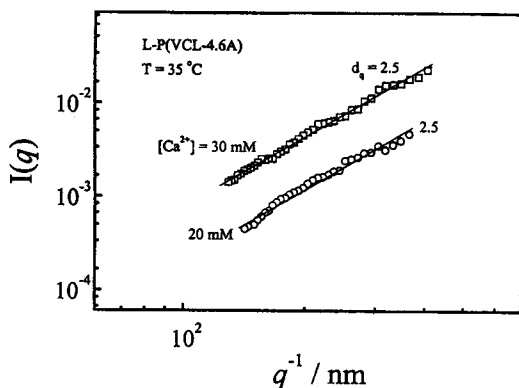
Figure 65. Double logarithmic plots of scattering intensity $I(q)$ versus scattering vector q for resultant linear chain aggregates in the presence of different amounts of Ca^{2+}. Reprinted with permission from [170], S. Peng and C. Wu, *Macromolecules* **34**, 6795 (2001). © 2001, American Chemical Society.

8. FORMATION AND STABILIZATION OF HYDROPHILIC MODIFIED POLYSTYRENE

Ionomers usually refer to macromolecules that contain no more than 10 mol% ionic groups chemically bound to a hydrophobic chain backbone. Ionomers can be homopolymers partially substituted with ionic groups or random copolymers made of neutral and ionic monomers. It has been found that ionomers (i.e., polymer chains with only a few mole percent ionic groups attached to the chain backbone) can form narrowly distributed nanoparticles that are stable in water if a special microphase inversion method is used [146–148]. Microphase inversion is a redispersion process; namely, ionomer is dissolved in a water-miscible solvent, such as acetone or tetrahydrofuran (THF), and then the ionomer solution is added dropwise to an excess of water. As expected, the solvent immediately mixes with water and the insoluble hydrophobic chains undergo an intrachain contraction and interchain association, while the ionic groups are forced to stay on the periphery during the microphase inversion. It is this small amount of ionic groups that stabilize the resultant nanoparticles. Using this method, we were able to make surfactant-free polystyrene nanoparticles as small as a few nanometers.

8.1. Polystyrene Nanoparticles Formed in Microphase Inversion

The particle size can be controlled by the initial ionomer concentration, the content of ionic groups, and the counterions. Figure 66 shows that most of the ionomer chains existed as individual carboxylated polystyrene (CPS) ionomer chains in THF with a hydrodynamic radius in the range $\sim$1–10 nm. The second peak located at $\sim$70 nm indicates a very small number of interchain aggregates, even at $C = 1 \times 10^{-4}$ g/mL, where ionic association still exists. Figure 66 also shows that the higher carboxylation extent leads to larger aggregates, reflecting that the nature of the interchain association in THF is through ionic interactions.

Figure 67 shows that the size of the nanoparticles formed by adding the NaCPS and MnCPS THF solution dropwise in an excess of water is in the range $\sim$10–100 nm, depending on the extent of the carboxylation and the kind of metal ion used. It is worth noting that nanoparticles formed in this manner were so stable that there was no change in particle size distribution even after 4 months at room temperature. We also found that the NaCPS ionomer chains formed nanoparticles ($\sim$20 nm) that are stable in water even if the initial ionomer concentration was as high as 2×10^{-2} g/mL, but in the case of MnCPS, the high initial ionomer concentration resulted in precipitation. Stable MnCPS nanoparticles can be obtained only if the initial MnCSP concentration is lower than 2×10^{-3} g/mL. Figure 67 clearly shows that using Mn^{2+} instead of Na^+ as a counterion leads to much larger particles. M_w and $\langle R_h \rangle$ of 4.8 and 6.8 MnCPS nanoparticles are 1.2×10^8 g/mol and 54 nm, and 5.5×10^7 g/mol and 48 nm, respectively. In comparison with the initial molar mass ($M_w = 3.4 \times 10^4$ g/mol)
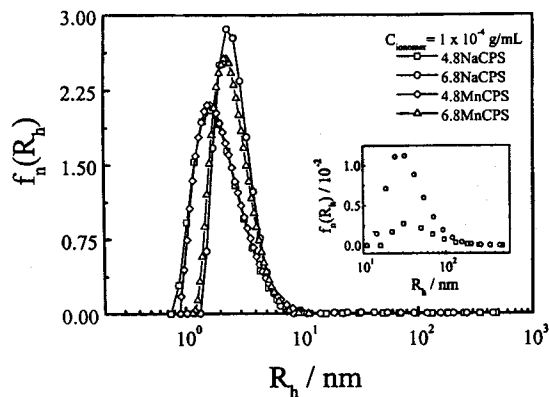
Figure 66. Typical number distributions $f_n(R_h)$ of the hydrodynamic radius of the NaCPS and MnCPS chains in THF, where the ionomer concentration is 1×10^{-4} g/mL. The inset shows a 100 times enlargement of the second peak in $f_n(R_h)$, indicating that a very small number of large interchain aggregates exist. Reprinted with permission from [151], M. Li et al., *Macromolecules* 31, 6841 (1998). © 1998, American Chemical Society.

of individual MnCPS ionomer chains, we know that the 4.8 and 6.8 MnCPS nanoparticles, respectively, consist of ~3500 and ~1600 chains. Assuming that the nanoparticles are uniform spheres and all the ionic group are on the surface, we estimated that the average surface area (s_{ionic}) per ionic group on the particle surface is $0.9 \sim 1.0$ nm^2 from $\langle R_h \rangle$ and M_w, which is lower than ~3 nm^2 found for the NaCPS nanoparticles [146], and the density of the particles is $0.2 \sim 0.3$ g/cm^3, which is much lower than the density (~1.0 g/cm^3). The lower chain density indicates that the MnCPS nanoparticles have a loose structure, which is also reflected in the ratio of $\langle R_g \rangle / \langle R_h \rangle$, which is ~1.0 instead of the ~0.774 predicted for a uniform compact sphere. The loose structure also explains why the MnCPS particles are much larger and why the estimated s_{ionic} is small, because for a given $\langle R_h \rangle$, the loose
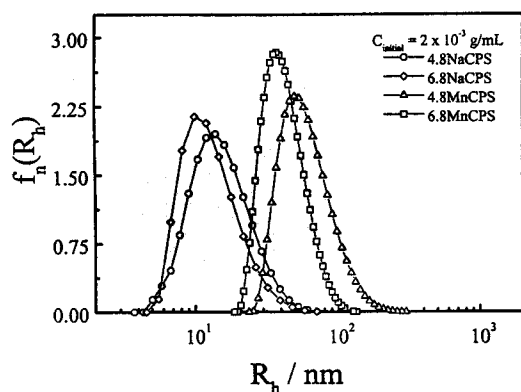
structure has a much larger surface area than that estimated from $\langle R_h \rangle$ on a uniform compact sphere.

Furthermore, our results show that removal of the 1% THF from the dispersion leads to smaller particles, that is, the particles contract, which supports the assumption that NaCPS nanoparticles have a loose structure. On the other hand, the addition of THF to the dispersion leads to swelling of the 4.8 MnCPS nanoparticles, which indicates that there is a preferential adsorption of THF onto the nanoparticles to which the loose structures can be attributed. Our results also show that higher initial ionomer concentrations result in larger particles with a broad size distribution. On the other hand, for a given initial ionomer concentration, higher carboxylation extents led to smaller particles. This can be attributed to the fact that each ionic group can cover only a certain area of the particle surface. When the carboxylation extent is high, each particle requires less ionomer chains to reach the same charge density on the particle surface, so the particle size is smaller. The same argument can also be used to explain why using Mn^{2+} instead of Na$^+$ as counterions leads to larger particles, because Na$^+$ can induce a stronger ionic repulsion so that each Na$^+$ stabilizes more surface area.

Figure 68 shows that the addition of water to the ionomer solution results in larger nanoparticles with a narrower distribution than the reverse process. It can be imagined that in the case of adding the ionomer THF solution dropwise into water, the local environment of the ionomer chains changes rapidly from THF to almost pure water, so that individual ionomer chains quickly collapse and disperse in water under ultrasonification, and the ionomer chains have less chance to form large particles through interchain aggregation. In the process of adding water dropwise into the ionomer THF solution, the polystyrene chains around the water droplet collapse into the water droplet and aggregate with each other to form large particles because local ionomer concentration is relatively higher. The question is how such nanoparticles can be stabilized and what determines the particle size. During the aggregation, the
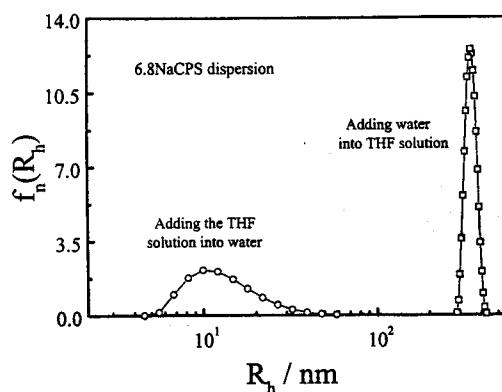

Figure 67. Typical number distributions $f_n(R_h)$ of the hydrodynamic radius of the CPS nanoparticles that are stable in water, where the CPS nanoparticles were formed by adding the CPS ionomer THF solution dropwise into an excess of water. Reprinted with permission from [151], M. Li et al., *Macromolecules* 31, 6841 (1998). © 1998, American Chemical Society.

Figure 68. Comparison of the number distributions $f_n(R_h)$ of the hydrodynamic radius of the CPS nanoparticles formed in the two different methods of mixing the CPS ionomer THF solution and water. Reprinted with permission from [151], M. Li et al., *Macromolecules* 31, 6841 (1998). © 1998, American Chemical Society.

surface area (S) of the particle is proportional to the square of its radius (R), the number (N_{ionic}) of the ionic groups on the surface is proportional to the associated chain number (N_{chain}) per aggregate, and N_{chain} is further proportional to the mass of the particle ($M_{particle}$). For a uniform particle, $M \propto R^3$. Therefore, the average surface area occupied per ionic group $s = S/N_{ionic} \propto R^{-1}$. As the aggregation proceeds, R increases and s decreases. For a given ionomer in water, there should exist a minimum value of s at which the particle surface is fully "covered" by the ionic groups and further coagulation becomes impossible because of electrostatic repulsion.

8.2. CPS Chains with Different Lengths and Amounts of Hydrophilic Groups

To have a better understanding of the formation and stabilization of CPS particles, we prepared surfactant-free polymeric particles by using a series of narrowly distributed CPS chains with different lengths and amounts of hydrophilic groups, and systematically studied their formation and stabilization under different conditions. These nanoparticles that are stable in water can be formed via a microphase inversion if a delicate balance between hydrophobic and hydrophilic interactions is carefully established. The structure of such formed particles is governed by hydrophilic interactions determined by the hydrophilic groups located on the periphery and the hydrophobic interaction coming from the hydrophobic backbones inside the particles. More hydrophilic groups can stabilize a larger total interface area so that the particle size generally decreases as the number of hydrophilic groups increases.

Figure 69 shows that the nanoparticles made of the CPS chains were very stable even after ~7 months. Removing the 1% THF from the dispersion did not change $f(R_h)$, indicating that the THF has no effect on stabilization of the particles. In contrast, polystyrene homopolymer chains are not able to form surfactant-free particles that are stable in water. Therefore, a small amount of hydrophilic moiety (—COOH) is essential
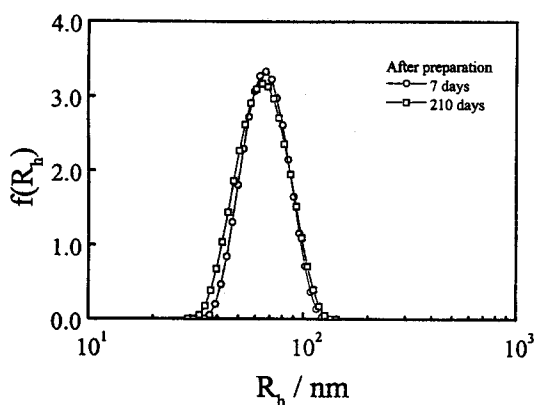
Figure 69. Standing time dependence of the hydrodynamic radius distributions $f(R_h)$ of CPS particles, where [—COOH] = 14.5 mol% and $M_{w, chain}$ = 6.43×10^3 g/mol. Reprinted with permission from [171], G. Zhang et al., *Langmuir* 16, 9205 (2000). © 2000, American Chemical Society.

for the stabilization. Considering that the dissociation constant of benzoic acid is only 6.46×10^{-5} at 25 °C, the ionization of —COOH is so limited that the stabilization should not be solely attributed to electrostatic repulsion, which was confirmed by the fact that once the particle formed, its size was independent of the ionic strength. The hydrophilic interactions that drive the stabilization should include the hydrogen bonding between —COOH and water, the electrostatic repulsion between —COO⁻ groups, and the interaction between —COO⁻ and water. Our preliminary experiments showed that precipitation instead of a stable dispersion occurred if the CPS THF solution was not added dropwise, but poured into the water. In the particle formation, after each drop of the CPS THF solution is added to the water, the insoluble hydrophobic backbones tend to collapse and associate with each other to minimize their interface with water, whereas the hydrophilic carboxylic groups try to stay on the periphery to reduce the interfacial energy even though not all of them are able to locate on the interface [149]. The dropwise addition and initial dilute solution provided more chances for the carboxylic groups to locate on the particle surface instead of being buried inside, so the hydrophilic stabilization was enhanced. Note that the CPS chains are practically "frozen" inside the particle due to the strong hydrophobic interaction, and the interparticle fusion is difficult, if not impossible. In this sense, the hydrophobic interaction is not only responsible for particle formation, but also for particle stabilization. Accordingly, formation of the particles is dependent not only on a delicate balance between hydrophilic and hydrophobic interactions, but also on the formation process.

Figure 70 shows that both the particle size and the average number of CPS chains inside each particle (N_{chain}) decrease as [—COOH] increases in the range 7.4–26.1 mol%. A similar trend was also observed for different polymeric colloids [146, 150–152]. For a given polymer/water interface, the average surface area stabilized by each hydrophilic moiety should be a constant [148, 150, 152]. Consequently, more hydrophilic moieties can stabilize a larger total surface area, corresponding to smaller particles. However, in the range 26.1–49.2 mol%, the particle size ($\langle R_h \rangle$) increases from 32 to 44 nm, while the average number (N_{chain}) of the CPS chains inside each particle almost remains. Figure 71 reveals that in this higher [—COOH] range, $f(R_h)$ splits into two peaks respectively located in the ranges ~10–20 and ~25–80 nm, much different from those narrowly distributed $f(R_h)$ shown in Figure 69. A dilution of the dispersion from 1.0×10^{-5} to 1.0×10^{-6} g/mL shifts the peak position and weighting; namely, the peak that corresponds to larger particles becomes smaller, while the peak that corresponds to smaller particles becomes larger and shifts to ~10 nm, indicating the dissociation of the particles. When the carboxylation extent is high, the hydrophobic polystyrene segment between two neighboring carboxylic groups, on average, becomes short and the association of these segments inevitably traps more carboxylic groups inside, resulting in a less compact structure. The CPS chains inside these particles are more mobile, so the dilution breaks up
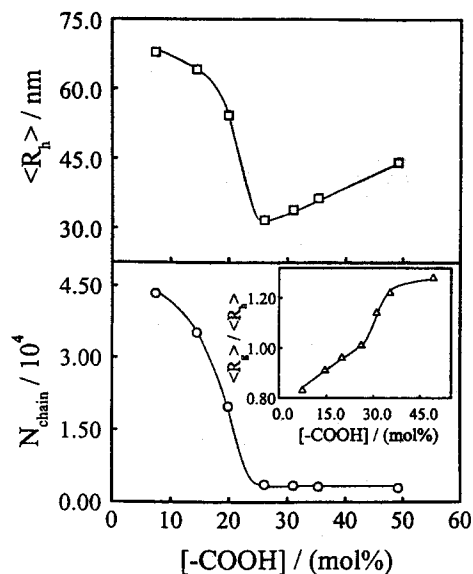
Figure 70. Carboxylation extent dependence of the average hydrodynamic radius ($\langle R_h \rangle$), the average number of CPS chains (N_{chain}) inside each particle, and the ratio of the average radius of gyration to the average hydrodynamic radius ($\langle R_g \rangle / \langle R_h \rangle$) of CPS nanoparticles, where $N_{chain} = M_{w,\,particle} / M_{w,\,chain}$ and $M_{w,\,chain} = 6.43 \times 10^3$ g/mol. Reprinted with permission from [171], G. Zhang et al., *Langmuir* 16, 9205 (2000). © 2000, American Chemical Society.

the particles. On the other hand, it is known that the ratio of the average radius of gyration to the average hydrodynamic radius $\langle R_g \rangle / \langle R_h \rangle$ increases as the structure or conformation extends. For example, for a uniform nondraining sphere, a hyperbranched cluster, and a coil chain, the ratios of $\langle R_g \rangle / \langle R_h \rangle$ are 0.774, ~1.0–1.3, and ~1.5–1.8, respectively [154–156]. The increase of $\langle R_g \rangle / \langle R_h \rangle$ from 0.8 to ~1.3 as [—COOH] increases from 7.4 to 49.2 mol%, shown in the inset of Figure 70, indicates a gradual transition of the particle structure from a compact spherelike form into a swollen hyperbranched clusterlike form.
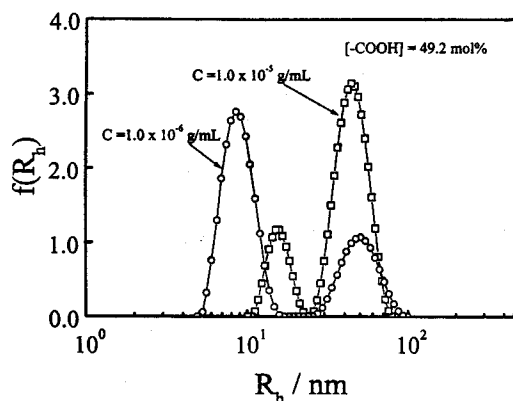
Figure 72 shows that the counterion and the chain length also affect the stability and size of the particles. LiCPS with more hydrophilic groups (—COOLi) formed much smaller particles compared with the corresponding CPS. This is because groups with higher hydrophilicity have more chance to stay at the particle/water interface than inside particles. Our LLS results directly confirm that the increase in both the hydrophilicity and the density of hydrophilic groups on a particle surface reduces the particle size and promotes its stability, as found in surfactant-free emulsion copolymerization [149, 157–159]. Figure 72 also shows that the particle size decreases as the CPS chain length increases even though each chain, statistically, has the same carboxylation extent. As we discussed before [152], a competition exists between intrachain contraction and interchain association in particle formation. Domination of the intrachain contraction leads to smaller particles. For a given weight concentration, a longer chain can be viewed as several connected short chains. Therefore, the intrachain contraction should be easier for a longer chain due to geometric constraints.

The effects of the nature and the amount of hydrophilic groups as well as the chain length on particle size and stability experimentally support the theory of Israelachvili and Wennerstrong [160]; namely, the entropic repulsion that arises from the particle surface properties drives the particle stabilization. We also found that when [—COOH] > 26 mol%, adding styrene monomer to the dispersion leads to swelling of the clusters, indicating that styrene is preferentially absorbed inside the clusters. The swollen clusters are stable

Figure 71. Effect of dilution on the hydrodynamic radius distribution $f(R_h)$ of CPS particles formed with a high carboxylation extent, where $M_{w,\,chain} = 6.43 \times 10^3$ g/mol. Reprinted with permission from [171], G. Zhang et al., *Langmuir* 16, 9205 (2000). © 2000, American Chemical Society.
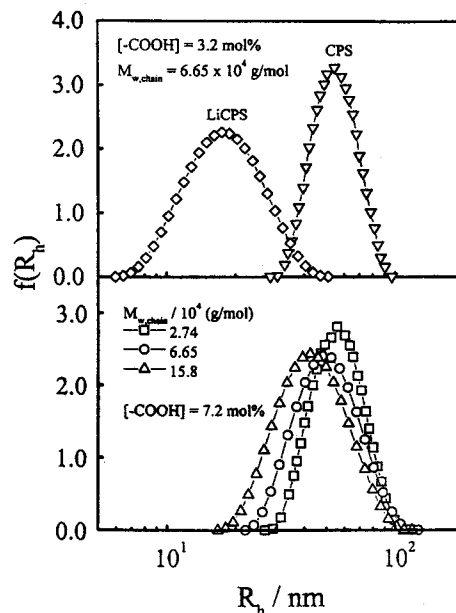

Figure 72. Counterion and chain length dependence of the hydrodynamic radius distribution $f(R_h)$ of CPS particles. Reprinted with permission from [171], G. Zhang et al., *Langmuir* 16, 9205 (2000). © 2000, American Chemical Society.

in water, suggesting that in surfactant-free emulsion copolymerization of hydrophilic and hydrophobic monomers, the initially formed hydrophobically associated copolymer chains may serve as seeds in polymerization.

8.3. Self-Assembly of CSEBS Triblock Copolymer Chains

Self-assembly of carboxylated poly(styrene-b-ethylene-co-butylene-b-styrene) (CSEBS) chains in water via microphase inversion was governed by a delicate balance between intrachain contraction and interchain association. The hydrophobic attraction leads, on one hand, to the formation of polymeric particles, but on the other hand, prevents interparticle fusion. The hydrophilic repulsion results, on one hand, in the stabilization of the particles, but on the other hand, yields swelling of the particles from spherelike to hyperbranch-like form. The right balance of the two different interactions enables us to prepare small surfactant-free polymeric nanoparticles that are stable in water.

Figure 73 shows that the hydrophobic association of the CSEBS chains in water leads to surfactant-free polymeric nanoparticles. The relative distribution width is in the range 0.04–0.1. As expected, the particle size decreases as [—COOH] increases, because more carboxylic groups can stabilize more surface area, in that, for a given mass of polymer, smaller particles can provide more total surface area. Such formed CSEBS nanoparticles were very stable even after the dispersion was concentrated 100 times from 1.0×10^{-5} to 1.0×10^{-3} g/mL by solvent evaporation as shown in Figure 74. The driving force behind the stabilization of polymeric colloidal particles in water has long been debated. Langmuir [161] suggested that the hydration or structural force of water molecules bound on particle surfaces was responsible for the stabilization. More recently, it was found that the hydration forces are not monotonically repulsive, but attractive or oscillatory, so the stabilization of polymeric colloidal particles
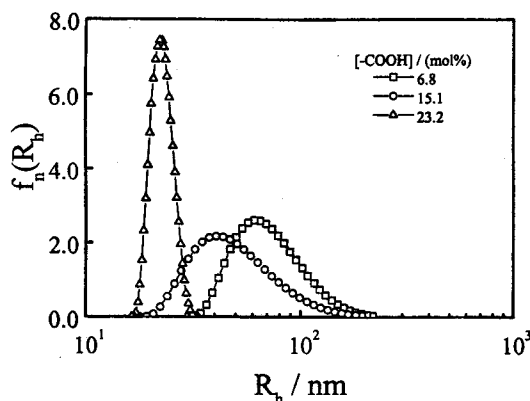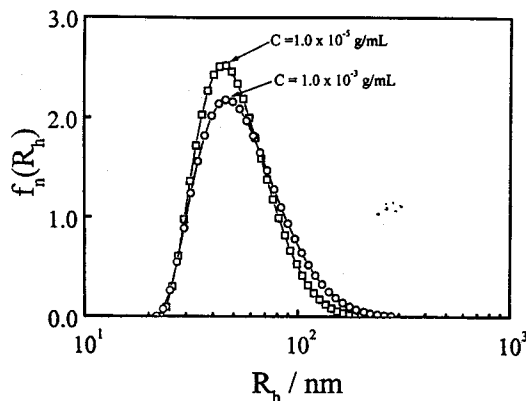
Figure 74. Concentration dependence of the number distribution $f_n(R_h)$ of the hydrodynamic radius of CSEBS nanoparticles, where [—COOH] = 13.3 mol% and $C = 1.0 \times 10^{-5}$ g/mL. Reprinted with permission from [172], G. Zhang et al., *Macromolecules* 33, 6340 (2000). © 2000, American Chemical Society.

should be related to the entropic repulsion, depending on the surface characteristic [160].

In the microphase inversion, the mixing of THF with water was nearly instantaneous after each drop of THF solution was added. The intrachain contraction and interchain association of the hydrophobic middle poly(ethylene-co-butylene) blocks lead to particle formation, whereas the relatively more hydrophilic CPS blocks have a tendency to stay on the periphery. The number of carboxylic groups (n) on each nanoparticle surface increases as the association proceeds, and n is proportional to the average number of polymer chains inside each nanoparticle (N_{chain}). On the other hand, the average particle volume (V) is also proportional to N_{chain} if the particle density is assumed to be a constant, so that $n \propto V \propto R^3$, where R is the particle size. Note that the particle surface area (S) is only proportional to R^2. Therefore, $S/n \sim R^{-1}$; namely, the surface area stabilized per carboxylic group decreases as R increases until S/n reaches a minimum at which the interchain association stops. Further fusion of two such formed particles would be difficult, if not impossible, because the polymer chains are practically frozen inside due to strong hydrophobic interaction. The time required for an interparticle diffusion of the polymer chains is much longer than the collision time of two particles under Brownian motion in the dispersion. This is why the metastable nanoparticles are very stable in water.

Figure 75 shows that in the range 3.3–23.2 mol%, both the particle size and the average number of polymer chains inside each nanoparticle (N_{chain}) decrease as [—COOH] increases. Polymeric nanoparticles made of carboxylated and sulfonated polystyrene ionomers [150, 151], poly(N-isopropylacrylamide-co-acrylic acid) [152] and poly(N-isopropylacrylamide) grafted with poly(ethylene oxide) [153] exhibit a similar tendency. As expected, less chains with a higher [—COOH] can offer an equivalent number of stabilizing groups as more chains with a lower [—COOH]. The particle size is determined by a delicate balance between the

Figure 73. Carboxylation extent dependence of the number distribution $f_n(R_h)$ of the hydrodynamic radius of CSEBS nanoparticles, where $C = 1.0 \times 10^{-5}$ g/mL. Reprinted with permission from [172], G. Zhang et al., *Macromolecules* 33, 6340 (2000). © 2000, American Chemical Society.
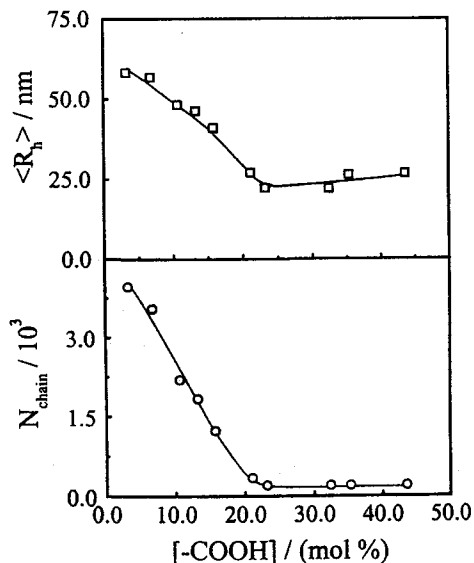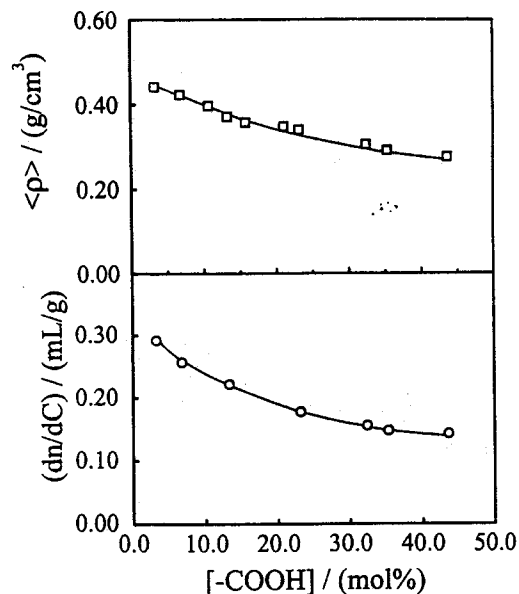
Figure 75. Carboxylation extent dependence of the average hydrodynamic radius ($\langle R_h \rangle$) of CSEBS nanoparticles and the average number (N_{chain}) of polymer chains inside, where $C = 1.0 \times 10^{-5}$ g/mL and N_{chain} is defined as $M_{w,particle}/M_{w,chain}$. Reprinted with permission from [172], G. Zhang et al., *Macromolecules* 33, 6340 (2000). © 2000, American Chemical Society.

hydrophobic attraction and hydrophilic stabilization. Further increase of [—COOH] in the range 23.2–43.6 mol% leads to a slight increase of $\langle R_h \rangle$ from 22 to 28 nm, but N_{chain} remains almost constant, indicating the swelling of the particles.

Figure 76 shows that the average density $\langle \rho \rangle$ of the CSEBS particles decreases as [—COOH] increases. Note that some of the carboxylic groups were inevitably trapped inside [149]. A study of the aggregation of poly(ethylene-*co*-methacrylic acid) in water suggested that each aggregate consists of a hydrophobic core, an intermediate layer made of the ionomer chains and counterions, and a hydrophilic periphery where most of the ionic groups are located [162]. The decrease of $\langle \rho \rangle$ as [—COOH] increases can be attributed to repulsion between the carboxylic groups inside. The decrease of dn/dC as [—COOH] increases shown in Figure 76 reflects the association of more water molecules (a lower refractive index) with the CSEBS chains inside the particles. The structure change of the nanoparticles can be better viewed in terms of the ratio of the average radius of gyration to the average hydrodynamic radius $\langle R_g \rangle/\langle R_h \rangle$.

Figure 77 shows that $\langle R_g \rangle/\langle R_h \rangle$ increases from ~0.86 to 1.16 as [—COOH] increases from 3.3 to 43.6 mol%. For a uniform nondraining sphere, a hyperbranched cluster, and a random coil, the ratios of $\langle R_g \rangle/\langle R_h \rangle$ are 0.774, ~1.0–1.3, and ~1.5–1.8, respectively. The fact that $\langle R_g \rangle/\langle R_h \rangle \sim 0.86$ at [—COOH] ~3.3% indicates that particles are practically draining and spherelike. The increase of $\langle R_g \rangle/\langle R_h \rangle$ reveals that the nanoparticle structure gradually changes from spherelike to clusterlike. The change in particle structure was also evidenced by the effect on $f(R_h)$ of diluting the dispersion. When [—COOH] < 23.2 mol%, the dilution had no influence

Figure 76. Carboxylation extent dependence of the apparent chain density ($\langle \rho \rangle$) and the specific refractive index increment (dn/dC) of CSEBS nanoparticles, where $dn/dC = \lim_{C\to 0}[(n_{solution} - n_{solvent})/C]$ and $\langle \rho \rangle = M_w/[(4/3)N_A\langle R_h \rangle^3]$ where n, M_w, and $\langle R_h \rangle$ are the refractive index, the weight average molar mass, and the average hydrodynamic radius, respectively. Reprinted with permission from [172], G. Zhang et al., *Macromolecules* 33, 6340 (2000). © 2000, American Chemical Society.

on $f(R_h)$, because a relatively strong hydrophobic attraction holds the polymer chains together. However, when [—COOH] is higher and the polymer chains are more hydrophilic, the dilution from 1.0×10^{-5} to 1.0×10^{-6} g/mL can split a narrowly distributed $f(R_h)$ into a bimodal distribution as shown in Figure 78. The peak located at ~6 nm can be attributed to individual collapsed CSEBS chains, because individual SEBS chains in THF (a good solvent) have a value of $\langle R_h \rangle \sim 13$ nm [163]. Therefore, in a very dilute dispersion, the interchain
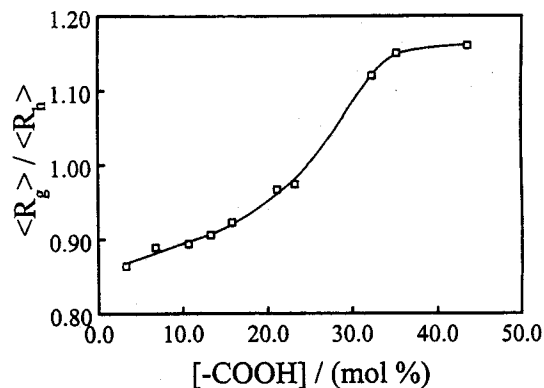
Figure 77. Carboxylation extent dependence of the ratio of the average radius of gyration to the average hydrodynamic radius ($\langle R_g \rangle/\langle R_h \rangle$) of CSEBS nanoparticles, where $C = 1.0 \times 10^{-5}$ g/mL. Reprinted with permission from [172], G. Zhang et al., *Macromolecules* 33, 6340 (2000). © 2000, American Chemical Society.
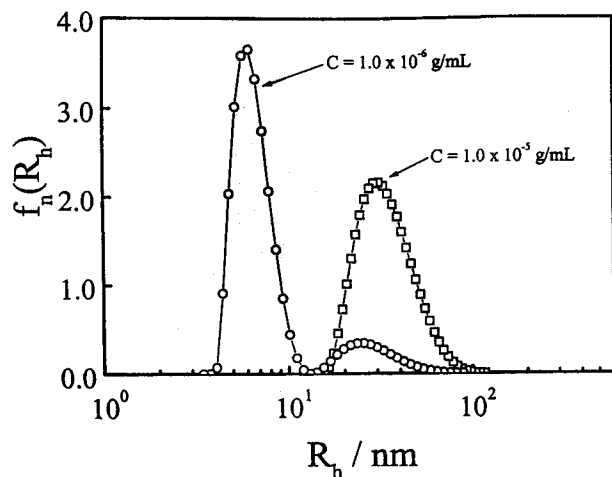
Figure 78. Effect of dilution on the number distribution $f_n(R_h)$ of the hydrodynamic radius of CSEBS nanoparticles, where [—COOH] = 35.2 mol%. Reprinted with permission from [172], G. Zhang et al., *Macromolecules* 33, 6340 (2000). © 2000, American Chemical Society.

association is greatly suppressed so that individual unimolecular micelles formed via the intrachain contraction are in equilibrium with large interchain aggregates.

ACKNOWLEDGMENTS

REFERENCES

1. S. Forster and M. Schmidt, *Adv. Polym. Sci.* 120, 51 (1995).
2. N. Ise, *Angew. Chem., Int. Ed. Engl.* 25, 323 (1986).
3. D. F. Hodgson and E. J Amis, in "Polyelectrolytes" (M. Hara, Ed.). Dekker, New York, 1993.
4. M. Sedlak, *Macromolecules* 26, 1158 (1993).
5. T. Odijk, *J. Poly. Sci. Polym. Phys. Ed.* 25, 323 (1977).
6. J. Skolnick and M. Fixman, *Macromolecules* 10, 9444 (1977).
7. J. L. Barrat and J. F. Joanny, *Europhys. Lett.* 24, 333 (1993).
8. S. C. Lin, W. I. Li, and M. J. Schurr, *Biopolymers* 17, 1041 (1978).
9. K. Kaji, H. Urakawa, H. Kanaya, and R. Kitamaru, *J. Phys.* 49, 93 (1988).
10. M. Sedlak and E. J. Amis, *J. Chem. Phys.* 96, 817 (1992).
11. X. Qiu and C. Wu, *Macromolecules* 30, 6090 (1997).
12. P. G. de Gennes, P. Pincus, R. M. Velasco, and F. Brochard, *J. Phys. (Paris)* 37, 1461 (1976).
13. A. R. Khokhlov and K. Khachaturian, *Polymer* 23, 1742 (1982).
14. V. Borue and X. Eurokomovich, *Macromolecules* 21, 3240 (1998).
15. J. F. Joanny and L. Leibler, *J. Phys.* 51, 545 (1990).
16. T. A. Vilgis and R. Borsali, *Phys. Rev. A* 43, 6857 (1991).
17. W. Essafi, F. Lafuma, and C. Williams, in "Macro-ion Characterization: From Dilute Solutions to Complex Fluid" (K. S. Schmitz, Ed.). ACS Symposium Series, Vol. 548, p. 278. American Chemical Society, Washington, DC, 1994.
18. M. Shibayama, T. Tanaka, and C. C. Han, *J. Chem. Phys.* 97, 6842 (1992).
19. A. Moussaid, F. Schosselser, J. P. Munch, and S. J. Candau, in "Macro-ion Characterization: From Dilute Solutions to Complex Fluid" (K. S. Schmitz, Ed.). ACS Symposium Series, Vol. 548, p. 287. American Chemical Society, Washington, DC, 1994.
20. A. S. Michaels and R. G. Miekka, *J. Phys. Chem.* 65, 1765 (1961).
21. J. Smid and D. Fish, *Encycl. Polym. Sci. Eng.* 11, 720 (1988).
22. B. Philipp, H. Dautzenberg, K.-J., Linow, J. Koetz, and W. Dawydoff, *Prog. Polym. Sci.* 14, 91 (1989).
23. E. Tsuchida, Y. Osada, and H. Ohno, *J. Macromol. Sci. B* 17, 683 (1980).
24. V. A. Kabanov and A. B. Zezin, *Pure Appl. Chem.* 56, 343 (1985).
25. R. D. Porasso, J. C. Benegas, and M. G. T. Van den Hoop, *J. Phys. Chem. B* 103, 2361 (1999).
26. C. Heitz and J. Francois, *Polymer* 40, 3331 (1999).
27. P. Dziezok, S. S. Sheiko, K. Fischer, M. Schmidt, and M. Moller, *Angew. Chem., Int. Ed. Engl.* 36, 2812 (1998).
28. M. G. Burnett, C. Faharty, C. Hardacre, J. M. Mallon, G. C. Saunders, and O. R. Mark, *Chem. Commun.* 22, 2525 (1998).
29. M. Hara and A. Nakajima, *J. Polym. Sci., Part B: Polym. Phys.* 27, 1043 (1989).
30. W. A. Bowman, M. Rubinstein, and J. S. Tan, *Macromolecules* 30, 3262 (1997).
31. B. L. Rivas and V. I. Moreno, *Chem. Lett.* 2, 166 (2000).
32. D. Takahashi, Y. Kubota, K. Kokai, T. Izumi, M. Hirata, and E. Kokufuta, *Langmuir* 16, 3133 (2000).
33. P. L. Dubin, S. S. The, L. M. Can, and C. H. Chew, *Macromolecules* 23, 500 (1990).
34. W. Liu, A. L. Cholli, R. Nagarajan, J. Kumar, S. Tripathy, F. F. Bruno, and L. Samuelson, *J. Am. Chem. Soc.* 121, 11,345 (1999).
35. F. Petit, R. Andebert, and I. Iliopoulos, *Colloid Polym. Sci.* 273, 777 (1995).
36. P. Aymard, T. Nicolai, D. Durand, and A. Clark, *Macromolecules* 32, 2542 (1999).
37. A.Y. Kim and J. C. Berg, *Langmuir* 16, 2101 (2000).
38. S. Takata, T. Norisuye, N. Tanaka, and M. Shibayama, *Macromolecules* 33, 5470 (2000).
39. O. Pelletier, P. Davidson, C. Bourgaux, C. Coulon, S. Regnault, and J. Livage, *Langmuir* 16, 5295 (2000).
40. N. Mitsuo, N. Tomohide, N. Yoshiki, and W. Syogo, *J. Chem. Phys.* 110, 2711 (1999).
41. H. Dautzenberg, G. Rother, and J. Hartmann, "Macro-ion Characterization: From Dilute Solutions to Complex Fluids" (K. Schmitz, Ed.). ACS Symposium Series, Vol. 548. American Chemical Society, Washington, DC, 1994.
42. N. V. Pogodina and N. V. Tsvetkov, *Macromolecules* 30, 4897 (1997).
43. S. Dai, K. C. Tam, and R. D. Jenkins, *Macromolecules* 33, 404 (2000).
44. A. Kjoniksen, B. Joabsson, K. Thuresson, and B. Nystroem, *J. Phys. Chem. B* 103, 9818 (1999).
45. K. N. Bakeev, V. A. Isumrudov, S. I. Kuchanov, A. B. Zezin, and V. A. Kabanov, *Macromolecules* 25, 4249 (1992).
46. M. Tsianou, A. Kjoniksen, K. Thuresson, and B. Nystrom, *Macromolecules* 32, 2974 (1999).
47. B. Vishalakshi, S. Ghosh, and V. Kalpagam, *Polymer* 34, 3270 (1993).
48. M. V. Smoluchowski, *J. Phys. Chem.* 92, 129 (1918).
49. D. Sornette, A. Johansen, A. Arneodo, J. F. Muzy, and H. Saleur, *Phys. Rev. Lett.* 76, 251 (1996).
50. M. Tirado, A. Schmitt, J. Callejas, and A. Fernandez, *Prog. Colloid Polym. Sci.* 104, 138 (1997).
51. M. Heskins and J. E. Guillet, *J. Macromol. Sci. Chem.* 2, 1441 (1969).
52. H. G. Schild, *Prog. Polym. Sci.* 7, 163 (1992) and references therein.
53. S. Hirotsu, Y. Hirokawa, and T. Tanaka, *J. Chem. Phys.* 87, 1392 (1987).
54. L. C. Dong, Q. Yan, and A. S. Hoffman, *J. Controlled Release* 19, 171 (1992).
55. C. Wu and S. Zhou, *Macromolecules* 28, 8381 (1995).
56. H. Hayashi, K. Kono, and T. Takagishi, *Biochim. Biophys. Acta* 1280, 127 (1996).
57. M. Antonietti, W. Bremser, and M. Schmidt, *Macromolecules* 23, 3796 (1990).

58. C. Wu, K. K. Chan, K. F. Woo, R. Qian, X. Li, L. Chen, D. H. Napper, G. Tan, and A. J. Hill, *Macromolecules* 28, 1592 (1995).

59. J. Ricka, M. Meewes, R. Nyffenegger, and Th. Binkert, *Phys. Rev. Lett.* 65, 657 (1990).

60. I. I. Pashkin, Yu. E. Kirsh, V. P. Zubov, T. V. Anisimova, I. F. Kuzkina, and Ya. V. Voloshina, *Polym. Sci., Ser. A* 35, 581 (1993).

61. S. F. Shestyuk, I. Yu. Galaev, A. P. Savitskii, Yu. E. Kirsh, and I. V. Berezin. *Biotechnologiya* 3(2), 178 (1987).

62. M. Eisele and W. Burchard, *Makromol. Chem.* 191, 169 (1990).

63. Yu. E. Kirsh, I. Yu. Galaev, T. M. Karaputadze, A. A. Margolin, and V. K. Shvyadas, *Biotechnologiya* 3(2), 184 (1987).

64. O. F. Solomon, M. Corciovei, and C. Boghina, *J. Appl. Polym. Sci.* 12, 1843 (1968).

65. E. E. Makhaeva, L. T. M. Thanh, S. G. Starodoudoubtsev, and A. R. Khokhlov, *Macromol. Chem. Phys.* 197, 1973 (1996).

66. L. M. Mikheeva, N. V. Grinberg, A. Ya. Mashkevich, and V. Ya. Grinberg, *Macromolecules* 30, 2693 (1997).

67. W. H. Stockmayer and M. Schmidt, *Pure Appl. Chem.* 54, 407 (1982).

68. Y. Hirokawa and T. Tanaka, *J. Chem. Phys.* 81, 6379 (1984).

69. B. G. Ershov and A. Henglein, *J. Phys. Chem. B* 102, 10,663 (1998).

70. Y. Ikeda, M. Beer, M. Schmidt, and K. Huber, *Macromolecules* 31, 728 (1998).

71. C. Heitz and J. Francois, *Polymer* 40, 3331 (1999).

72. F. T. Wall and J. W. Drenan, *J. Polym. Sci.* 7, 83 (1951).

73. P. J. Flory and J. E. Osterheld, *J. Phys. Chem.* 58, 653 (1954).

74. P. I. Fracex and S. M. Haas, *J. Nutr.* 107, 1889 (1977).

75. I. R. Prohaska and O. A. Zukasewycz, *Science* 213, 559 (1983).

76. H. Rotnenbacher and H. Schermann, *J. Nutr.* 110, 1648 (1980).

77. D. A. Hart, *Cell Immunol.* 71, 169 (1982).

78. H. S. Frank and W. Y. Wen, *Discuss. Faraday Trans.* 74, 583 (1978).

79. D. W. James and R. L. Frost, *J. Chem. Soc., Faraday Trans.* 74, 583 (1978).

80. J. C. Hindman, *J. Chem. Phys.* 36, 1000 (1962).

81. M. Shibayama, F. Ikkai, S. Inamoto, S. Nomura, and C. C. Han, *J. Chem. Phys.* 105, 4358 (1996).

82. Y. Li and T. Tanaka, *J. Chem. Phys.* 90, 5161 (1989).

83. M. Annaka and T. Tanaka, *Nature* 355, 430 (1992).

84. K. B. Zeldovich, E. E. Dormidontova, and A. R. Khokhlov, *J. Phys. II* 7, 627 (1997).

85. R. G. Pearson, *J. Chem. Educ.* 45, 581, 643 (1968).

86. G. Klopman, "Chemical Reactivity and Reaction Path." Wiley, New York, 1974.

87. R. Mizuguchi, S. Ishikura, A. Takahashi, and A. Uenaka, U.S. Patent 4,215,028, 1980.

88. R. Knoesel, M. Ehrman, and J. C. Galin, *Polymer* 34, 1925 (1993).

89. D. J. Liaw, C. C. Huang, W. F. Lee, J. Borbrly, and E. T. Kang, *J. Polym. Sci., Part A: Polym. Chem.* 35, 3527 (1997).

90. D. J. Liaw, C. C. Huang, and E. T. Kang, *Colloid Polym. Sci.* 275, 922 (1997).

91. F. Ilmain, T. Tanaka, and E. Kokufuta, *Nature* 349, 400 (1991).

92. E. Kokufuta, B. Wang, R. Yoshida, A. R. Khokhlov, and M. Hirata, *Macromolecules* 31, 6878 (1998).

93. O. E. Philippova, D. Hourdet, R. Audebert, and A. R. Khokhlov, *Macromolecules* 30, 8278 (1997).

94. K. D. Branham, H. S. Snowden, and C. L. McCormick, *Macromolecules* 29, 254 (1996).

95. K. Thalberg, B. Lindman, and K. Bergfeldt, *Langmuir* 7, 2893 (1991).

96. Y. Li, J. Xia, and P. L. Dubin, *Macromolecules* 27, 7049 (1994).

97. X. Zhang, N. Hirota, T. Narita, J. Gong, and Y. Osada, *J. Phys. Chem.* 103, 6069 (1999).

98. A. R. Khokhlov, E. Y. Kramarenko, E. E. Makhaeva, and S. G. Starodubtzev, *Macromolecules* 25, 4779 (1992).

99. H. Okuzaki and Y. Osada, *Macromolecules* 28, 380 (1995).

100. Y. V. Khadurina, A. T. Dembo, V. B. Rogacheva, A. B. Zezin, and V. A. Kabanov, *Polym. Sci.* 36, 189 (1997).

101. E. Sokolov, F. Yeh, A. Khokhlov, V. Y. Grinberg, and B. Chu, *J. Phys. Chem. B* 7091 (1998).

102. Y. B. Gao, S. C. Au-Yeung, S. Q. Zhou, and C. Wu, *J. Macromol. Sci., Phys. B* 36, 417 (1997).

103. Y. B. Gao, S. C. Au-Yeung, and C. Wu, *Macromolecules* 32, 3674 (1999).

104. E. Kokufuta, H. Suzuki, and D. Sakamoto, *Langmuir* 13, 2627 (1997).

105. M. Matsukata, M. Hirata, J. P. Gong, Y. Osada, Y. Sakurai, and T. Okano, *Colloid Polym. Sci.* 276, 11 (1998).

106. P. H. Hippel and K.-Y. Wong, *Science* 145, 577 (1964).

107. R. A. Horne, J. P. Almeida, A. F. Day, and N.-T. Yu, *J. Colloid Interface Sci.* 35, 77 (1971).

108. J. L. Thomas, P. D. Brian, and D. A. Tirrell, *Biochim. Biophys. Acta* 1278, 73 (1996).

109. J. M. Park, B. B. Muhoberac, P. L. Dubin, and J. Xia, *Macromolecules* 25, 290 (1992).

110. A. Güner, A. U. Sevil, and O. J. Guven, *Appl. Polym. Sci.* 68, 891 (1998).

111. S. Peng and C. Wu, *Macromolecules* 32, 585 (1999).

112. W. A. Bowman, M. Rubinstein, and J. S. Tan, *Macromolecules* 30, 3262 (1997).

113. J. Bondeson and R. Sundler, *Biochim. Biophys. Acta* 1026, 186 (1990).

114. K. Huber, *J. Phys. Chem.* 97, 9825 (1993).

115. C. Wu and X. Wang, *Phys. Rev. Lett.* 80, 4092 (1998).

116. X. Qiu, M. Li, C. M. Kwan, and C. Wu, *J. Polym. Sci., Part B: Polym. Phys.* 36, 1501 (1998).

117. S. Magazu, G. Maisano, F. Mallamace, and N. Micali, *Phys. Rev. A* 39, 4195 (1989).

118. P. Meakin, *Phys. Rev. Lett.* 51, 1119 (1983).

119. J. E. Martin and B. J. Ackerson, *Phys. Rev. A* 31, 1180 (1985).

120. R. Jullien, R. Botet, and P. M. Mors, *Faraday Discuss. Chem. Soc.* 83, 125 (1987).

121. H. Reinecke, N. Fazel, M. Dosiere, and J. M. Guenet, *Macromolecules* 30, 8360 (1997).

122. C. Aubert and D. S. Cannell, *Phys. Rev. Lett.* 56, 738 (1986).

123. M. Y. Lin, H. M. Lindsay, D. A. Weitz, R. C. Ball, R. Klein, and P. Meakin, *Nature* 40, 4665 (1989).

124. N. Micali, F. Mallamace, A. Romeo, R. Purrello, and L. Scolaro, *J. Phys. Chem. B* 104, 5897 (2000).

125. R. Botet, M. Kolb, and R. Jullien, "Physics of Finely Divided Matter." Springer-Verlag, New York, 1985.

126. Z. Zhou and B. Chu, *J. Colloid Interface Sci.* 143, 356 (1991).

127. B. J. Mandlbrot, "Fractals, Form and Dimensions." Freeman, San Francisco, 1977.

128. D. A. Weitz, J. S. Huang, M. Y. Lin, and J. Sung, *Phys. Rev. Lett.* 54, 1416 (1985).

129. S. Peng and C. Wu, *Macromolecules* 32, 585 (1999).

130. W. D. Brown and R. C. Ball, *J. Phys. A* 18, L 517 (1985).

131. T. Vicsek, "Fractal Growth Phenomena." World Scientific, London, 1992.

132. T. C. Halsey, *Physics Today* 11, 36 (2000).

133. P. Aymard, T. Nicolai, D. Durand, and A. Clark, *Macromolecules* 32, 2542 (1999).

134. A.Y. Kim and J. C. Berg, *Langmuir* 16, 2101 (2000).

135. S. Takata, T. Norisuye, N. Tanaka, and M. Shibayama, *Macromolecules* 33, 5470 (2000).

136. N. V. Pogodina and N. V. Tsvetkov, *Macromolecules* 30, 4897 (1997).

137. S. Dai, K. C. Tam, and R. D. Jenkins, *Macromolecules* 33, 404 (2000).

138. K. N. Bakeev, V. A. Isumrudov, S. I. Kuchanov, A. B. Zezin, and V. A. Kabanov, *Macromolecules* 25, 4249 (1992).

139. M. Tsianou, A. Kjoniksen, K. Thuresson, and B. Nystrom, *Macromolecules* 32, 2974 (1999).

140. B. Vishalakshi, S. Ghosh, and V. Kalpagam, *Polymer* 34, 3270 (1993).

141. E. G. Timoshenko and A. Yu. Kuznetsov, *J. Chem. Phys.* 112, 8163 (2000) and references therein.

142. D. S. Jordan, D. W. Green, R. E. Terry, and G. P. Willhite, *J. Soc. Petrol. Eng.* 8, 463 (1982).

143. I. Yuko, B. Michael, S. Manfred, and H. Klaus, *Macromolecules* 31, 728 (1998).

144. T. A. Martin, H. J. Joost, and Van Opheusden, *Phys. Rev. E* 53, 5044 (1996).

145. M. Y. Lin, H. M. Lindsay, D. A. Weitz, R. C. Ball, R. Klein, and P. Meakin, *Phys. Rev. E.* 41, 2005 (1990).

146. M. Li, M. Jiang, L. Zhu, and C. Wu, *Macromolecules* 30, 2201 (1997).

147. Z. Gao, S. K. Varshney, S. Wong, and A. Eisenberg, *Macromolecules* 27, 7923 (1994).

148. M. Li, L. Liu, and M. Jiang, *Macromol. Rapid Commun.* 16, 831 (1995).

149. G. W. Ceska, *J. Appl. Polym. Sci.* 18, 427 (1974); 18, 2493 (1974).

150. C. Wu, M. Akashi, and M. Chen, *Macromolecules* 30, 2187 (1997).

151. M. Li, Y. Zhang, M. Jiang, L. Zhu, and C. Wu, *Macromolecules* 31, 6841 (1998).

152. X. Qiu and C. Wu, *Macromolecules* 30, 7921 (1997).

153. X. Qiu, C. M. S. Kwan, and C. Wu, *Macromolecules* 30, 6090 (1997).

154. W. Buchard, in "Light Scattering Principles and Development" (W. Brown, Ed.), p. 439. Clarendon Press, Oxford, 1996.

155. J. P. Douglas, J. Roovers, and K. F. Freed, *Macromolecules* 23, 4168 (1990).

156. L. J. M. Vagberg, K. A. Cogan, and A. P. Gast, *Macromolecules* 24, 1670 (1991).

157. M. Okubo, K. Kanaida, and T. Matsumoto, *J. Appl. Polym. Sci.* 33, 1511 (1987).

158. T. C. Pan, J. F. Kuo, and C. Y. Chen, *J. Polym. Sci., Polym. Chem. Ed.* 29, 709 (1991).

159. D. Y. Lee and J. H. Kim, *J. Appl. Polym. Sci.* 69, 543 (1998).

160. J. N. Israelachvili and H. Wennerstrom, *Nature* 379, 219 (1996).

161. I. Langmuir, *J. Chem. Phys.* 6, 873 (1938).

162. E. Szajdzinska-Peitek, M. Wolszczak, M. A. Plonka, and S. Schlick, *J. Am. Chem. Soc.* 120, 4215 (1998).

163. C. Wu, K. Woo, and M. Jiang, *Macromolecules* 29, 5361 (1996).

164. S. Peng and C. Wu, *J. Phys. Chem. B* 105, 2331 (2001).

165. S. Peng and C. Wu, *Polymer* 42(16), 6871 (2001).

166. A. Niu, D.-J. Liaw, H.-C. Sang, and C. Wu, *Macromolecules* 33, 3492 (2000).

167. S. Peng and C. Wu, *Macromolecules* 34, 568 (2001).

168. S. Peng and C. Wu, *Polymer* 42(17), 7355 (2001).

169. S. Peng and C. Wu, *Macromolecules* 32, 585 (1999).

170. S. Peng and C. Wu, *Macromolecules* 34, 6795 (2001).

171. G. Zhang, X. Li, M. Jiang, and C. Wu, *Langmuir* 16, 9205 (2000).

172. G. Zhang, L. Liu, Y. Zhao, F. Ning, M. Jiang, and C. Wu, *Macromolecules* 33, 6340 (2000).